

The Pennsylvania State University

The Graduate School

College of Engineering

FEMTOSECOND OPTICAL ENGINEERING

A Dissertation in

Electrical Engineering

by

Peng Li

© 2008 Peng Li

Submitted in Partial Fulfillment

of the Requirements

for the Degree of

Doctor of Philosophy

August 2008

The dissertation of Peng Li was reviewed and approved* by the following:

Zhiwen Liu

Assistant Professor of Electrical Engineering

Dissertation Advisor

Chair of Committee

Shizhuo Yin

Professor of Electrical Engineering

C. Russell Philbrick

Professor of Electrical Engineering

William O. Hancock

Associate Professor of Bioengineering

W. Kenneth Jenkins

Professor of Electrical Engineering

Head of the Department of Electrical Engineering

* Signatures are on file in the Graduate School

ABSTRACT

The last a few decades have witnessed the rapid progress of ultrafast optics, which has been driving the technology revolutions in scientific research and engineering applications. For instance, several recent Nobel Prize winners have made their discoveries using femtosecond optics applications in physics, chemistry and biomedicine.

This dissertation covers three important applications of ultrafast femtosecond lasers. First, we study the single particle scattering spectroscopy using supercontinuum white light tweezers. We have developed supercontinuum white light optical tweezers by using the ultrabroad band supercontinuum (SC) generated in highly nonlinear photonic crystal fibers pumped by ultrafast laser pulses and for the first time studied the scattering spectra in tightly focused supercontinuum. When the scatterer is of spherical shape, we describe modeling based on Mie's scattering theory and angular spectrum decomposition. For the non-spherical-shaped scatterers, when the size of the scatterer is small or the refractive index of the scatterer is close to the surrounding medium, another modeling based on Born approximation and Green's function is derived. The calculation results are provided as well. This work has built the foundation to understand optical scattering spectroscopy of single particles in the supercontinuum white light optical tweezers

and further application to probe the single particle's physical and chemical properties via the linear and nonlinear optical scattering spectra, which can lead to many important applications particularly in nanoparticle characterization and sensing.

The second part of this dissertation is dedicated to the study of the femtosecond pulse beam shaping. For femtosecond laser pulses, which cover bandwidths of tens of nanometers, the performance of beam-shaping a Gaussian beam into a flat-topped rectangular intensity profile is discussed for a practical realization. In the meantime, the convergence of the improved Gerchberg–Saxton algorithm has been studied and the number of iterations for phase element design is optimized. The temporal and spatial properties of femtosecond laser pulses during beam shaping are studied. This study is expected to benefit many industrial, medical and military applications where specified beam shaping profiles are desirable.

The last part of this dissertation is terahertz (THz) generation by optical rectification of femtosecond laser pulses. A method using optical rectification of supercontinuum is proposed to improve the conversion efficiency over a broadband range. Highly efficient broadband terahertz will accelerate the development of terahertz technologies and their applications to areas such as biomedical imaging and remote security screening.

Table of Contents

List of Figures	vii
Acknowledgements.....	xiii
Chapter 1 Introduction	1
Chapter 2 Supercontinuum White Light Optical Tweezers.....	6
2.1 Introduction to Optical Tweezers	6
2.2 Supercontinuum generation from photonic crystal fibers (PCF)	10
2.3 Supercontinuum White Light Optical Tweezer	14
2.4 Optical Tweezer Trapping Force Calibration- Stiffness Determination	22
2.5 Summary	37
Chapter 3 Single-particle optical scattering spectroscopy in white light supercontinuum optical tweezers.....	38
3.1 Background	38
3.2 Theoretical Model Based on Mie Theory and Angular Spectrum Decomposition	39
3.3 Experiment Verification	47
3.4 Further discussion about scattering model based Mie's Theory.....	54
3.5 Modeling Non-spherical-shaped Weak Scatterers Based On Born Approximation	64
3.6 Summary	74
Chapter 4 Femtosecond Laser Beam Shaping	75

4.1 Introduction to beam shaping	75
4.2 Lossless beam shaping phase mask design	76
4.3 Beam Shaping with Femtosecond Laser	84
4.4 Summary	93
Chapter 5 Terahertz generation	95
5.1 Background	95
5.2 Terahertz generation by optical rectification of supercontinuum	106
5.3 Summary	115
Chapter 6 Conclusions and Future Work	116
6.1 Conclusions	116
6.2 Future Work	118
Bibliography	120

List of Figures

Figure 2.1 The principle of optical trapping.....	8
Figure 2.2 (a) Typical cross section of nonlinear PCF [Source: Crystal-Fibre] and (b) supercontinuum generation	12
Figure 2.3 Typical spectrum of supercontinuum generated in highly nonlinear photonic crystal fibers (a) supercontinuum pumped by femtosecond laser pulses (b) supercontinuum pumped by subnanosecond laser pulses.	14
Figure 2.4 A 4.82- μm silica microsphere was 2D trapped by the white light tweezer.	15
Figure 2.5 A 2- μm polymer microsphere was 3D trapped by the white light tweezer, and these particles are identified, A, B, and C, in the frame sequence. First three frames show the process of a sphere being trapped by the tightly focused supercontinuum white light, frames 4-6 show the trapping in the lateral plane, and the last three frames demonstrate the trapping in the axial direction.....	16
Figure 2.6 Trapping and manipulation of microspheres and micro-rod using supercontinuum white light (a) the collapse of eight 5- μm microspheres lifted by the inverted chromatic white light tweezer after blocking the white light. (b) the falling down of a micro-rod initially lifted and aligned by the inverted chromatic white light tweezer after blocking the white light.	18
Figure 2.7 Schematic diagram of the experimental setup. The inserted pictures are (a) the background when no microsphere was trapped and (b) scattering pattern when a 2 μm latex	

microsphere was three dimensionally trapped by an inverted white light tweezer using the femtosecond supercontinuum source.....	19
Figure 2.8 Scattering efficiency curves. (a) – (c) are the scattering efficiency of three dimensionally trapped microspheres of diameter 1.5 μm , 2 μm and 2.5 μm respectively. Refractive index is 1.59 at $\lambda=589\text{ nm}$. The wavelength resolution is 10 nm.	21
Figure 2.9 Schematic diagram of SC white light optical tweezer force measurement setup. PCF, photonic crystal fiber; OBJ, objective lens; MR, mirror; BS, beam splitter; SMF, single mode fiber; PD, photodiode detector; SM, scanning mirrors.	25
Figure 2.10 Spectra of supercontinuum pumped by femtosecond laser pulses	29
Figure 2.11 Second harmonic phase delay measurement results.....	30
Figure 2.12 Schematic diagram of modified white light SC trapping force measurement setup. MR, mirror; OBJ, objective lens; BS, beam splitter; PZ, piezoelectric actuator; PD, photodiode detector.	31
Figure 2.13 Spectra of supercontinuum pumped by sub-nanosecond laser pulses.....	33
Figure 2.14 Second harmonic phase vs. $1/f$ curves	34
Figure 2.15 Trapping stiffness measurement of a 100-nm-sized gold particle trapped by SC optical tweezers. (a) SC spectrum used for gold nanoparticle trapping (b) measurement results (circles) and fitting curve (solid line)	36
Figure 3.1 Schematic diagram of optical scattering by using tightly focused supercontinuum. A linearly-polarized incoming supercontinuum is tightly focused by objective lens L_1 . The scattered light produced by a spherical scatterer is collected by objective lens L_2 and analyzed by a spectrometer.....	39

Figure 3.2 Schematic diagram of experiment setup to verify the modeling of focus beam scattering by a spherical particle.	48
Figure 3.3 Dependence of scattering efficiency on axial position (a) and (b) are the scattering efficiencies of the 1.5 and 2 μm diameter microspheres respectively at $\lambda_0 = 600\text{ nm}$ as a function of axial position. Red lines are theoretical calculation results. Blue dots are experiment results.	50
Figure 3.4 Measured chromatic aberration of the experimental system. Circles and pluses represent the results using 1.5 and 2.0- μm -diameter microspheres respectively. The blue line is the fitted curve.	51
Figure 3.5 Scattering spectra of a 1.5 μm diameter microsphere at two different positions. Dotted red lines are theoretical calculation results while solid blue lines are experiment data.	53
Figure 3.6 Normalized intensity angular distributions of focused beams scattered by spherical particles by a 800 nm source. The refractive indices of spherical scatterer and surrounding media are taken to be 1.59 and 1.33, respectively, and different color curves represent azimuthal angles at 0° , 30° , 60° and 90° , respectively. (a) 2 micron diameter sphere, $\text{NA} = 1.25$; (b) 2 micron diameter sphere, $\text{NA} = 0.85$; (c) 1 micron diameter sphere, $\text{NA} = 1.25$; (d) 1 micron diameter sphere, $\text{NA} = 0.85$	58
Figure 3.7 Normalized scattering spectrum in the forward direction. The refractive indices of spherical scatterer and surrounding media are assumed to be 1.59 and 1.33, respectively. (a) $\text{NA} = 1.25$; (b) $\text{NA} = 0.85$. Blue curves are the results of 1-micron-diameter sphere, and red curves are of 2 micron diameter sphere.	60

Figure 3.8 Normalized scattering spectrum in the backward direction. The refractive indices of spherical scatterer and surrounding media are assumed to be 1.59 and 1.33, respectively. (a) NA = 1.25; (b) NA = 0.85. Blue curves are the results of 1 micron diameter sphere, and red curves are of 2 micron diameter sphere.	61
Figure 3.9 Normalized scattering spectrum in the forward direction at different axial positions.....	62
Figure 3.10 Normalized scattering spectrum of gold nanoparticles of various sizes in the water solution. NA = 1.25. Solid, dashed and dotted lines are the results of 80 nm, 90 nm and 100 nm gold particles, respectively.	64
Figure 3.11 Normalized scattered intensity in forward direction of spherical scatterer located at different positions along z axis. Blue curves are calculated by using Mie's Theory. Red curves with circles and green curves with stars are calculated by using Born approximation method with vectorial and scalar formula, respectively. NA is 1.25, wavelength is 800nm, and refractive index of scatter is 1.59. (a) 100 nm sphere in oil; (b) 1 micron sphere in oil; (c) 100 nm sphere in water; (d) 1 micron sphere in water.....	72
Figure 3.12 Calculated forward scattering efficiency $\lambda=800\text{nm}$, N.A.=1.25, $n_{\text{sphere}}=1.59$, $n_{\text{medium}}=1.33$, $d=100\text{nm}$ (a) and $d=1000\text{nm}$ (b). Solid curve is obtained by using Mie's theory and angular spectrum decomposition while the dotted one is obtained using Born approximation method.	73
Figure 4.1 Schematic diagram of typical beam shaping system	77
Figure 4.2 Diagram of Gerchberg-Saxton Iteration.....	79
Figure 4.3(a) Normalized intensity distribution of designed flat-top beam after 5000 GS iterations. (b) Calculated MSE during the GS iterations	81

Figure 4.4 Normalized intensity distribution of designed flat-top beam after modified GS iteration (a) optimized for minimum intensity MSE (b) optimized for flatness in the center part of intensity profile.	83
Figure 4.5 Phase distribution of optimized DOE (a) unwrapped phase (b) wrapped phase from 0 to 2π	86
Figure 4.6 Normalized intensity profile of (a) unwrapped phase mask (b)	88
Figure 4.7 Pulse profiles of a 20 fs pulse passing through beam shaping system. (a) using unwrapped phase mask; (b) using wrapped phase mask.....	89
Figure 4.8 FWHM Pulse width of a 20 fs pulse passing through beam shaping system. (a) using unwrapped phase mask; (b) using wrapped phase mask	90
Figure 4.9 Total energy distribution of a 20 fs pulse passing through beam shaping system. (a) using unwrapped phase mask; (b) using wrapped phase mask	91
Figure 5.1 A schematic diagram of experimental setup of THz generation and THz-TDS detection.....	97
Figure 5.2 the typical THz time domain pulse profile and frequency domain spectrum generated by 1 mm thickness ZnTe	99
Figure 5.3 Group index in visible region(a) and refractive index in FIR(b) of ZnTe	104
Figure 5.4 Coherence lengths in ZnTe and terahertz spectrum. Coherence lengths (a) for three different pump laser wavelengths (830, 800, and 770 nm) are shown to compare with the terahertz spectra (b).....	105
Figure 5.5 Typical transverse mode (a) and dispersion(b) of nonlinear PCF NL-770-2.0	109
Figure 5.6 Temporal evolution of laser pulse (a) and spectrum broadening (b) in SC generation.....	113

Figure 5.7 Spectrum broadening in a nonlinear PCF and terahertz spectrum. (a) spectrum broadening of femtosecond laser pulses within nonlinear PCF of different propagation distances. (b) Terahertz spectrum generated by optical rectification of SC. 114

Acknowledgements

First of all, I would like to express my warm and sincere thanks to my advisor, Professor Zhiwen Liu, for his help and support during my five years' Ph.D. study. Not only his profound knowledge but also his passion of research affected and finally changed my way of thinking. Looking back at the last five years, I always feel I am so fortunate and proud to be his student. This dissertation could not have been written without his encouragement and support.

I would like to express same gratitude to Professor Stuart (Shizhuo) Yin for his support my study in terahertz radiation project. I am also very thankful to Professor C. Russell Philbrick and Professor William O. Hancock for serving on my committee and for their valuable suggestion on my thesis. I wish to express my thanks to Professor Mark Cronin-Golomb and Professor Fiorenzo G. Omenetto at Tufts University for their help and useful discussion on optical tweezers calibration. I am also grateful to Professor L. Michael Hayden and Dr. Xuemei Zheng for their generous sharing the experience on terahertz experiments. It was also a great pleasure to discuss with Professor H. Daniel Ou-Yang and Professor Yujie Ding at the Lehigh University.

I would like to take this opportunity to thank my colleagues and friends for their enormous help on my work, including Dr. Kebin Shi, Haifeng Li, Qian Xu, Dr. Qin

Chen, Jae Hun Kim, Natalie Wolchover, Dr. Fei Wu, Meng-Ku Chen and many other friends at Penn State.

At the end, I will thank my parents for their understanding and support through all my life. Last, but not least, I should say thanks to my wife, Wenhua Yu. The love accompanied me through the writing of the whole dissertation.

Chapter 1 Introduction

Ultrafast optics is a rapidly developing branch of optics in recent years, which deals with the study and application of optical pulses and optical phenomena with ultrashort laser pulses [1, 2]. Ultrashort laser pulses, which refers to the pulses with duration at femtosecond (10^{-15} s) level and even shorter, have the special properties, such as ultrashort duration, high peak power, broad spectral bandwidth, short coherent length, and structured spectral coherence [2], which make them especially useful for a number of applications. The most obvious property of ultrashort pulses is short pulse duration, which is critical for time-resolved study of fast processes. Majority of applications use laser pulses with duration falling in the range of 100 fs to 1 ps, where the ability for time-resolve fast process is far greater than anything that can be achieved by means of conventional or state-of-the-art electronics. The extremely short pulse duration also implies that very high peak power can be generated even at moderate pulse energies. For example, a 100 fs pulse with energy of 1 nJ gives a peak power level of ~ 10 kW. When such a pulse is focused to a spot of $100 \mu\text{m}^2$, the intensity is on the order of $\sim 10 \text{ GW/cm}^2$, which is strong enough to observe many nonlinear optical phenomena, while the average power is maintaining at hundreds of milliwatts, which will not damage the sample. For ultrafast pulses with energy at microjoule or millijoule levels, the intensity after focusing can be more than $\sim 1000 \text{ TW/cm}^2$, which can induce ionization in the materials. This process has been applied to laser ablation and micromachining. Broad spectral bandwidth and short coherent

length is an essential property for ultrashort pulses as a result of the uncertainty principle. When ultrafast lasers are applied to optical coherent tomography (OCT), improvement in longitudinal resolution can be achieved. One other property of ultrashort pulsed lasers is the structured spectral coherence. In 2005, the Nobel Prize in physics was awarded to the research of frequency metrology, which processes the comb structure of laser pulses in temporal and frequency domain.

In my dissertation, I present three applications of the ultrafast femtosecond lasers: scattering spectroscopy of single micro/nano particle using supercontinuum white light tweezers, tunable femtosecond laser beam shaping and terahertz (THz) generation by optical rectification of femtosecond laser pulses.

The first part my dissertation is to study the single particle scattering spectroscopy using supercontinuum white light tweezers [3]. Spectroscopy has a long history and it has been widely used in research and industries. Since the ultrafast optical techniques were launched and advanced quickly, the spectroscopy techniques have made a huge revolution. Not only have many nonlinear optical spectroscopy techniques come to this expanding world, such as fluorescence spectroscopy and coherent Raman spectroscopy, but also the area linear optical spectroscopy has made a great improvement. Examples include reports of applications using sources of ultrabroad band supercontinuum (SC) [4-6] generated in highly nonlinear photonic crystal fibers [7] pumped by ultrafast laser pulses. Supercontinuum white light covers more than 1000 nm from UV to near-IR, yet it still keeps high intensity and high degree of

spatial coherence. It is a major enhancement over traditional broad band optical sources in linear optical spectroscopy. We developed the supercontinuum white light optical tweezers to perform single particle spectroscopy [3]. Unlike conventional spectroscopy, single particle spectroscopy can avoid ensemble averaging and it has the capability to probe the properties of individual particles (e.g., size, shape, refractive index, resonant absorption, chemical composition), which can lead to many important applications particularly in nanoparticle characterization and sensing. The supercontinuum white light optical tweezers system setup is described in Chapter 2. The scattering spectroscopy of single particles trapped by supercontinuum white light tweezers was firstly observed by our group. Scattering spectra of different particles have been measured and are presented in this dissertation. The properties of trapping forces in the supercontinuum white light optical tweezers are calibrated and results are presented.

In order to understand the scattering spectrum in the supercontinuum white light tweezers, Chapter 3 discusses theoretic models, which are constructed under various approximation conditions. When the scatterer is of spherical shape, modeling based on Mie's scattering theory [8] and angular spectrum decomposition will be described. In order to verify the model, a series of particularly designed experiments have been performed and results showed consistent with our theory analysis. This modeling can also be applied to nanoscaled metallic particle scatterer. The calculation results will be presented and the results will be discussed in my dissertation. For the arbitrary-shaped scatterers, when the size of the scatterer is small or the refractive index of the

scatterer is close to the surrounding medium, another modeling based on Born approximation and Green's function is derived. The comparisons of the results between these two models show consistency and are presented, together with calculation results.

Chapter 4 in my dissertation is dedicated to the study of the femtosecond beam shaping [9]. Some specific beam shapes, such as flat top rectangular profiles, are desirable in lithography, laser printing, optical data storage and many other applications, but the basic mode coming out of laser cavity is often of Gaussian profile. A flexible approach to producing relatively small flat-top profiles is to use a shaping phase element followed by a focusing (Fourier transform) lens. Gerchberg–Saxton (GS) [10] or improved GS algorithm [11] based on the desired wavelength is often used to obtain the phase element design. For femtosecond laser pulses, which cover bandwidth of tens of nanometers, the performance of beam-shaping a Gaussian beam into a flat-topped rectangular profile will be studied and discussed for practical realization. In the meantime, the convergence of the improved GS algorithm has been studied and the number of iterations is optimized for phase element design.

The third part of my dissertation, Chapter 5, is about terahertz (THz) generation by optical rectification of femtosecond laser pulses. THz radiation is an electromagnetic wave that is in the range between FIR and microwaves [12]. THz radiation is not only capable of penetrating tissues, fabrics, plastics and many other non-conducting materials without damage, but also for spectral fingerprinting of many materials of

interest such as cancer cells. THz has a splendid application future in biomedical imaging and security screening. Optical rectification of femtosecond pulse in second order nonlinear materials is a simple and widely used method to generate broadband THz radiation [13]. However the limitation is that the energy conversion efficiency from femtosecond pumping lasers to THz radiation is very low, usually at 10^{-6} [14]. One important reason is the absorption of nonlinear materials and highly dispersion, which breaks the phase matching condition and limits the interaction length. In my dissertation, a method using optical rectification of supercontinuum pulses generated in nonlinear photonic crystal fibers is proposed to improve the efficiency of THz generation in the desired frequency region by tuning the supercontinuum spectrum. Terahertz radiation generated with strategy is analyzed and simulated with numerical calculations by using the split step method.

Chapter 6 presents conclusions and suggests future research directions.

Chapter 2 Supercontinuum White Light Optical Tweezers

2.1 Introduction to Optical Tweezers

A strongly focused light beam can exert force to trap and manipulate microscopic objects [15-19]. This technology is named “optical tweezer”. Prior to the invention of optical tweezers, optical pressure on micron-sized particles was observed and studied in the early 1970s. In 1986, Arthur Ashkin, Steven Chu and their colleagues at AT&T Bell Lab introduced single-beam gradient force optical trap, which is known as the first optical tweezer [15, 16]. Developed rapidly during the last two decades, optical tweezers have found a wide range of applications in research fields of physics [20-27] and biology [16, 28-40].

Current technologies of optical tweezers have demonstrated the capability of trapping objects as small as tens of nanometers [41, 42] in size. The trapping forces, which usually depend on power and wavefront structures of the light beam, are typically at the pico-Newton level [43, 44]. Such a scale is ideal for manipulating macromolecular systems, such as biological cells, and probing their responses. By measuring mechanic force response of biopolymer, such as DNA and protein molecules, and cell membranes using optical tweezers, it has been revealed that the cell regulates gene transcription [45], inter- and intra-cellular signaling [46] and respiration during reproductions [47]. Optical tweezers are useful not only for selecting individual heterogeneous microbes, but also for applications in future

intracellular surgery [48]. More applications of optical tweezers in biological research and medical applications have been reviewed in detail [16, 30, 31]. Optical tweezers can also be used in studying interactions between colloidal particles [21] in the field of physical and colloidal science.

Optical tweezer technology has experienced huge progress, and has become more and more powerful and versatile. [17, 49-55] Meanwhile, efforts have been also made to combine optical tweezers technology with spectroscopy techniques, such as Raman spectroscopy [56, 57] and dark field spectroscopy [58], to probe properties of trapped particle.

The basic principle behind optical tweezers is photon momentum transfer during the light reflection and refraction. The momentum of photon is in the direction of light propagation. When light is reflected or refracted on the surface of an object, the direction of light propagation changes, which results in the photon momentum changing. At the same time, the object undertakes an equal momentum change in the opposite direction. This is how the force is exerted on the object by the light.

When the object size is larger than the trapping wavelength, the optical trapping forces can be explained by the geometric optics model, as shown in Figure 2.1. When the tightly focused laser beam hits a microsphere, the light rays are bent on the surface of the microsphere according to the laws of reflection and refraction. The total force on the microsphere can be decomposed into scattering force and gradient force. The scattering force is always pointing in the direction of laser beam propagation to

push object along that direction, while the gradient force, which is proportional to the gradient of the intensity, always pulls the object to the point of intensity peak if its refractive index is larger than that of the surrounding medium. In typical optical tweezers, the incoming lasers are working on TEM00 mode with a Gaussian intensity profile. This means the center of the beam has stronger intensity than the edges. When the axial gradient force is large enough to balance the scattering force, the microsphere will be trapped. In order to obtain strongly focused field, high numerical aperture objective lenses, where the gradient forces are overwhelming at focal spot, are always desired.

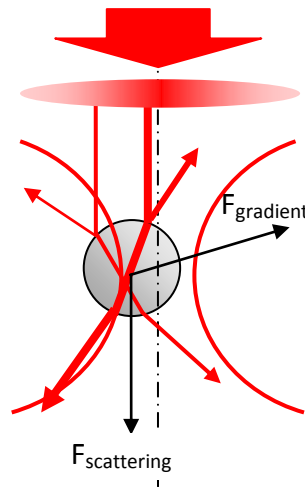


Figure 2.1 The principle of optical trapping

The geometric optics model, discussed above, is in good agreement with measured forces, if the diameter of the trapped object is well above the wavelength of the laser light; whereas, electromagnetic theory can be used for particles that are small compared with the wavelength. In the intermediate regime, where the particle sizes

are of the same order as the wavelength of the trapping laser, the electromagnetic theory yields better results than the geometric optics model.

In the electromagnetic model, when the size of the particle is smaller than wavelength, the external electric field of light will induce a dipole,

$$p = \alpha E \quad , \quad (2-1)$$

where p is the induced dipole, E is the electric field of light, α is the polarizability of particle. When this induced dipole moment interacts with electric field of light, the total energy of this system, U , is

$$U = -p \cdot E \quad . \quad (2-2)$$

Therefore the force, gradient force, is proportional to the gradient of the intensity of the laser field,

$$F = -\nabla U = \alpha \nabla E^2 \quad . \quad (2-3)$$

The electromagnetic theory can not only explain the dielectric particle trapping, but can be also apply to metallic particle trapping. Experiment has verified the metallic nano particles can be trapped. Furthermore metallic nanoparticle trapping shows more tightly than dielectric trapping, because the metallic particle is more easily polarized and has larger polarizability.

A basic optical tweezer setup is simple: light source, beam expansion and steering optics, high numerical aperture objective lens, sample cell holder, and imaging

equipment for observation. The trapping light sources are usually conventional continuous wave lasers, because the laser power stability is an essential factor. Optical tweezers using femtosecond pulsed laser have also been investigated recently. We introduced the white light supercontinuum optical tweezers [3] for the first time by using supercontinuum [5] generated from highly nonlinear photonic crystal fibers [7]. Many interesting properties and applications of white light supercontinuum optical tweezers are studied and discussed below.

2.2 Supercontinuum generation from photonic crystal fibers (PCF)

Supercontinuum generation is the process of the extremely broadening of spectrum when high intensity lasers interact with materials. Supercontinuum generation has been observed and studied in the bulk materials[59] and optical fibers[60, 61]. With the development of the photonic crystal fibers (PCF), supercontinuum generation was for the first time observed in highly nonlinear photonic crystal fiber pumped by femtosecond laser pulses in 2000 [5].

Photonic crystal fiber is a kind of microstructured optical fiber, in which optical wave can be confined by periodic air holes and propagates within core. The size of the core can be as small as 1~2 microns. Figure 2.2(a) shows the cross section of a typical photonic crystal fiber [62]. Thereby the nonlinearity of the fiber can be improved about an order of magnitude compared to conventional single mode fibers. Another advantage of photonic crystal fibers is that the group velocity dispersion (GVD)

property is adjustable by tuning the size and pitch of air holes in the cladding layers. With special design, the zero group velocity dispersion wavelength can be shifted from visible to near infrared region, which is a critical condition for supercontinuum generation over extremely broadband spectrum range.

When ultrashort, femtosecond to picosecond, laser pulses are coupled into highly nonlinear PCF, SC can be generated due to extremely intense nonlinear interaction between optical field and PCF material. The mechanisms behind the SC generation in highly linear PCF have been studied during the years since it was observed [6]. Supercontinuum generation in the highly nonlinear PCF can be categorized to two cases: pumping in the normal GVD regime and in the anomalous regime. When pumping laser pulses are located in the normal GVD regime of PCF, the physics of SC generation is similar to that from conventional optical fiber, which has the typical zero GVD wavelength in the near IR (about 1.3 μm). In this situation, self phase modulation (SPM), Raman scattering, cross phase modulation (XPM) and four wave mixing (FWM) are the major nonlinear optical process involved in SC generation [63-65]. As mentioned above, one of important properties of PCF's is that their GVD can be tuned by adjusting the pitches and sizes of air holes in the cladding layers. A specially designed PCF can shift the zero GVD wavelength to visible regime. As a result, a general femtosecond oscillator or picoseconds laser source can pump PCF's in their anomalous GVD regime. In this case that the highly nonlinear PCF is pumped at anomalous GVD regime, a broader SC spectrum can be obtained. That is because in the anomalous GVD regime, high frequency components travel faster than the

lower ones, while the SPM effect on the high intensity pulse will slow them down. When the effect of SPM and anomalous group velocity dispersion are balanced each other, an optical soliton can be formed. A series of soliton-related nonlinear processes are involved in SC generation, such as soliton fission [66, 67], soliton self frequency shift [68, 69], and dispersive wave generation [70]. Consequently, a broader SC spectrum can be obtained. SC generation in the following experiment belongs to this case. Figure 2.2(b) shows the far field image of a typical SC generated from PCF. The theoretical simulation of SC generation in PCF will be described in section 5.2.

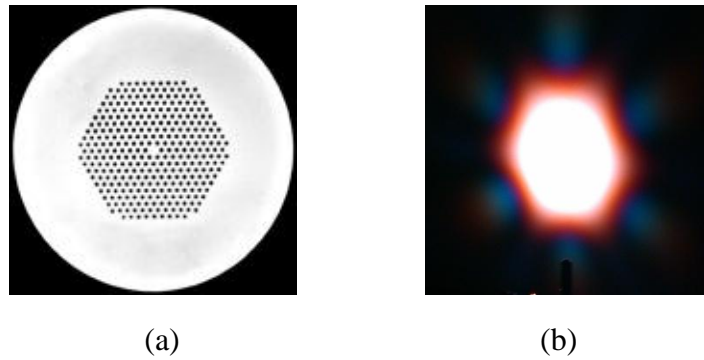
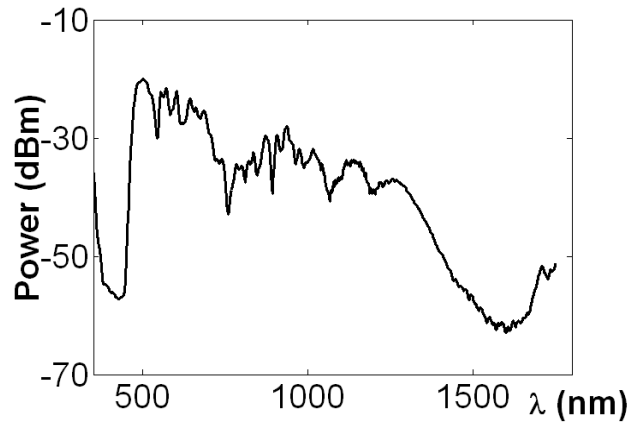


Figure 2.2 (a) Typical cross section of nonlinear PCF [Source: Crystal-Fibre] and (b) supercontinuum generation

Since the core of the photonic crystal fiber is very small, with a diameter usually of less than 5 μm , the supercontinuum light source has an intrinsic character, a high degree of spatial coherence, which is unique from other traditional white light sources, such as the Xe arc lamp. Therefore supercontinuum can be collimated to a plane wave and focused to a nearly diffraction limited spot. This makes the supercontinuum work more like a traditional laser but with ultra broad bandwidth. The unique property of a high degree of spatial coherence and extremely broadband spectrum of SC has made

it attractive in the applications of optical frequency metrology [71], optical coherent tomography [72], telecommunication [73], confocal imaging [74, 75] and spectroscopy [3, 76, 77].

Two types of supercontinuum white light sources were used in the dissertation work. In the first one, femtosecond laser pulses (average power ~ 400 mW, repetition rate ~ 88 MHz, pulse width ~ 64 fs) from a mode-locked Ti: Sapphire laser (KM Labs) are coupled into a short section (several centimeters long) of photonic crystal fiber (NL-2.0-770, Crystal-Fibre). A typical supercontinuum spectrum measured by an Ando optical spectrum analyzer is shown in Figure 2.3(a). In the second supercontinuum white light source, sub-nanosecond laser pulses from a passively Q-switched microchip laser (JDSU NP-10620-100, $\lambda=1064$ nm, average power ~ 70 mW) are coupled into a ~ 20 meter long photonic crystal fiber (BlazePhotonics SC-5.0-1064) to generate supercontinuum white light. Compared with the first source, it has less power but a much more uniform power spectrum as shown in Figure 2.3(b).



(a)

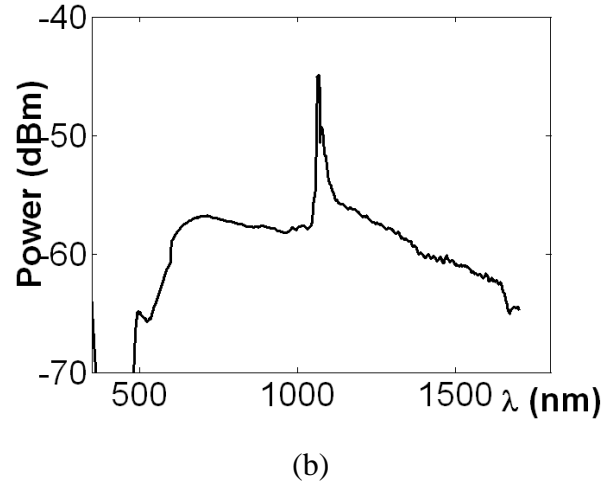


Figure 2.3 Typical spectrum of supercontinuum generated in highly nonlinear photonic crystal fibers (a) supercontinuum pumped by femtosecond laser pulses (b) supercontinuum pumped by subnanosecond laser pulses.

2.3 Supercontinuum White Light Optical Tweezer

Since the supercontinuum white light generated from highly nonlinear photonic crystal fibers has a high degree of spatial coherence, collimated supercontinuum beams perform like lasers. We demonstrated that strongly focused the supercontinuum white light is able to trap and manipulate mesoscopic scale objectives.

First collimated supercontinuum white light from the first SC source was tightly focused by an objective lens (Newport 60X/0.85 NA) into a sample cell filled with microspheres in solution. A non-inverted optical tweezer setup was used in our experiment. In Fig. 2.4, a silica microsphere of 4.82- μm -diameter (Bangs Laboratory) is trapped in 2D and manipulated in the lateral direction. In order to show the trapped microsphere, we blocked the supercontinuum white light intermittently during the experiments.

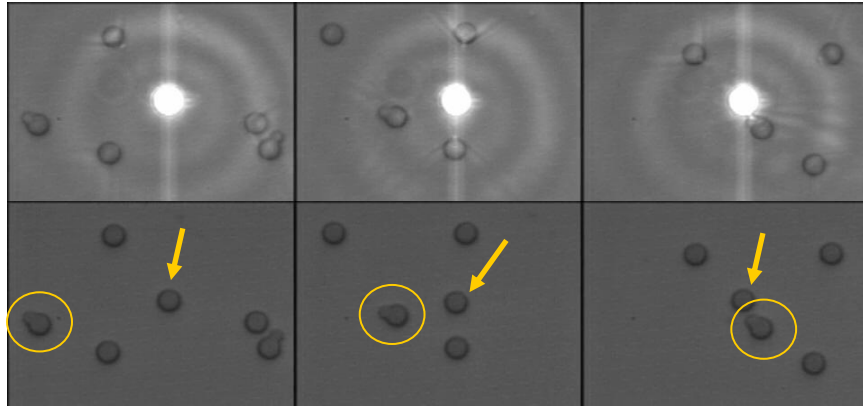


Figure 2.4 A 4.82- μm silica microsphere was 2D trapped by the white light tweezer.

To demonstrate 3D trapping by using supercontinuum, we constructed a downward optical tweezer (non-inverted) using the second supercontinuum source. The collimated white light was tightly focused by a Zeiss Plan-Neofluar oil immersion objective lens (63x/1.25 NA) into a sample cell filled with polymer microspheres suspended in water. A sequence of frames was captured, and these are shown in Figure 2.5 to demonstrate the 3D trapping of a 2- μm diameter microsphere. The first frame shows the initial positions of several microspheres before one of them was to be trapped. We mechanically translated the sample cell and moved one sphere (pointed by the arrow) toward where the white light was focused (frame 2). The sphere was then trapped and as a result the white light was strongly scattered (frame 3). Once it was trapped, it stayed there when we continued to move the sample cell with the other spheres in the lateral directions (frames 4, 5, and 6). In order to demonstrate the trapping along the axial direction, we moved the sample cell downwards (frames 7 and 8), and as expected all the other microspheres were

defocused. Finally, in the last frame we blocked the white light to show the trapped sphere and it is evident that it remained in the same place all the time. This clearly demonstrates the 3D trapping capability of the white light tweezers.

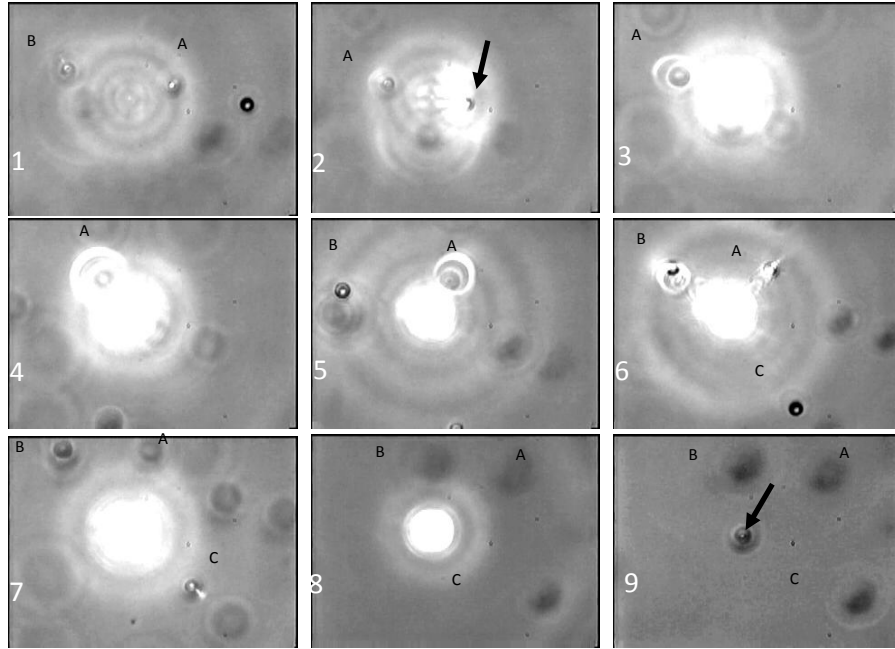
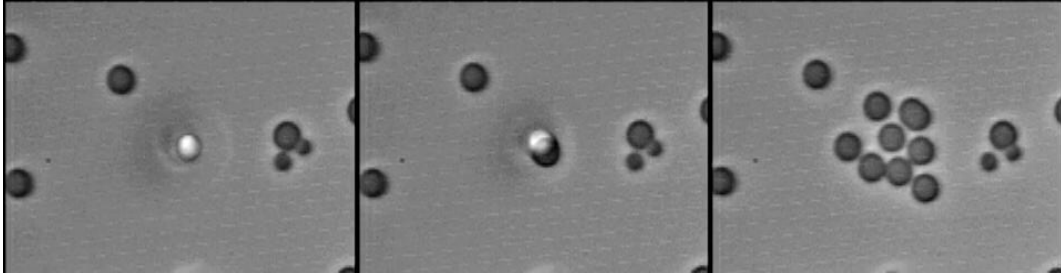


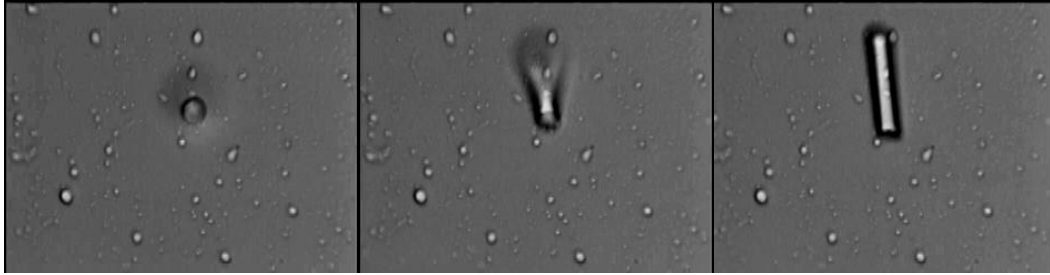
Figure 2.5 A 2- μm polymer microsphere was 3D trapped by the white light tweezer, and these particles are identified, A, B, and C, in the frame sequence. First three frames show the process of a sphere being trapped by the tightly focused supercontinuum white light, frames 4-6 show the trapping in the lateral plane, and the last three frames demonstrate the trapping in the axial direction.

Compared to conventional optical tweezers, the white light tweezer has a broader versatility in controlling the properties of an optical trap, especially in the axial direction, due to the extra degree of freedom - wavelength. To illustrate this idea, following our work on chromatic confocal microscopy [75], we insert a pair of singlet lenses, which form a telescope system, in order to purposely introduce chromatic aberration. As the result, different wavelengths are focused at slightly different axial

positions and therefore an extended depth of focus (EDOF) is obtained. The length of the EDOF depends on the amount of material dispersion and the bandwidth of the white light. Longer EDOF can be achieved by using a diffractive optical element such as a Fresnel lens. We used an inverted setup with chromatic aberration to lift and move multiple silica microspheres and to align micro- rods. The experimental results are given in Fig. 2.6 (a) and (b). In Fig. 2.6 (a) we temporally blocked the supercontinuum white light after 8 microspheres were lifted. The three frames show the falling of the spheres due to gravity. In Fig 2.6 (b) an initially aligned micro-rod fell down after the white light was temporally blocked. Stacking multiple microspheres and aligning micro-rods have previously reported using Gaussian [78] and Bessel beams [79]. Although the achievable depth of focus is shorter than that of a Bessel beam [55], it does not have the ring structure. In addition, the intensity distribution along the axial direction can be controlled by spectrally filtering the white light beam using a pulse shaper like setup. Furthermore, since different spectral components of the white light are focused at different axial positions, the relative position information of the lifted microspheres could be potentially retrieved by examining the back scattered light spectrum as in a chromatic confocal microscope.



(a)



(b)

Figure 2.6 Trapping and manipulation of microspheres and micro-rod using supercontinuum white light (a) the collapse of eight 5- μ m microspheres lifted by the inverted chromatic white light tweezer after blocking the white light. (b) the falling down of a micro-rod initially lifted and aligned by the inverted chromatic white light tweezer after blocking the white light.

It is interesting to perform spectroscopic measurements, particularly the optical scattering measurement, while the particle is being trapped and manipulated. As shown in Fig. 2.7, when we use the supercontinuum white light generated from the first SC source to 3D trap a 2- μ m-diameter polystyrene sphere with a high numerical aperture objective lens (Zeiss Plan-Neofluar 63x/1.25 N.A.), a colored scattering pattern was observed and captured by color CCD camera. Fig. 2.7 (a) is the background when no sphere was trapped and (b) is the scattering pattern of a 3D trapped latex sphere. Clearly, the presence of a three-dimensionally trapped sphere modified the spectrum dramatically.

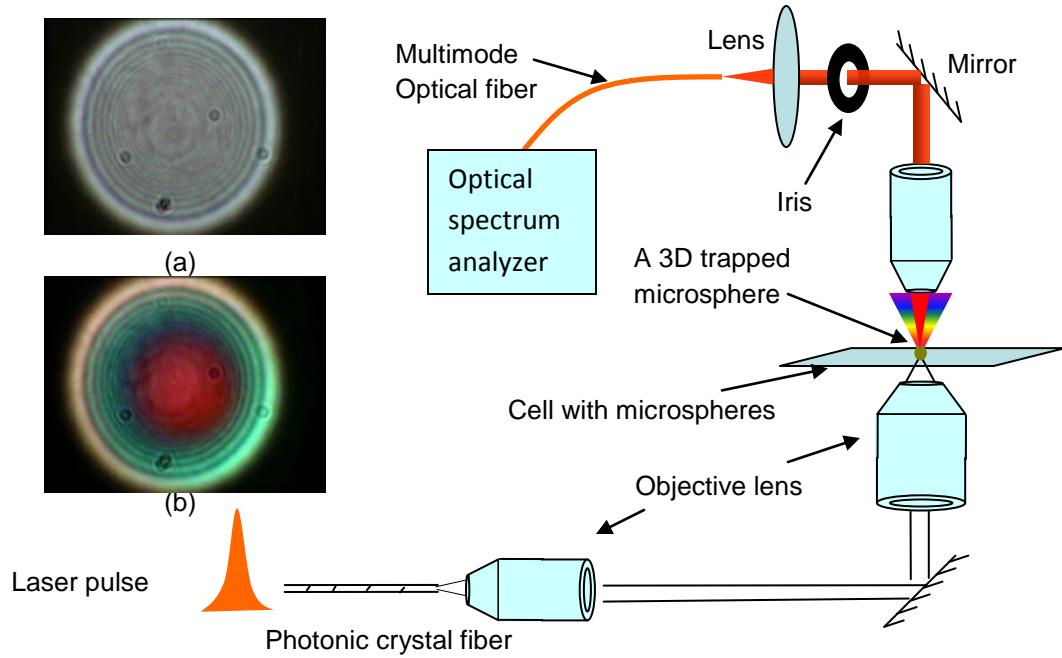


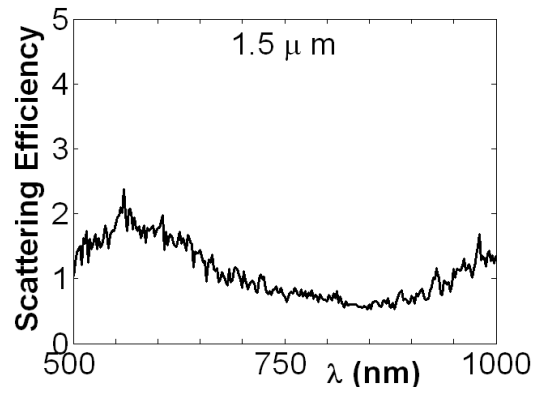
Figure 2.7 Schematic diagram of the experimental setup. The inserted pictures are (a) the background when no microsphere was trapped and (b) scattering pattern when a $2\mu\text{m}$ latex microsphere was three dimensionally trapped by an inverted white light tweezer using the femtosecond supercontinuum source.

To measure the optical scattering spectrum, we constructed an inverted tweezer with the second sub-nanosecond supercontinuum white light source because of its relative flat spectrum. An objective lens (Newport 10x/0.25 N.A.) is placed on the top to collect the transmitted light in the nearly forward direction. The numerical aperture of the collection system is limited to about 0.13 by the iris. Finally the spectrum of the transmitted light is measured by an optical spectrum analyzer (Ando 6315E).

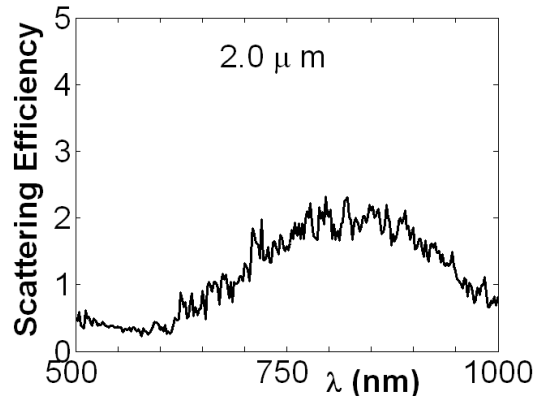
During the experiments, we first measured the signal spectrum of the transmitted light with a three dimensionally trapped microsphere. Next we measure the reference spectrum when no microsphere was trapped. We define the ratio between the signal

and reference as the scattering efficiency, which serves as a metric to describe how strongly the light is scattered at a certain wavelength. The scattering efficiency curves of microspheres with three different diameters are plotted in Fig. 2.8(a)-(c), respectively.

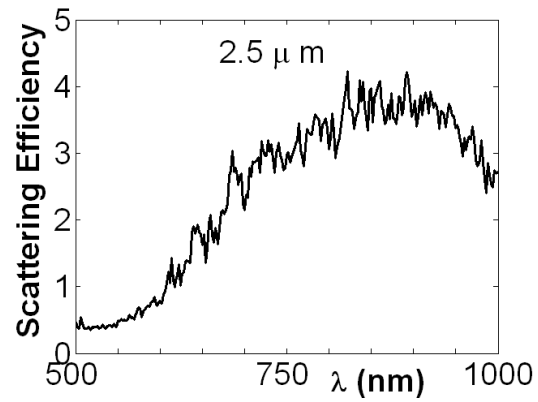
The jagged structure of the plot is primarily due to the oscillatory movement of the trapped microsphere. Each curve is the average of several traces which were obtained by repeated measurements of the same trapped microsphere. As the microsphere diameter increases from 1.5 μm to 2.5 μm , the peak is shifted to longer wavelength, i.e. 580 nm, 820 nm, and 900 nm respectively and the peak value of the scattering efficiency increases (from 1.8 to 4) as well.



(a)



(b)



(c)

Figure 2.8 Scattering efficiency curves. (a) – (c) are the scattering efficiency of three dimensionally trapped microspheres of diameter 1.5 μm , 2 μm and 2.5 μm respectively. Refractive index is 1.59 at $\lambda=589$ nm. The wavelength resolution is 10 nm.

2.4 Optical Tweezer Trapping Force Calibration- Stiffness Determination

Trapping force is one of the important properties of optical tweezers [80, 81]. The tightly focused optical field forms a three dimensional potential well. The trapping force always pulls the particles being captured toward the nadir of the potential well. The potential can be written in the forms of series expansion as,

$$U(x) = U(x_0) + \frac{1}{2} \kappa (x - x_0)^2 + \dots, \quad (2-4)$$

where x_0 is the equilibrium position and κ is the trap stiffness or spring constant in Hook's law $F = -\kappa(x - x_0)$. Since the forces come from the photon momentum transfer, the force is proportional to the power of trapping laser, and so is the stiffness.

A number of methods have been developed to measure the stiffness of the optical trapping, such as power spectrum measurement [82, 83], equipartition [18, 84], optical potential analysis [18], and drag force method [80]. Setups of first three measurements are similar. The trapped particle is imaged on a quadrant photodiode (QPD) in the forward direction. The photodiode quadrants are then summed pairwise, and differential signals are derived from the pairs for both x and y directions. When the size of probing bead is known and the trace of Brownian motion in a harmonic potential is recorded, the stiffness of the trapping can be calculated through one-sided power spectrum [82],

$$S_{xx}(f) = \frac{k_B T}{\pi^2 \gamma (f_0^2 + f^2)} , \quad (2-5)$$

where k_B is Boltzmann's constant, T is the absolute temperature, γ is the hydrodynamic drag coefficient, and f_0 is the rolloff frequency. The rolloff frequency f_0 depends on the trap stiffness κ by $f_0 = \kappa/2\pi\gamma$. The drag γ is given by the usual Stokes relation $\gamma = 6\pi\eta a$, where η is the viscosity of the medium and a is the radius of the bead. The stiffness of trap can be also obtained thermal fluctuations of the particle through the equipartition theorem [84],

$$\frac{1}{2} k_B T = \frac{1}{2} \kappa \langle x^2 \rangle . \quad (2-6)$$

The position variance, $\langle x^2 \rangle$, connects to the stiffness, κ , directly. An extension of the equipartition method is to analyze the complete distribution of the particle position in the potential well due to thermal motion. The probability of the displacement in the potential well is given by the Boltzmann distribution [18],

$$P(x) \propto \exp\left(\frac{-U(x)}{k_B T}\right) = \exp\left(\frac{-\kappa x^2}{2k_B T}\right) . \quad (2-7)$$

For all of these three methods, the bandwidths of position detection systems are required to record the power spectrum well beyond the rolloff frequency (in general, more than one order of magnitude). Since all of these three methods are based on the thermal dynamics of the particle, the temperature monitoring at focal point is very important during the measurement.

The drag force method directly measures the force balanced by viscous forces produced by the medium at the largest displacement from the equilibrium position. The sample cell is translated at known velocity perpendicular to the laser beam until the bead is left behind. The calibration force is [80]

$$F_{la} = 6\pi\eta a v k \quad , \quad (2-8)$$

where v denotes the velocity of the microscope stage during escape, and k is a factor that takes into account the finite distance from the upper and lower boundaries of the sample cell.

To calibrate the stiffness of the white light supercontinuum optical tweezers, we used the method invented by Nemet and Cronin-Golomb [85, 86], which is actually an extension of the drag force method. The trapped object scatters the trapping light and is confocally detected through a pinhole or an optical fiber placed in the imaging plane. When the optical trap is moved back and forth at small amplitude, the trapped particle is driven to move at the same frequency but with a phase lag due to the viscous drag of media. By measuring the phase lag, the stiffness of optical trapping can be determined.

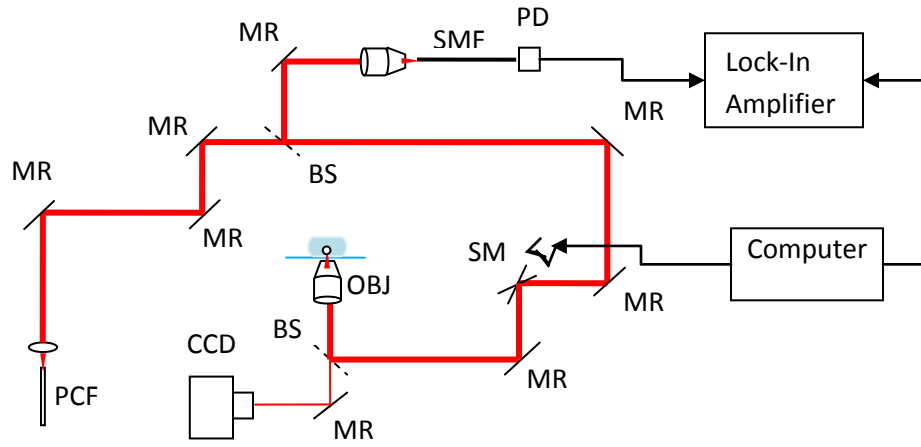


Figure 2.9 Schematic diagram of SC white light optical tweezer force measurement setup. PCF, photonic crystal fiber; OBJ, objective lens; MR, mirror; BS, beam splitter; SMF, single mode fiber; PD, photodiode detector; SM, scanning mirrors.

In December 2007, I went to Tufts University to calibrate the trapping stiffness of supercontinuum optical tweezers in Prof. Mark Cronin-Golomb and Prof. Fiorenzo Omenetto's lab. The experiment is performed on a modified trapping stiffness measurement system, which was used to calibrate the trapping stiffness of optical tweezer using a narrow band laser. Figure 2.9 shows the schematic diagram of experiment setup. A collimated supercontinuum beam generated from PCF (high delta PCF, silica, 2.6 micron core, zero GVD at 780nm) pumped by femtosecond laser pulses from a Ti:Sapphire mode locked laser is focused by Zeiss Plan-Neofluar oil immersion objective lens (63x/1.25 NA) into polystyrene microsphere solution. A pair of scanning mirrors (Cambridge Technologies) are used to steer the beam and move the trapping spot. Back scattered light from the trapped particle is confocally

measured by a photodiode detector through a single mode fiber placed at the imaging plane. A CCD camera monitors the motion of trapping spot and trapped particle. When the scanning mirrors are driven by computer signals and oscillate periodically at a given frequency, the confocal signal peak appears twice for each cycle, which corresponds to the second harmonic signal. A digital lock-in amplifier (Stanford Research System SR850) measures and records the phase difference between back scattering confocal signals and second harmonic of scanning mirrors driving signals.

In the following, the physics behind such a confocal system to measure the stiffness of optical trapping is described. One dimension (1-D) motion equation of a particle in a viscous fluid undertaking Brownian motion in an oscillating harmonic potential is given by [85, 86],

$$\gamma \frac{dx}{dt} + \kappa[x - p(t)] = L(t) , \quad (2-9)$$

where x is the particle's position, $p(t)$ is the position of trapping at time t , and $L(t)$ is the Langevin force function related to Brownian motion. γ is the hydrodynamic drag given by Stokes relation $\gamma = 6\pi\eta a$ [87] The mass times acceleration term is ignored since Reynolds number is very small for micron-sized particles where viscous drag dominates. Let $u = x - p(t)$ denote the relative position of particle to the center of trapping. If the optical trapping oscillates as sine wave, $p(t) = A \sin(\omega_0 t)$, Eq. (2-9) becomes

$$\gamma \frac{du}{dt} + \kappa u = -\gamma A \omega_0 \cos \omega_0 t + L(t), \quad (2-10)$$

where A and ω_0 are the amplitude and frequency of oscillation, respectively. When the oscillation amplitude is small, the confocal signal is proportional to $1 - \alpha u^2$, where α is an expansion coefficient. When the time constant of lock-in amplifier is set large enough, for example 10 s, the contribution from Brownian motion in the signal band where trapping oscillation dominates is very small and can be considered as noise. Therefore, the solution of Eq. (2-10) can be expressed as

$$u(t) = -u_0 \sin(\omega_0 t + \phi_1), \quad (2-11)$$

where $\phi_1 = \cot^{-1} \omega_0 \tau$ and $u_0 = A \omega_0 \tau / [1 + (\omega_0 \tau)^2]^{1/2}$, and $\tau = \gamma / \kappa$ is the relaxation time. The phase of the confocal detection signal of second harmonic appears as

$$\phi_2 = 2\phi_1 = 2 \cot^{-1} \omega_0 \tau. \quad (2-12)$$

We first measured the stiffness of white light supercontinuum optical tweezers with two different spectra, and the 2.9-micron-diameter polystyrene bead used as the probing particle. In order to reduce the media boundary effect on the viscosity, the microbead is 3D trapped far away from the water and glass interface. The time constant of digital lock-in amplifier is set to 10 s. The oscillation frequency is varied from 3.7 Hz to 303 Hz. First the coupling of femtosecond laser into a ~15 cm length of PCF (high delta, 2.6 micron core) is optimized to provide the highest output power. The power measured before the trapping objective lens is 16.5 mW and spectrum is

shown as blue line in Fig 2.10. The experiment results are plot as circles on the phase-vs- $1/f$ coordinate in Fig. 2.11(a). We use Matlab and OriginPro to look for the best fitting curve and the result are also plotted in the same figure as solid line. The stiffness, the calculated mean value of κ is 3.816 pN/ μm . After measurement, the PCF was tweaked at the input coupling end slightly to reduce the output power while SC spectrum changed. The power measured before the trapping objective lens is 15.5 mW and spectrum is shown as red line in Fig. 2.10. The experiment results and fitting curve are plotted in Fig. 2.11(b). The calculated mean value of stiffness of trapping, κ , is 4.804 pN/ μm . The results show the stiffness of low power white light supercontinuum is even stronger than that of high power. That is because optical field distribution of SC at the focal point is more complicated than that of a single wavelength trapping due to chromatic aberration of the optical system. The focal point of SC is the superposition of all the spectrum components. The chromatic aberration of optics is inevitable for such extremely broadband supercontinuum. The different wavelengths components are focused at different axial positions. The light beam of each wavelength component diverges away from its focal point, especially for tightly focused light beams using high NA objective lenses. That results in the effective focal point of SC being not as tight as that of single wavelength. Considering the fact that the spectrum of first SC is broader, this chromatic aberration effect is more obvious. Meanwhile, given same SC spectrum, the trap stiffness will still be proportional to the power.

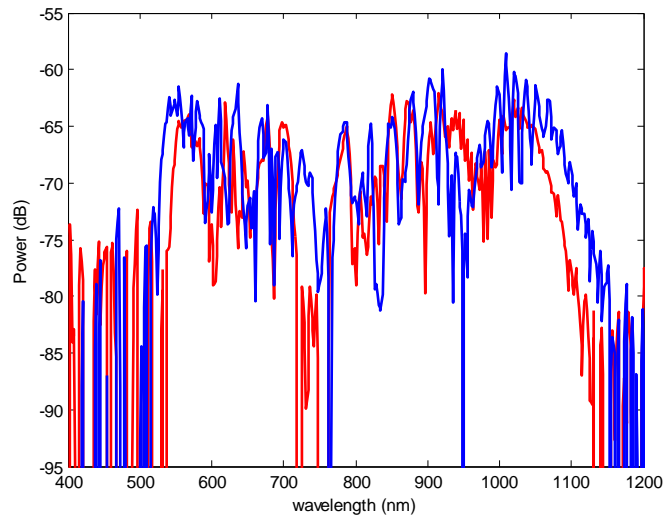
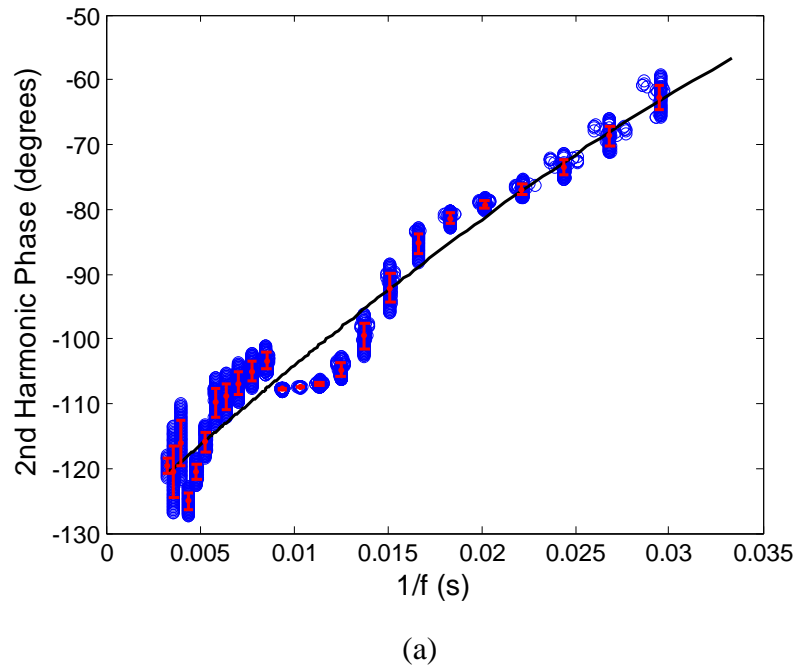


Figure 2.10 Spectra of supercontinuum pumped by femtosecond laser pulses



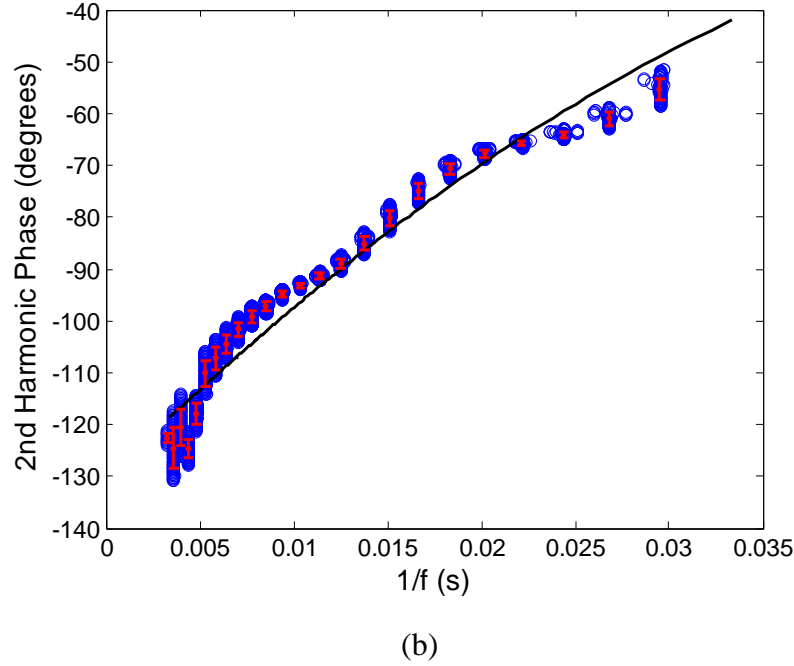


Figure 2.11 Second harmonic phase delay measurement results

To prove this point, we built another trapping stiffness calibration system at PennState, and setup is modified as shown in Fig. 2.12. Sub-nanosecond SC source is used in the experiment. Sub-nanosecond pulsed lasers from a passively Q-switched microchip laser (JDSU NP-10620-100, $\lambda=1064$ nm, average power ~ 70 mW) is reflected by a narrow band mirror for 1064 nm wavelength (CASIX) and then coupled into a ~ 16 meter long photonic crystal fiber (BlazePhotonics SC-5.0-1064) to generate supercontinuum white light. The output end of PCF is fixed to a piezoelectric actuator (AE0505D18, Thorlabs). Collimated SC white light is steered up and focused by Zeiss Plan-Neofluar oil immersion objective lens (63x/1.25 NA) to trap particles. The highly nonlinear PCF is used to also confocally detect backward scattering SC light. The backward scattering SC goes through 1064 nm narrow band

mirror and is detected by a photodiode detector. When computer sends sinusoidal signal to drive piezo-electric actuator to vibrate, the optical trap oscillates as a result. Confocally detected signals are sent to a digital lock-in amplifier to measure the phase at the second harmonic. A CCD camera is used to monitor the trapping. 4.82 μm diameter microbeads (Bangs Laboratories) are trapped right above surface of the glass slide. Therefore the boundary effect on the hydrodynamic drag γ must be taken into account. Faxen's law gives the proximate drag on a sphere near a surface [33]:

$$\gamma = \frac{6\pi\eta a}{1 - \frac{9}{16}\left(\frac{a}{h}\right) + \frac{1}{8}\left(\frac{a}{h}\right)^3 - \frac{45}{256}\left(\frac{a}{h}\right)^4 - \frac{1}{16}\left(\frac{a}{h}\right)^5}, \quad (2-13)$$

where h is distance of sphere center above the surface.

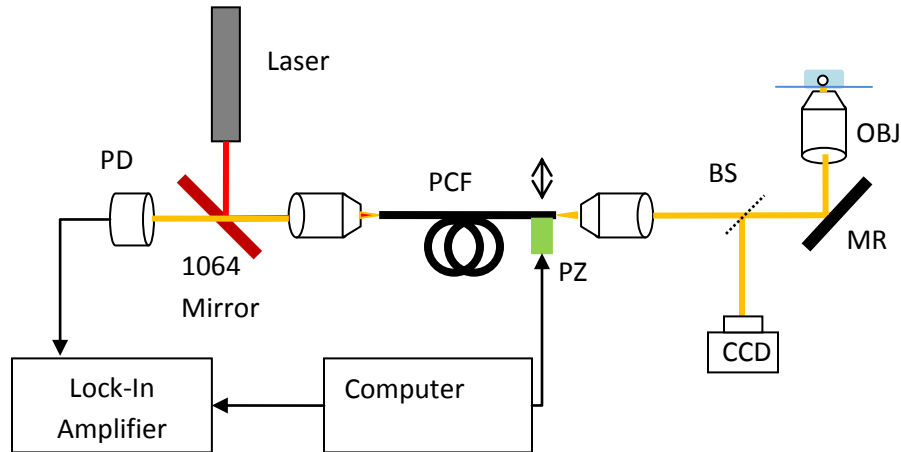


Figure 2.12 Schematic diagram of modified white light SC trapping force measurement setup. MR, mirror; OBJ, objective lens; BS, beam splitter; PZ, piezoelectric actuator; PD, photodiode detector.

The experimental procedure is described below: first we optimize the coupling into the PCF to obtain highest SC output power. The power of SC for trapping is 16 mW and spectrum is plotted as blue line in Fig. 2.13. The trapping oscillation frequency is varied from 30 Hz to 300 Hz. The experimental results are plotted as circles on the phase-vs-1/f coordinate in Fig. 2.14(a). After curve fitting, the mean value of trapping stiffness, κ , is calculated as 32.76 pN/ μm . An OD0.08 neutral density filter (83.2% Transmission) is inserted before high-NA trapping objective lens. The power of SC for trapping is reduced to 13.5 mW and its spectrum is plotted as green line in Fig. 2.13. The experiment and fitting results are plotted in Fig. 2.14(b). The mean value of trapping stiffness, κ , is calculated as 25.11 pN/ μm . Then the neutral density filter is inserted before the PCF. Consequently the SC spectrum changed, shown as red curve in Fig. 2.13, and total power changed to 12 mW. The experiment and fitting results are plotted in Fig. 2.14(c). The mean value trapping stiffness, κ , is calculated as 27.14 pN/ μm . The first two SC spectra are uniformly attenuated for all the wavelengths, therefore the trapping stiffness is still proportional to the total power, which is similar to the single wavelength optical trapping. For the third SC, the power becomes lower, however, spectrum is narrower. The experiment results show, as we expected, that the trapping stiffness is even higher than that of the second trapping. The trapping stiffness of white light SC is strongly dependent on the spectrum of SC.

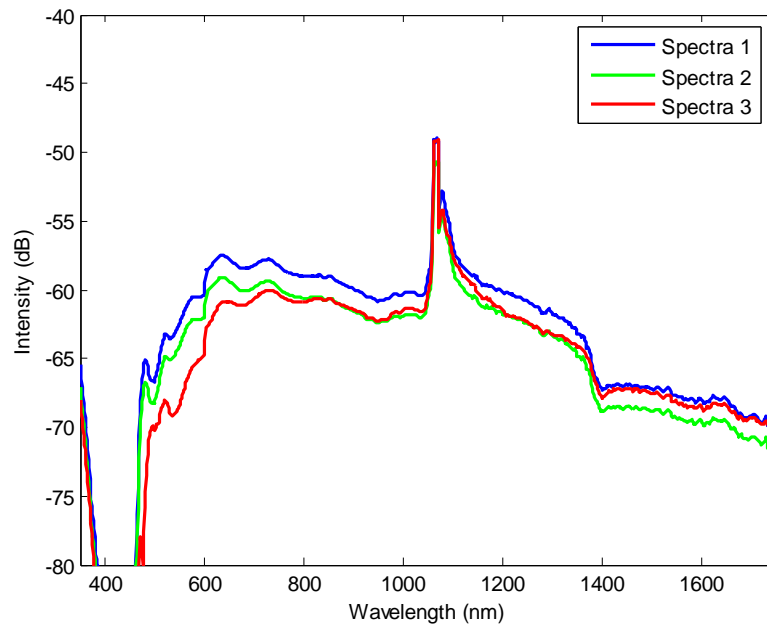
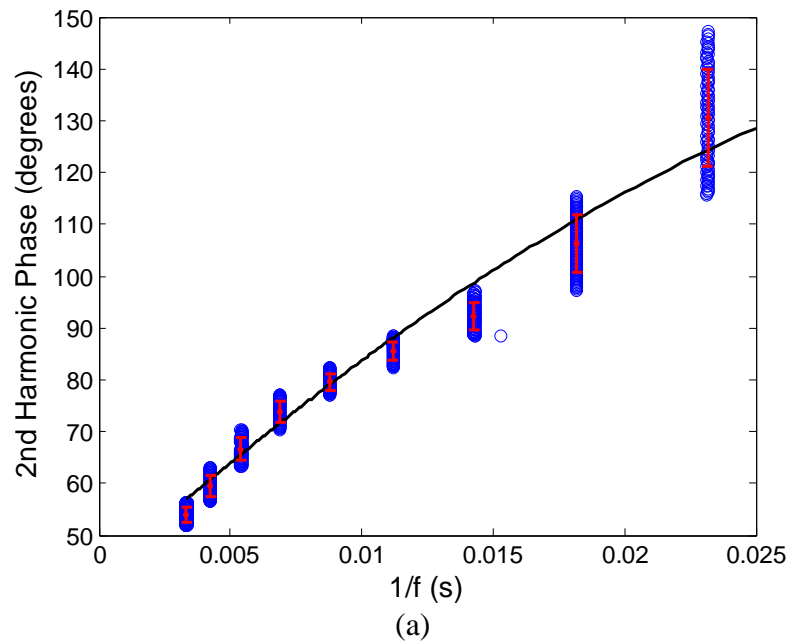
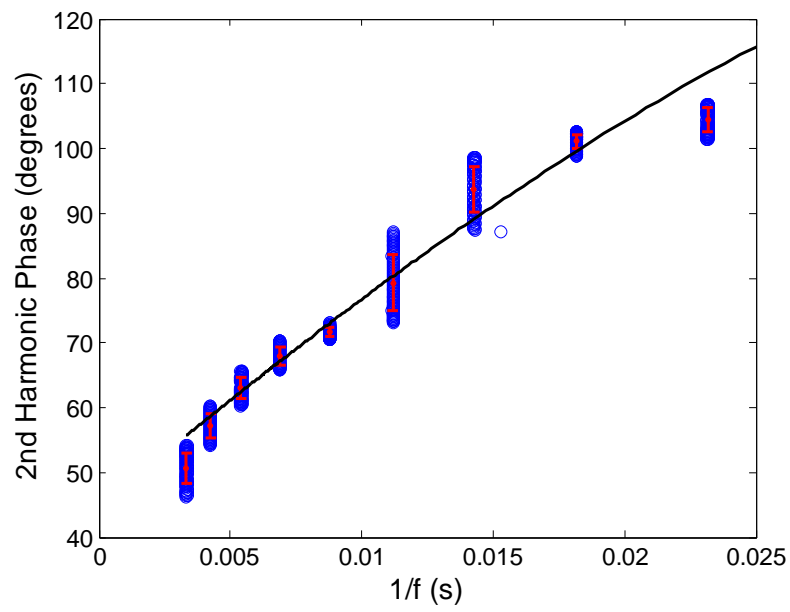
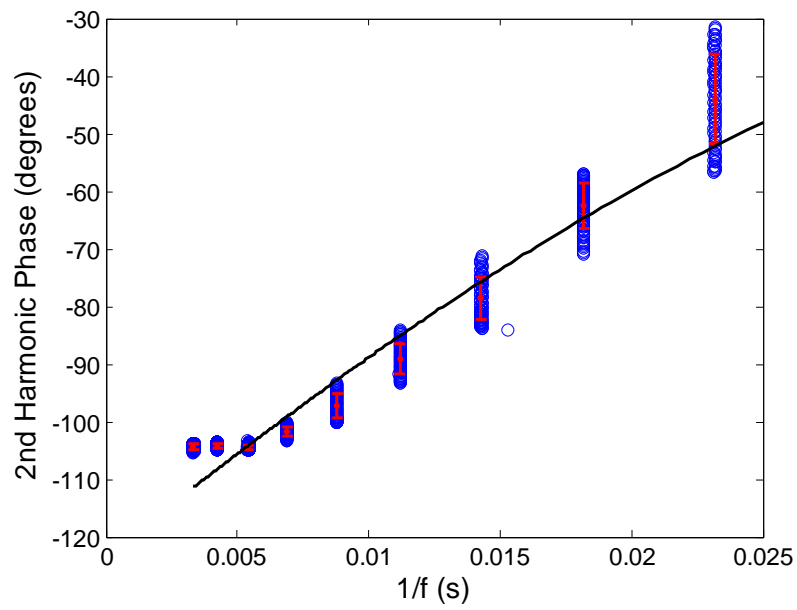


Figure 2.13 Spectra of supercontinuum pumped by sub-nanosecond laser pulses





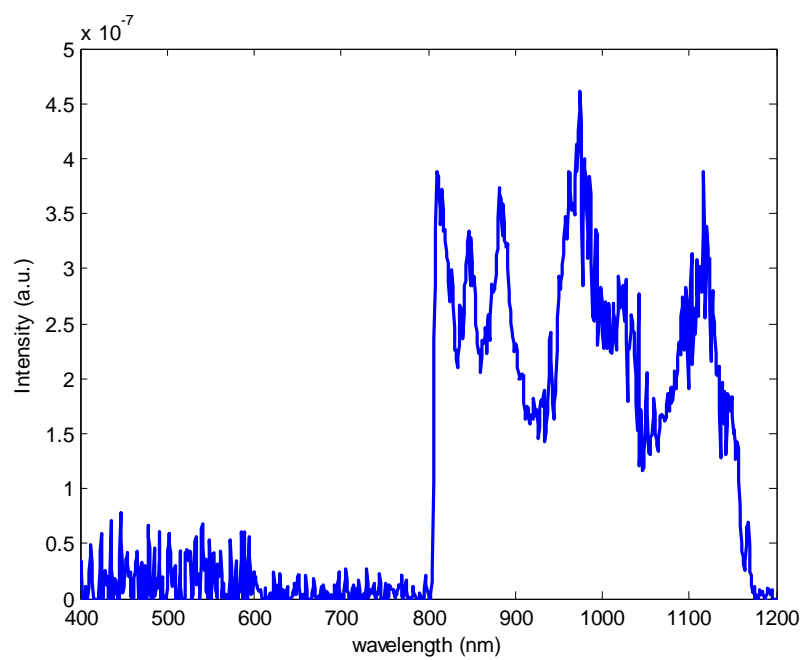
(b)



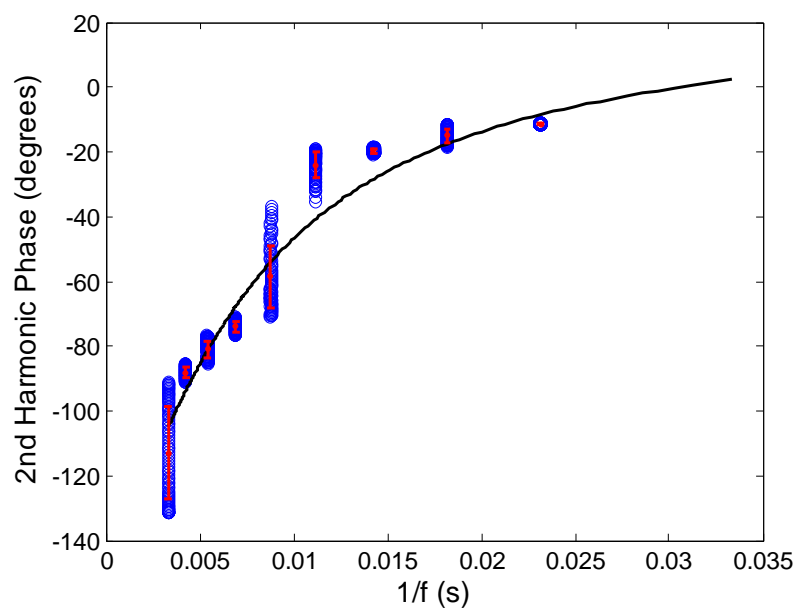
(c)

Figure 2.14 Second harmonic phase vs. $1/f$ curves

SC white light optical tweezers have also been demonstrated to have the capability of trapping metallic nano-sized particles in lateral directions. Same strategy has been used to measure the trapping stiffness when a 100 nm diameter gold particle is trapped by SC white light tweezers. The experiment setup is similar to that shown in Fig. 2.12. Femtosecond laser pulses (average power ~ 550 mW, repetition rate ~ 88 MHz, pulse width ~ 64 fs) from a mode-locked Ti: Sapphire laser (KM Labs) are reflected by a 808 nm long pass filter (Semrock LP02-808RU), instead of 1064 nm mirror in Fig. 2.12, and coupled into a ~ 40 cm long PCF (NL-2.0-770, Crystal-Fibre). Since the wavelength components shorter than the localized plasmon resonance frequency of the particle will repel the particle away, only the long wavelength components can be used to trap nanosized metal particles [58]. As a consequence, a long pass filter (HQ810LP Chroma) is used to remove the short wavelength components. SC spectrum after filter is shown in Fig. 2.15(a) with total power ~ 31 mW. SC is focused by a Zeiss apochromat objective lens (100x/1.32NA) into 100-nm-sized gold nanoparticle solution. Gold nanoparticles are pushed to top surface of sample cell and trapped in the lateral directions. The trapping stiffness measurement results and fitting curve are shown in Fig. 2.15(b). The mean value of trapping stiffness, κ , is calculated as 2.38 pN/ μm , where the approximate drag near a surface is given by Eq. (2-13).



(a)



(b)

Figure 2.15 Trapping stiffness measurement of a 100-nm-sized gold particle trapped by SC optical tweezers. (a) SC spectrum used for gold nanoparticle trapping (b) measurement results (circles) and fitting curve (solid line)

2.5 Summary

In this chapter, the optical tweezers and supercontinuum generation technologies are first reviewed. It is demonstrated that white light supercontinuum optical tweezers are able to trap and manipulate mesoscopic objects by taking advantage of the high degree of spatial coherence and high power of supercontinuum generated from highly nonlinear photonic crystal fibers pumped by ultrashort laser pulses.

Since supercontinuum covers extremely broadband spectrum (over 1000 nm), spectroscopy techniques are easily combined with white light supercontinuum optical tweezers. Linear scattering spectra of trapped particles are measured and presented. This shows the potentials of probing characteristics, such as size, shape, refractive index, and chemical components, of an individual particle by linear and nonlinear spectroscopy techniques in the future.

Trapping stiffness of white light supercontinuum optical tweezers has also been calibrated for both dielectric and metallic bead. The measurement results show the stiffness of white light supercontinuum optical tweezers not only depends on the total power but also the spectrum. Broader spectra may reduce the stiffness due to the effect of chromatic aberration of optics.

Chapter 3 Single-particle optical scattering spectroscopy in white light supercontinuum optical tweezers

3.1 Background

As demonstrated in Chapter 2, tightly focused supercontinuum can trap a particle, and at the same time to obtain scattering spectrum of the particle. In contrast to some conventional spectroscopy techniques, single particle spectroscopy using white light supercontinuum optical tweezers avoids ensemble averaging and has the capability to probe the properties of individual particles (e.g., size, shape, refractive index, resonant absorption, chemical composition). This obviously leads to many important applications, particularly in nanoparticle characterization and sensing. To further explore the potential of single particle spectroscopy with focused supercontinuum illumination, theoretical modeling tools need to be developed.

Optical scattering by a spherical scatterer in a focused narrow-band laser beam has been studied for many years [88-96]. For instance, generalized Lorentz-Mie theory (GLMT) can be used to study the scattering of a single spherical scatterer in a focused Gaussian beam [90-96]. We have recently developed a theoretical model to study scattering by a uniform spherical scatterer in a supercontinuum optical trap based on Mie's scattering theory and Fourier angular spectrum representation [97]. Fourier angular spectrum representation can be used to describe strongly focused beam, and has been applied to investigate scattering in optical tweezers [98], reflection at media

interface [99], and confocal imaging [100]. In this chapter, we apply the angular spectrum analysis and the Mie scattering theory to investigate optical scattering spectroscopy of a single spherical scatterer illuminated with tightly focused supercontinuum source. The scattered field is obtained by the linear superposition of the scattered fields produced by each of the Fourier angular component of the tightly focused incident field. The theory is compared with experiment. The effect of chromatic aberration is also considered. Numerical calculations of both polymer microspheres and metallic nanoparticles are presented. Next, we show that Born approximation method [101] can be used to calculate the scattered field produced by a non-spherical-shaped weak scatterer (e.g., when the refractive index of the scatterer is close to that of the surrounding medium, or the size of the scatterer is much smaller than the wavelength).

3.2 Theoretical Model Based on Mie Theory and Angular Spectrum Decomposition

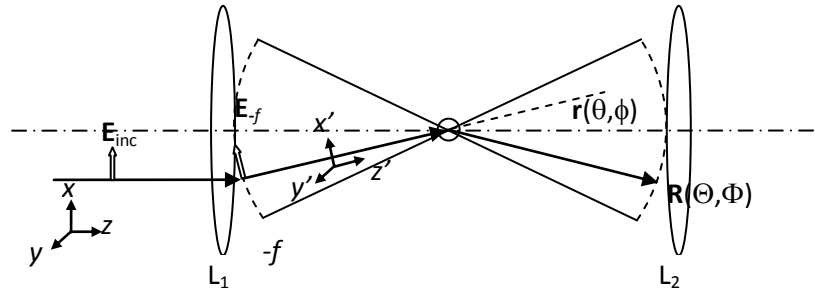


Figure 3.1 Schematic diagram of optical scattering by using tightly focused supercontinuum. A linearly-polarized incoming supercontinuum is tightly focused by objective lens L_1 . The scattered light produced by a spherical scatterer is collected by objective lens L_2 and analyzed by a spectrometer.

Figure 3.1 shows a schematic diagram of a typical forward optical scattering measurement system using a tightly focused supercontinuum source. An incoming supercontinuum beam, which is linearly polarized along the x-direction and propagates in the z direction, is strongly focused by a high-numerical-aperture objective lens L_1 ($NA = n\sin\theta_m$), with focal length f . We first consider a single wavelength component (λ_0 in vacuum) of the white light supercontinuum. Let us choose the geometrical focal point as the origin of our coordinate system. At the same time a spherical coordinate is constructed. The tightly focused electric field in the vicinity of focal point can then be expressed in terms of its Fourier angular spectrum,

$$\mathbf{E}(\mathbf{r}) = \iint \tilde{\mathbf{E}}(\mathbf{k}_i) e^{j\mathbf{k}_i \cdot \mathbf{r}} dk_{ix} dk_{iy} = \int_0^{2\pi} \int_0^{\theta_m} \tilde{\mathbf{E}}(\mathbf{k}_i) e^{j\mathbf{k}_i \cdot \mathbf{r}} k^2 \sin\theta \cos\theta d\theta d\phi, \quad (3-1)$$

where $k = 2\pi/\lambda$ is the wave number, $\lambda = \lambda_0/n$ is wavelength in the medium with refractive index n . $\mathbf{k}_i = k(\sin\theta \cos\phi \hat{\mathbf{x}} + \sin\theta \sin\phi \hat{\mathbf{y}} + \cos\theta \hat{\mathbf{z}})$ is the incident wave vector and θ, ϕ are the polar and azimuthal angles, respectively. $\tilde{\mathbf{E}}(\mathbf{k}_i)$ is the spatial spectrum of the electrical field, which can be expressed in terms of the far field $\mathbf{E}_f(\theta, \phi)$ on the reference sphere $-f$ [102].

$$\tilde{\mathbf{E}}(\mathbf{k}_i) = -\frac{j\lambda}{(2\pi)^2} \left(\frac{1}{\cos\theta} \right) f e^{jkf} \mathbf{E}_f(\theta, \phi). \quad (3-2)$$

Here we assume the incoming beam is a plane wave with a uniform electric field distribution $\mathbf{E}_{inc} = E_0 \hat{\mathbf{x}}$. $\mathbf{E}_f(\theta, \phi)$ can be obtained by taking account of the refraction of objective lens

$$\mathbf{E}_{-f}(\theta, \phi) = \sqrt{\cos \theta} \times \mathbf{RL} \cdot \mathbf{E}_{inc}(\theta, \phi) \quad (3-3),$$

where $\sqrt{\cos \theta}$ is introduced due to energy conservation for an aplanatic lens [103].

$$|\mathbf{E}_{inc}(\theta, \phi)|^2 f \sin \theta d\phi \times d(f \sin \theta) = |\mathbf{E}_{-f}(\theta, \phi)|^2 f \sin \theta d\phi \times d(f \theta) \quad (3-4)$$

RL is the matrix to calculate the refraction of lens L_1 in the form of

$$\mathbf{RL} = \begin{pmatrix} \cos \theta \cos^2 \phi + \sin^2 \phi & (\cos \theta - 1) \cos \phi \sin \phi & \sin \theta \cos \phi \\ (\cos \theta - 1) \cos \phi \sin \phi & \cos \theta \sin^2 \phi + \cos^2 \phi & \sin \theta \sin \phi \\ -\sin \theta \cos \phi & -\sin \theta \sin \phi & \cos \theta \end{pmatrix}. \quad (3-5)$$

Substituting Eq. (3-5) into Eq. (3-3), we can obtain

$$\mathbf{E}_{-f}(\theta, \phi) = E_0 \sqrt{\cos \theta} [(\cos \theta \cos^2 \phi + \sin^2 \phi) \hat{\mathbf{x}} + (\cos \theta - 1) \cos \phi \sin \phi \hat{\mathbf{y}} - \sin \theta \cos \phi \hat{\mathbf{z}}] . \quad (3-6)$$

Let us now first consider optical scattering caused by the presence of a spherical object located at the focal point of the objective lens L_1 . Since the field near the focal point can be thought of as the superposition of many plane wave components, $\tilde{\mathbf{E}}(\mathbf{k}_i)$, like Eq. (3-1), the scattered field can be obtained by coherently superimposing the scattered fields produced by each plane wave component, and can be calculated by using Mie theory. For each plane wave component, we define a rotated coordinate system (denoted with a prime) such that the plane wavelet is polarized along the x' direction and travels along the z' direction in the new coordinate system (the standard configuration used in Mie theory). So the unit vectors $\hat{\mathbf{x}}'$, $\hat{\mathbf{y}}'$, and $\hat{\mathbf{z}}'$ can be presented in the general fixed coordinate as

$$\hat{\mathbf{x}}' = (\cos \theta \cos^2 \phi + \sin^2 \phi) \hat{\mathbf{x}} + (\cos \theta - 1) \cos \phi \sin \phi \hat{\mathbf{y}} - \sin \theta \sin \phi \hat{\mathbf{z}}, \quad (3-7a)$$

$$\hat{\mathbf{z}}' = \sin \theta \cos \phi \hat{\mathbf{x}} + \sin \theta \sin \phi \hat{\mathbf{y}} + \cos \theta \hat{\mathbf{z}}, \quad (3-7b)$$

$$\hat{\mathbf{y}}' = \hat{\mathbf{z}}' \times \hat{\mathbf{x}}' = (\cos \theta - 1) \cos \phi \sin \phi \hat{\mathbf{x}} + (\cos \theta \sin^2 \phi + \cos^2 \phi) \hat{\mathbf{y}} - \sin \theta \sin \phi \hat{\mathbf{z}}, \quad (3-7c)$$

Any vector \mathbf{v} in the stationary coordinate system can be expressed in the terms of projections in the directions of $\hat{\mathbf{x}}'$, $\hat{\mathbf{y}}'$, and $\hat{\mathbf{z}}'$

$$\mathbf{v} = (\mathbf{v} \cdot \hat{\mathbf{x}}') \hat{\mathbf{x}}' + (\mathbf{v} \cdot \hat{\mathbf{y}}') \hat{\mathbf{y}}' + (\mathbf{v} \cdot \hat{\mathbf{z}}') \hat{\mathbf{z}}', \quad (3-8)$$

or written in the matrix form as

$$\mathbf{v}' = \mathbf{M} \cdot \mathbf{v}, \quad (3-9),$$

where \mathbf{M} is the transformation matrix given by

$$\mathbf{M} = \begin{pmatrix} \cos \theta \cos^2 \phi + \sin^2 \phi & (\cos \theta - 1) \cos \phi \sin \phi & -\sin \theta \cos \phi \\ (\cos \theta - 1) \cos \phi \sin \phi & \cos \theta \sin^2 \phi + \cos^2 \phi & -\sin \theta \sin \phi \\ \sin \theta \cos \phi & \sin \theta \sin \phi & \cos \theta \end{pmatrix}. \quad (3-10)$$

The scattered field decays with propagation distance. For each Fourier angular spectrum component $\tilde{\mathbf{E}}(\mathbf{k}_i)$, the scattered wavelet along at the measurement position \mathbf{R} , $R(\sin \theta \cos \phi \hat{\mathbf{x}} + \sin \theta \sin \phi \hat{\mathbf{y}} + \cos \theta \hat{\mathbf{z}})$ along the direction (θ, ϕ) is named as $\mathbf{E}_s(\mathbf{R}; \mathbf{k}_i)$, which can be calculated using the Mie Theory. First we use Eq. (3-10) to represent \mathbf{R} in the rotating system as $\mathbf{R}' = R'(\sin \theta' \cos \phi' \hat{\mathbf{x}}' + \sin \theta' \sin \phi' \hat{\mathbf{y}}' + \cos \theta' \hat{\mathbf{z}}') = \mathbf{M} \cdot \mathbf{R}$, where θ' and ϕ' are the polar and azimuthal angles, respectively, in the rotated coordinate system.

From Mie's theory, in the rotated coordinate system the scattered field is given by

$$\mathbf{E}'_s(\mathbf{R}') = \frac{je^{jkR'}}{kR'} \times \left[-\frac{j}{(2\pi)^2} \frac{\lambda}{\cos\theta} fe^{jkf} E_0 \sqrt{\cos\theta} \right] \begin{pmatrix} \sin^2 \Phi' S_1(\Theta') + \cos\Theta' \cos^2 \Phi' S_2(\Theta') \\ -\cos\Phi' \sin \Phi' S_1(\Theta') + \cos\Theta' \cos\Phi' \sin \Phi' S_2(\Theta') \\ -\sin \Theta' \cos\Phi' S_2(\Theta') \end{pmatrix} \quad (3-11)$$

where S_1 and S_2 are the scattering functions for the out-of-plane and in-plane components respectively[8], and are defined as

$$\begin{aligned} S_1(\Theta') &= \sum_{n=1}^{\infty} \frac{2n+1}{n(n+1)} [a_n \pi_n(\cos\Theta') + b_n \tau_n(\cos\Theta')] \\ S_2(\Theta') &= \sum_{n=1}^{\infty} \frac{2n+1}{n(n+1)} [b_n \pi_n(\cos\Theta') + a_n \tau_n(\cos\Theta')] \\ \pi_n(\cos\Theta') &= \frac{P_n^1(\cos\Theta')}{\sin\Theta'} \quad \tau_n(\cos\Theta') = \frac{dP_n^1(\cos\Theta')}{d\Theta'} \\ a_n &= \frac{\psi'_n(mka)\psi_n(ka) - m\psi_n(mka)\psi'_n(ka)}{\psi'_n(mka)\zeta_n(ka) - m\psi_n(mka)\zeta'_n(ka)} \quad b_n = \frac{m\psi'_n(mka)\psi_n(ka) - \psi_n(mka)\psi'_n(ka)}{m\psi'_n(mka)\zeta_n(ka) - \psi_n(mka)\zeta'_n(ka)} \end{aligned} \quad (3-12)$$

where P_n^m is the associated Legendre function, ψ_n and ξ_n are Riccati-Bessel function which are defined as $\psi_n(\rho) = \rho j_n(\rho)$, $\xi_n(\rho) = \rho h_n^{(1)}(\rho)$, where $j_n(\rho)$ and $h_n^{(1)}(\rho)$ are the spherical Bessel and Hankel functions of first kind respectively, a is the radius of the sphere, and m is the ratio between refractive index of the sphere to that of the surrounding medium. Transformed back to the fixed coordinate system, the scattered field is given by

$$\mathbf{E}_s(\mathbf{R}; \mathbf{k}_i) = \mathbf{E}_s(\Theta, \Phi; \theta, \phi) = \mathbf{M}^{-1} \cdot \hat{\mathbf{E}}'_s(\mathbf{M} \cdot \mathbf{R}). \quad (3-13)$$

The total scattered field is then the coherent superposition of the scattered field produced by each plane wave component,

$$\mathbf{E}_s(\Theta, \Phi) = \int_0^{2\pi} \int_0^{\theta_m} \mathbf{E}_s(\Theta, \Phi; \theta, \phi) k^2 \sin \theta \cos \theta d\theta d\phi. \quad (3-14)$$

We also need to consider the incident field propagating in the detection region when Θ is less than maximum incident angle θ_m ,

$$\mathbf{E}_I(\Theta, \Phi) = -j\tilde{\mathbf{E}}(\Theta, \Phi) \frac{(2\pi)^2}{\lambda} \cos \Theta \frac{e^{jkR}}{R}. \quad (3-15).$$

So the total optical intensity to be detected in this direction is the coherent sum of scattered field and incident field

$$I(\Theta, \Phi; \lambda_0) = \frac{n c \epsilon_0}{2} \left| \int_0^{2\pi} \int_0^{\theta_m} \mathbf{E}_s(\Theta, \Phi; \theta, \phi) k^2 \sin \theta \cos \theta d\theta d\phi + \mathbf{E}_I(\Theta, \Phi) \right|^2. \quad (3-16)$$

If an objective lens L_2 with numerical aperture $NA = n \sin \Theta_m$ is used to collect the forward scattered light (as shown in Figure 1), the detected power is given by

$$P(\lambda_0) = R^2 \int_0^{2\pi} \int_0^{\Theta_m} I(\Theta, \Phi; \lambda_0) \sin \Theta d\Theta d\Phi. \quad (3-17)$$

When the detection angle Θ is larger than the maximum incident angle θ_m , the incident field is not present. For example, in backward scattering measurement,

where the maximum collecting aperture angle is also Θ_m , the detected power is given by,

$$P(\lambda_0) \propto R^2 \int_0^{2\pi} d\Phi \int_{\pi-\Theta_m}^{\pi} \sin \Theta d\Theta \left| \int_0^{2\pi} \int_0^{\Theta_m} \mathbf{E}_s(\Theta, \Phi; \theta, \phi) k^2 \sin \theta \cos \theta d\theta d\phi \right|^2. \quad (3-18)$$

When the spherical scatterer is centered at \mathbf{r}_0 , rather than at the origin, the phase term $e^{j\mathbf{k}_i \cdot \mathbf{r}_0}$ for each Fourier component $\tilde{\mathbf{E}}(\mathbf{k}_i)$ should be considered for the scattered field and the incident field in the far field region. In this case, Eq. (3-14) and Eq. (3-15) become, respectively,

$$\mathbf{E}_s(\Theta, \Phi) = \int_0^{2\pi} \int_0^{\Theta_m} \mathbf{E}_s(\Theta, \Phi; \theta, \phi) e^{j\mathbf{k}_i(\theta, \phi) \cdot \mathbf{r}_0} k^2 \sin \theta \cos \theta d\theta d\phi, \quad (3-19)$$

and

$$\mathbf{E}_I(\Theta, \Phi) = -j\tilde{\mathbf{E}}(\Theta, \Phi) \frac{(2\pi)^2}{\lambda} \cos \Theta \frac{e^{jkR}}{R} e^{j\mathbf{k}_i(\Theta, \Phi) \cdot \mathbf{r}_0}. \quad (3-20)$$

Since the power of linear scattered field depends on the incident power of each wavelength, as described in Chapter 2, we introduce a dimensionless scattering efficiency, q , which is defined as the ratio of the detected scattering power to the total power, when there is no scatterer,

$$q = \frac{\iint_{\Omega_d} I(\Theta, \Phi) \sin \Theta d\Theta d\Omega}{\iint_{\Omega_d} I_0(\Theta, \Phi) \sin \Theta d\Theta d\Omega}, \quad (3-21)$$

where Ω_d is the measurement solid angle. Scattering efficiency, q , in the forward direction is easy to be measured in the experiment. However, when detection direction is not within the incident angle, for example in the backward direction, the scattering field cannot be normalized to the field, which is zero when there is no scatterer. Furthermore, the scattering efficiency, q , depends on the detection angle. Here we introduce the intensity angular distribution function of scattered field for each wavelength $F(\Theta, \Phi; \lambda_0)$ that is the intensity in every direction normalized to the far field intensity of incident wave in the forward direction [8],

$$F(\Theta, \Phi; \lambda_0) = \frac{I(\Theta, \Phi)}{I_0(0,0)} = \frac{|E_s(\Theta, \Phi) + E_t(\Theta, \Phi)|^2}{|E_t(0,0)|^2}. \quad (3-22)$$

Therefore the scattering efficiency q can be expressed in the form of intensity angular distribution function as

$$q = \frac{\iint_{\Omega_d} F(\Theta, \Phi) \sin \Theta d\Theta d\Omega}{\iint_{\Omega_d} F_0(\Theta, \Phi) \sin \Theta d\Theta d\Omega}, \quad (3-23)$$

where $F_0(\Theta, \Phi; \lambda)$ is the intensity angular distribution function of the initial incident field. For Eq. (3-4), we can easily get $F_0(\Theta, \Phi; \lambda)$ as

$$F_0(\Theta, \Phi; \lambda) = \begin{cases} \cos \Theta & \Theta \leq \theta_m \\ 0 & \Theta > \theta_m \end{cases}. \quad (3-24)$$

From Eq. (3-10) to (3-24), we can calculate any single wavelength scattered field produced by a uniform spherical scatterer in the tightly focused field. When trying to calculate the scattering spectrum in the supercontinuum tweezer in practice, aberration should also be incorporated in the theoretical model. Chromatic aberrations due to the focal length differences for different wavelengths require a change of coordinate origins, which can be written as

$$f(\lambda) = f(\lambda_0) + \Delta f, \quad \mathbf{r}_0(\lambda) = \mathbf{r}_0(\lambda_0) - \Delta f \hat{\mathbf{z}}. \quad (3-25)$$

Δf is the chromatic aberration of the system which can be calibrated experimentally. We use Eq. (3-25) together with Eq. (3-10)-(3-24) to analyze the optical scattering spectrum of a uniform spherical scatterer in a supercontinuum trap. Another aberration produced by a tightly focused beam occurs due to refraction at the interface of cover glass and solution, and it can be calculated using Fresnel's equations.

3.3 Experiment Verification

To verify the theoretical analysis, we have also investigated scattering of tightly focused supercontinuum experimentally. Since the scattering spectrum depends on the position of the scatterer, in order to quantitatively compare theory and experiment we immobilized microspheres (Duke Scientific, 4000 series, $n = 1.59$ @ 589 nm) on the bottom of the sample cell (made from standard glass coverslip) so that we can precisely control and determine the position of microspheres. Immobilization was

achieved by air-drying microsphere solution in a sample cell for a few days. The sample cell was then filled with immersion oil whose refractive index ($n_D = 1.5150$) matches that of the sample cell ($n_D = 1.523$). As a result, the microsphere is surrounded by a uniform medium with slightly different refractive index. The experimental setup is shown in Fig. 3.2. White light supercontinuum, which was generated by coupling sub-nanosecond laser pulses (JDS Uniphase NP-10620-100) into a nonlinear photonic crystal fiber (BlazePhotonics SC-5.0-1040), was collimated and then tightly focused onto a single microsphere by an apochromatic objective lens L1 (100x /1.4 N.A.). The full aperture of the objective lens was uniformly illuminated. Another objective lens L2 (10x /0.25 N.A.) was used to collect the forward scattered light. In addition, an iris was used to further limit the effective numerical aperture of the collection system (effective N.A.~ 0.08). Finally, the spectrum of the forward-scattered light was measured by an optical spectrum analyzer. A CCD camera was used to monitor the position of the microsphere.

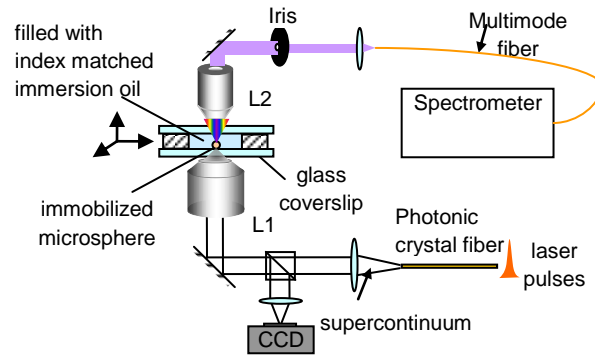
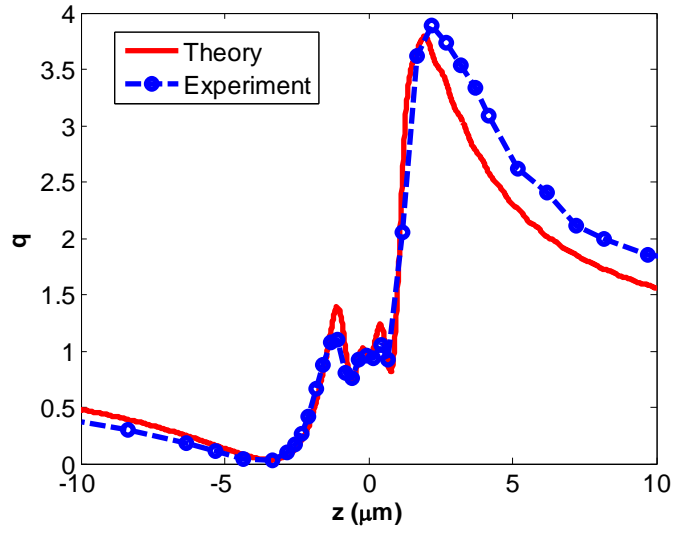
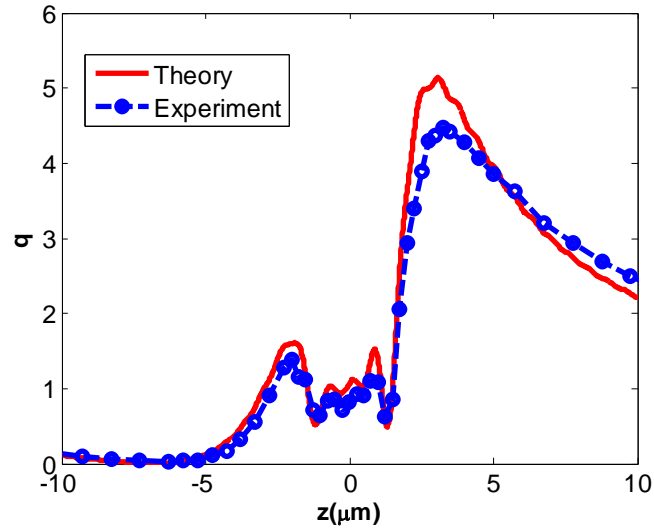


Figure 3.2 Schematic diagram of experiment setup to verify the modeling of focus beam scattering by a spherical particle.

We normalized the forward scattering spectrum to the reference spectrum which was measured when no microsphere was present. This ratio is defined as scattering efficiency (denoted by q in Fig. 3.3 and Fig. 3.5). By mechanically translating the sample cell, normalized scattering spectra (i.e., scattering efficiency) at different positions can be obtained. The results are plotted in Fig. 3.3. Fig. 3.3(a) and (b) show the scattering efficiencies of two microspheres (diameter 1.5 μm and 2 μm respectively) at $\lambda_0 = 600 \text{ nm}$ as a function of their axial position. The blue dots correspond to experimental data while the red lines represent calculation results. Intuitively, since the refractive index of the microsphere is larger than that of the surrounding medium it works like a positive lens approximately. A strong peak can be observed in the scattering efficiency curve if the sphere is moved away from the lens and collimates the incident beam. On the other hand, a minimum occurs if the sphere is moved closer to the lens and focuses/defocuses the incident beam more strongly. Finally, when the sphere is very far away from the focal region the scattering effect is weakened and the scattering efficiency approaches to unity as expected. Compared with that of the 1.5 μm diameter microsphere, the maximum scattering efficiency of the 2 μm diameter microsphere is slightly higher and the positions of its maximum and minimum are further away from the focal point.



(a)



(b)

Figure 3.3 Dependence of scattering efficiency on axial position (a) and (b) are the scattering efficiencies of the 1.5 and 2 μm diameter microspheres respectively at $\lambda_0 = 600\text{ nm}$ as a function of axial position. Red lines are theoretical calculation results. Blue dots are experiment results.

Due to chromatic aberration, different wavelengths focus at different axial positions.

As a result, the z -dependence scattering efficiency curve for different wavelengths

will center at different positions (their actual focal points). We correlated the experimentally measured scattering efficiency z-dependence curves with the corresponding theoretical curves (assuming no chromatic aberration) for each wavelength. The positions of correlation peaks indicate chromatic aberration for different wavelengths. We used both the 1.5- and 2.0- μm -diameter microspheres to calibrate the chromatic aberration of the whole system. The result $\Delta f = f(\lambda) - f(\lambda_0 = 600\text{nm})$ is shown in Fig.3.4.

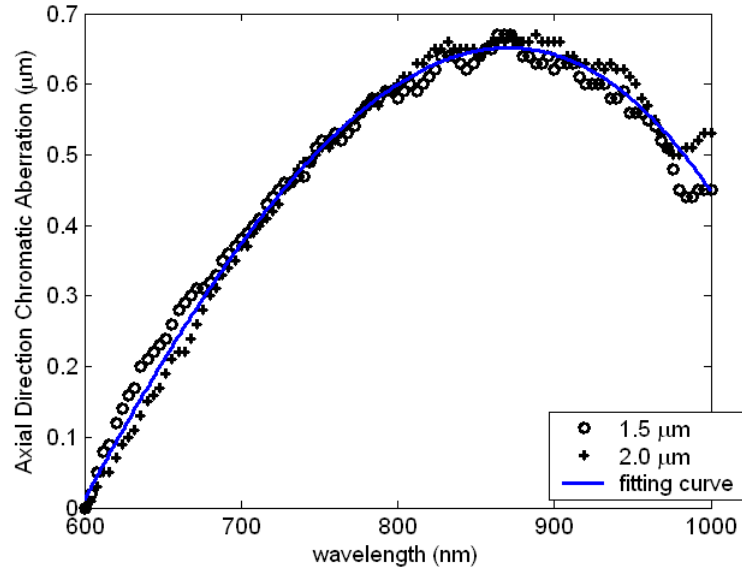
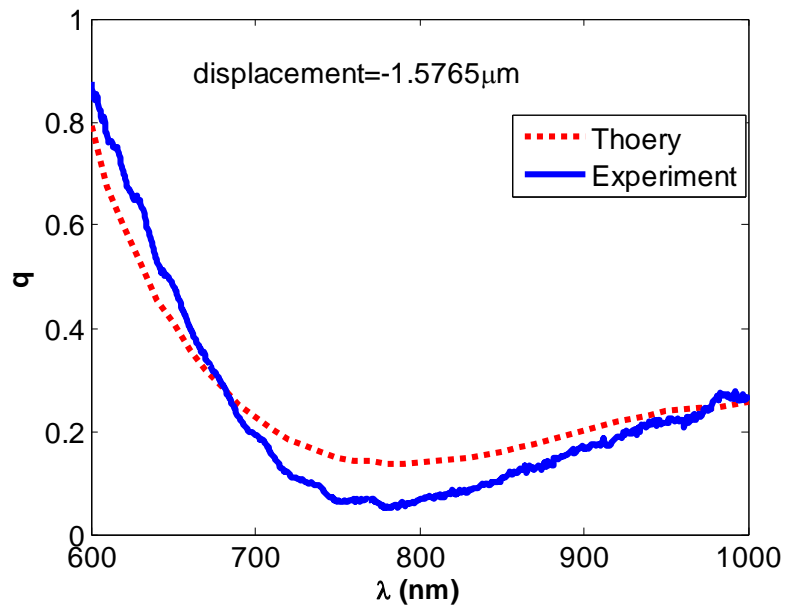


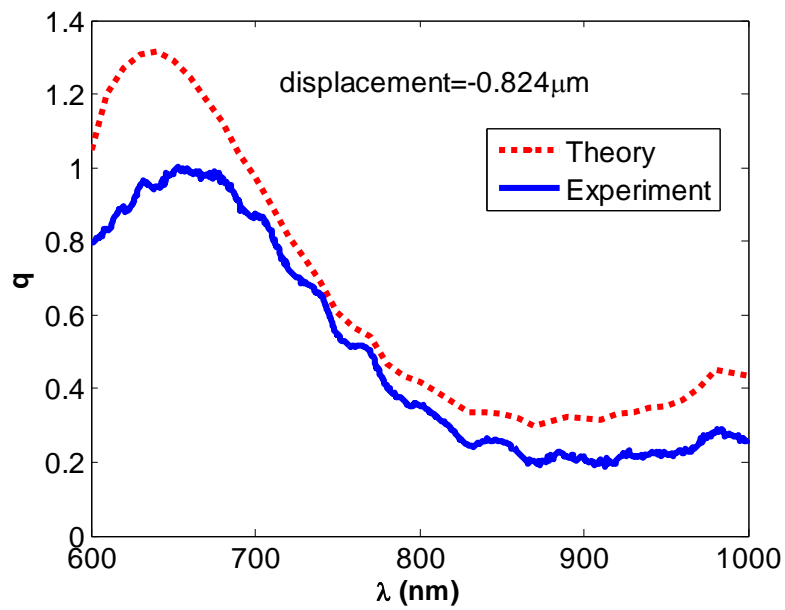
Figure 3.4 Measured chromatic aberration of the experimental system. Circles and pluses represent the results using 1.5 and 2.0- μm -diameter microspheres respectively. The blue line is the fitted curve.

Fig. 3.5 shows the measured and calculated scattering efficiencies of the 1.5 μm diameter microsphere as a function of wavelength at two different axial positions. Chromatic aberration was included in the calculation. The theory (dotted red line) in

general agrees with the experimental results (solid blue line). However, there exists quite considerable discrepancy between the theory and experiment when the focused spot is moved near the interface of microsphere/coverlip. Several factors may have contributed to it: (1) although the refractive index of the immersion oil (1.515) is very close to that of the glass coverslip (1.523), they are not identical. As a matter of fact, the difference is about 10% of the refractive index difference between the microsphere (1.59) and the immersion oil. Boundary effects (e.g., multiple reflections and scatterings between the coverslip and the microsphere) may not be ignored; (2) dispersion of the microsphere, glass, and immersion oil was not considered in the theoretical calculation; (3) possible lateral displacement of the microsphere from the center of the beam; (4) noise in the supercontinuum. Since the polymer sphere is quite inert in the measurement wavelength range, the measured scattering spectrum does not show any pronounced features. We should point out that the method outlined here can also be used to model optical scattering of other types of particles including metallic particles. Since the scattering spectrum depends on particle size, shape, refractive index, and resonant absorption (if exists), optical spectroscopy with focused supercontinuum is a promising technique to non-invasively probe the properties of individual particles.



(a)



(b)

Figure 3.5 Scattering spectra of a 1.5 μ m diameter microsphere at two different positions. Dotted red lines are theoretical calculation results while solid blue lines are experiment data.

3.4 Further discussion about scattering model based Mie's Theory

In the forward ($\Theta = 0$) and backward ($\Theta = \pi$) directions, due to the axial symmetry of incident beam, the formalisms can be further simplified when scatterer sphere is also on the axis. For $\Theta = 0$ (forward direction), it can be shown that the scattered field produced by one plane wave component of the incident field is given by

$$\mathbf{E}_s(0,0;\theta,\phi) = \frac{je^{jkr}}{kr} \frac{-j\lambda}{(2\pi)^2} \frac{1}{\cos\theta} fe^{jkf} \left[\begin{pmatrix} \sin^2 \phi \\ -\sin \phi \cos \phi \\ 0 \end{pmatrix} S_1(\theta) + \begin{pmatrix} \cos^2 \phi \\ \sin \phi \cos \phi \\ 0 \end{pmatrix} S_2(\theta) \right] E_0 \sqrt{\cos\theta} e^{jk \cdot \mathbf{r}_0} \quad (3-26).$$

If $\mathbf{r}_0 = z_0 \hat{\mathbf{z}}$ (i.e., the sphere is displaced only along the z axis), the total scattered field can be calculated as follows.

$$\begin{aligned} & \mathbf{E}_s(0,0) \\ &= \int_0^{2\pi} \int_0^{\theta_m} \mathbf{E}_s(0,0;\theta,\phi) k^2 \sin\theta \cos\theta d\theta d\phi \\ &= \frac{1}{2\pi} \frac{f}{R} e^{jk(f+R)} E_0 \int_0^{2\pi} \int_0^{\theta_m} \left[\begin{pmatrix} \sin^2 \phi \\ -\cos\phi \sin\phi \\ 0 \end{pmatrix} S_1(\theta) + \begin{pmatrix} \cos^2 \phi \\ \cos\phi \sin\phi \\ 0 \end{pmatrix} S_2(\theta) \right] e^{jkz_0 \cos\theta} \sin\theta \sqrt{\cos\theta} d\theta d\phi \\ &= \hat{\mathbf{x}} \frac{1}{2} \frac{f}{R} e^{jk(f+R)} E_0 \int_{\cos\theta_m}^1 e^{jkz_0 \cos\theta} \sqrt{\cos\theta} [S_1(\theta) + S_2(\theta)] d\cos\theta \\ &= \hat{\mathbf{x}} \frac{1}{2} \frac{f}{R} e^{jk(f+R)} E_0 \sum_n \frac{2n+1}{n(n+1)} (a_n + b_n) \int_{\cos\theta_m}^1 e^{jkz_0 \cos\theta} \sqrt{\cos\theta} [\pi_n(\cos\theta) + \tau_n(\cos\theta)] d\cos\theta \end{aligned} \quad (3-27).$$

The incident field in the far field region is given by

$$\mathbf{E}_I(0,0) = -\frac{f}{R} e^{jk(f+R)} e^{jkz_0} E_0 \hat{\mathbf{x}}. \quad (3-28)$$

We can obtain the normalized angular intensity function in the forward direction and,

$F(0,0)$, as

$$F(0,0) = \left[\sum_n \frac{2n+1}{n(n+1)} (a_n + b_n) \int_{\cos \theta_m}^1 e^{jkz_0 \cos \theta} \sqrt{\cos \theta} [\pi_n(\cos \theta) + \tau_n(\cos \theta)] d \cos \theta \right] \left[\frac{e^{-jkz_0}}{2} - 1 \right]^2. \quad (3-29)$$

Similarly, in the backward direction ($\theta = \pi$) the scattered field produced by one plane wave component can be written as

$$\mathbf{E}_s(\pi, 0; \theta, \phi) = \frac{e^{jkR}}{kR} \frac{\lambda}{(2\pi)^2} \frac{1}{\cos \theta} f e^{jkf} \times \left[\begin{pmatrix} \sin^2 \phi \\ -\sin \phi \cos \phi \\ 0 \end{pmatrix} S_1(\pi - \theta) - \begin{pmatrix} \cos^2 \phi \\ \sin \phi \cos \phi \\ 0 \end{pmatrix} S_2(\pi - \theta) \right] E_0 \sqrt{\cos \theta} e^{j\mathbf{k} \cdot \mathbf{r}_0}. \quad (3-30)$$

The total backward scattered field at distance $\mathbf{r}_0 = z_0 \hat{\mathbf{z}}$ is

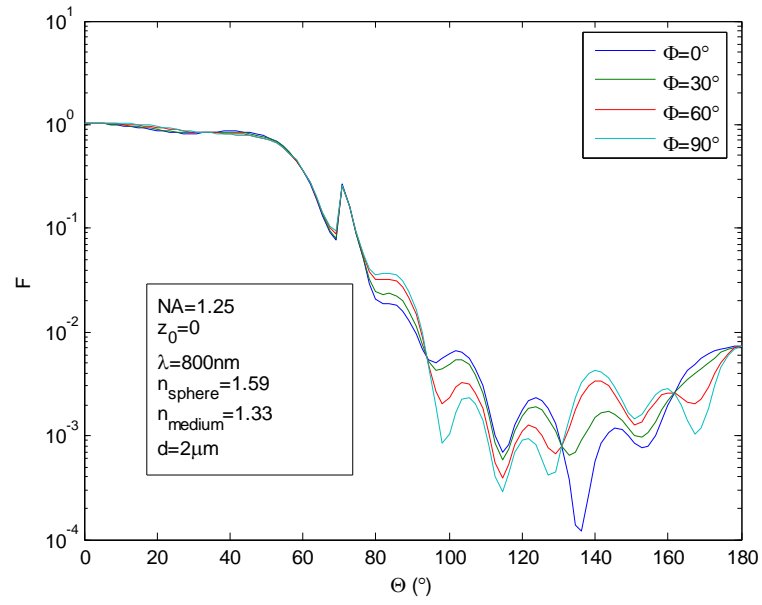
$$\mathbf{E}_s(\pi, 0) = \hat{\mathbf{x}} \frac{1}{2} \frac{f}{R} e^{jk(f+R)} E_0 \times \sum_n \frac{2n+1}{n(n+1)} (a_n - b_n) \int_{\cos \theta_m}^1 e^{jkz_0 \cos \theta} \sqrt{\cos \theta} [\pi_n(\cos(\pi - \theta)) - \tau_n(\cos(\pi - \theta))] d \cos \theta \quad (3-31)$$

Similarly, we also obtain the normalized angular intensity function in the backward direction, $F(\pi, 0)$ as

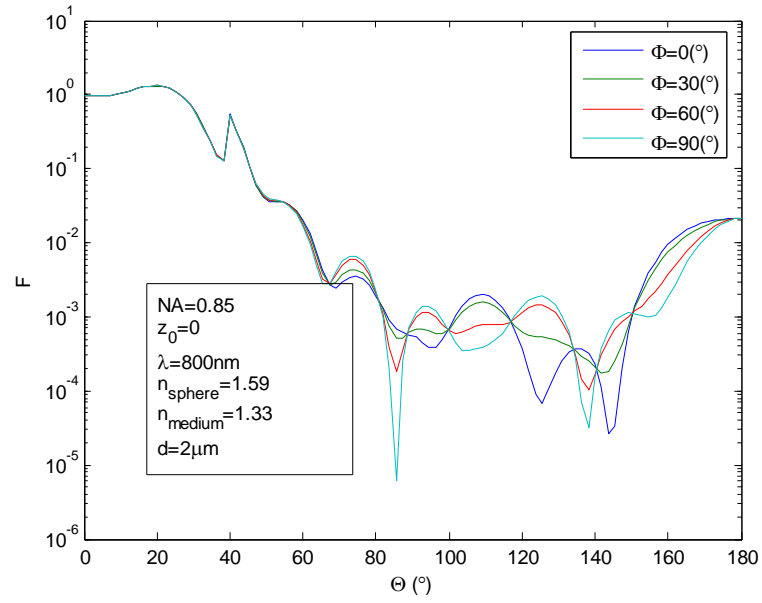
$$F(\pi, 0) = \left[\sum_n \frac{2n+1}{n(n+1)} (a_n - b_n) \int_{\cos \theta_m}^1 e^{jkz_0 \cos \theta} \sqrt{\cos \theta} [\pi_n(\cos(\pi - \theta)) - \tau_n(\cos(\pi - \theta))] d \cos \theta \right] / 2 \Bigg|^2$$

(3-32).

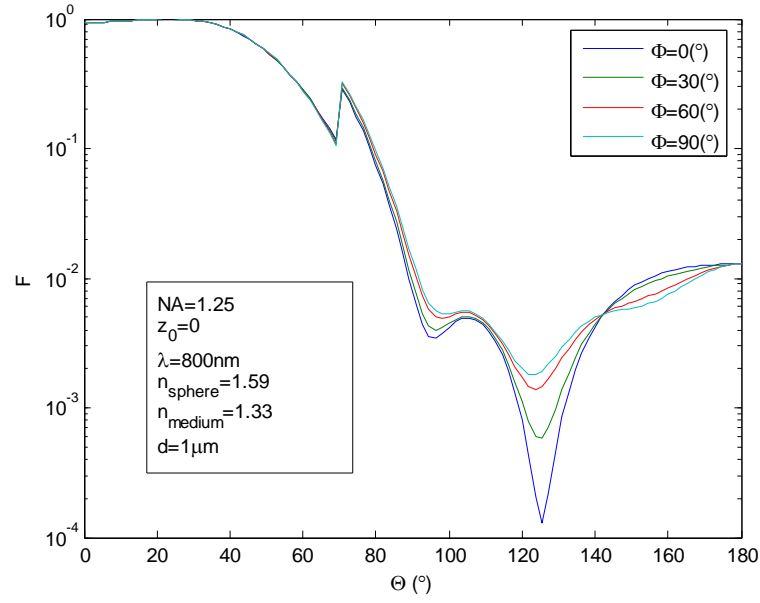
All the calculation codes are programmed in Matlab 7.0.4. First, we calculate the single wavelength intensity angular distribution of different sized spherical scatterers located at focal point of high numerical aperture objective lens. Fig. 3.6 (a)-(d) show the normalized intensity of 800 nm wavelength optical wave scattered by uniform polystyrene spheres with refractive index 1.59 in the water solution(refractive index is 1.33). Different colored curves are the results of observation azimuthal angles at 0 °, 30 °, 60 ° and 90 °, respectively. Fig. 3.6 (a) plots the results of 2-micron-diameter sphere trapped by using a 1.25 numerical aperture objective lens; Fig. 3.6 (b) plots the results of 2 micron diameter sphere trapped by using a 0.85 numerical aperture objective lens; Fig. 3.6 (c) is the result of 1 micron diameter sphere trapped by using a 1.25 numerical aperture objective lens; and Fig. 3.6 (d) is the result of 1-micron-diameter sphere trapped by using a 0.85 numerical aperture objective lens. The scattered field angular distributions change significantly for different sizes and numerical apertures of objective lens.



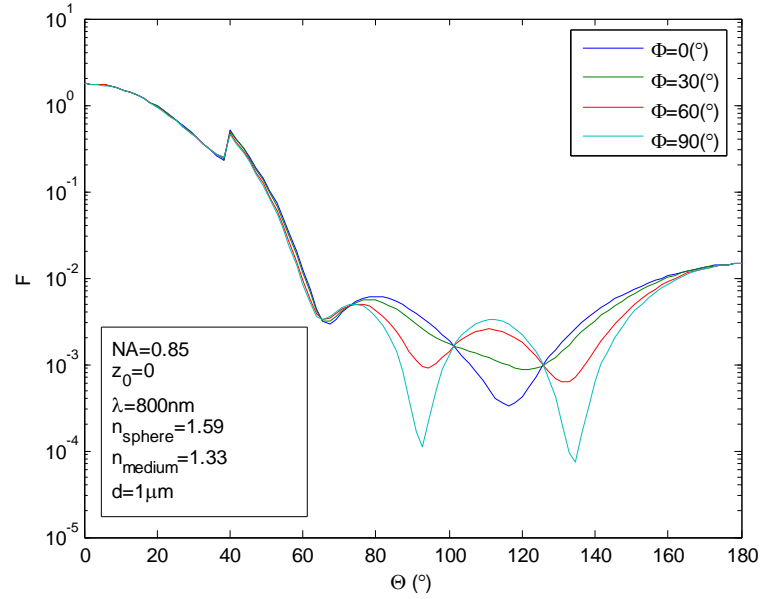
(a)



(b)



(c)



(d)

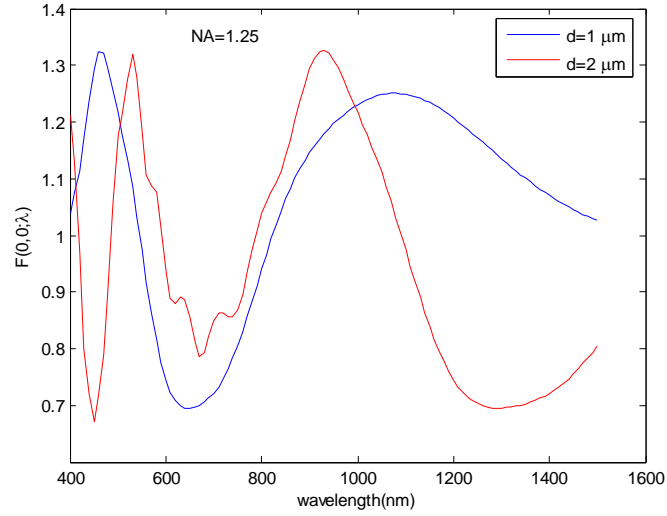
Figure 3.6 Normalized intensity angular distributions of focused beams scattered by spherical particles by a 800 nm source. The refractive indices of spherical scatterer and surrounding media are taken to be 1.59 and 1.33, respectively, and different color curves represent azimuthal angles at 0°, 30°, 60° and 90°, respectively. (a) 2 micron diameter sphere, $NA = 1.25$; (b) 2 micron diameter sphere, $NA = 0.85$; (c) 1 micron diameter sphere, $NA=1.25$; (d) 1 micron diameter

sphere, NA=0.85.

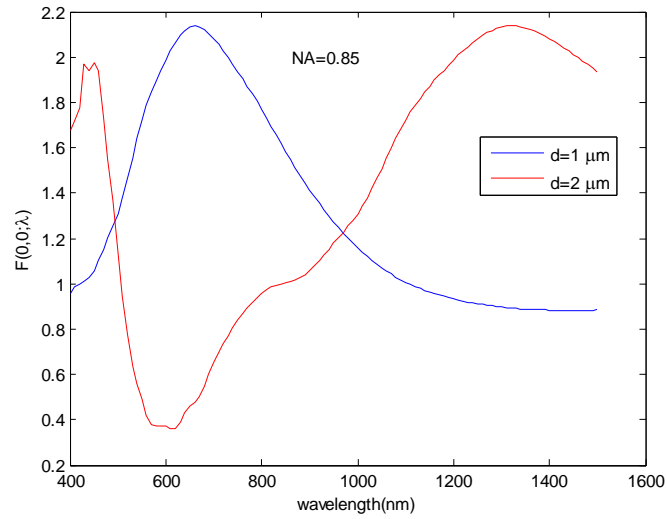
Figure 3.7 shows the calculated normalized scattering spectra in the forward direction using Eq. (3-29). The scatterers and surrounding media are still selected as polystyrene spheres and water, respectively, and the wavelength dependence of the refractive indices and absorption are ignored. The scattering spectra from 400 nm to 1500 nm in forward direction using 1.25 numerical aperture and 0.85 numerical apertures are, respectively, plot in Fig. 3.7 (a) and (b). Blue curves are the results of 1 micron diameter and red curves are of 2 micron diameter. Similarly, we use Eq. (3-32) to obtain the normalized scattering spectra in the backward direction, and calculations are plotted in Fig. 3.8 (a) and (b). The spectra structure features show obvious dependence on the size of the scatterer. For example, in the spectra of Fig. 3.7 (a), a dip appears at around 650 nm for 1 micron diameter sphere, while for the 2 micron diameter sphere the corresponding dip shifts to about 1300 nm. This analysis is consistent with Mie's theory's results.

When the center of spherical scatterer is not located at the focal point, the scattering spectra change due to phase factor. Figure 3.9 shows the calculated the scattering spectra when 1 micron diameter spherical particle is centered at different position along the z axis. Fig. 3.9 (a) displays the results for an objective lens (NA = 1.25) and Fig. 3.9 (b) displays the results of another (NA = 0.85). Since the refractive index of scatterer sphere is higher than that of surrounding media, water, the scatterer behaves like a positive lens. When scatterer is centered behind the focal point, the

light is collimated into the forward direction. Therefore, the scattered intensity is higher than when the particle is located on other positions.

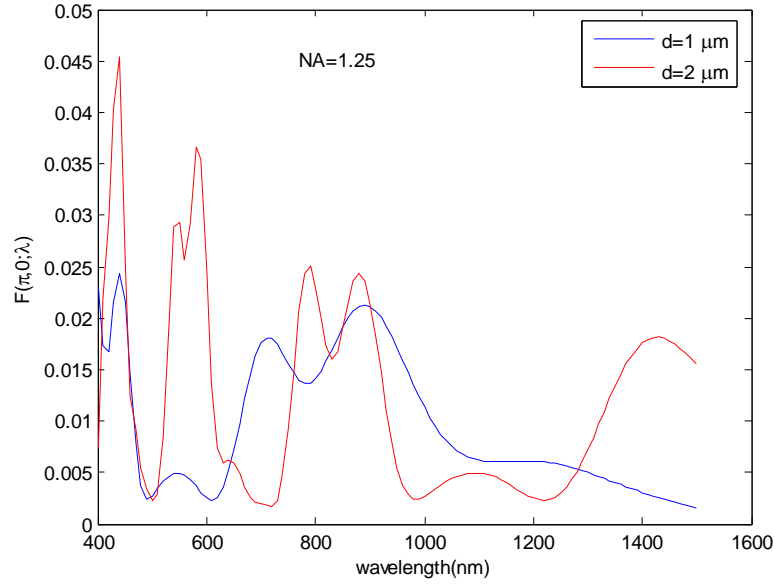


(a)

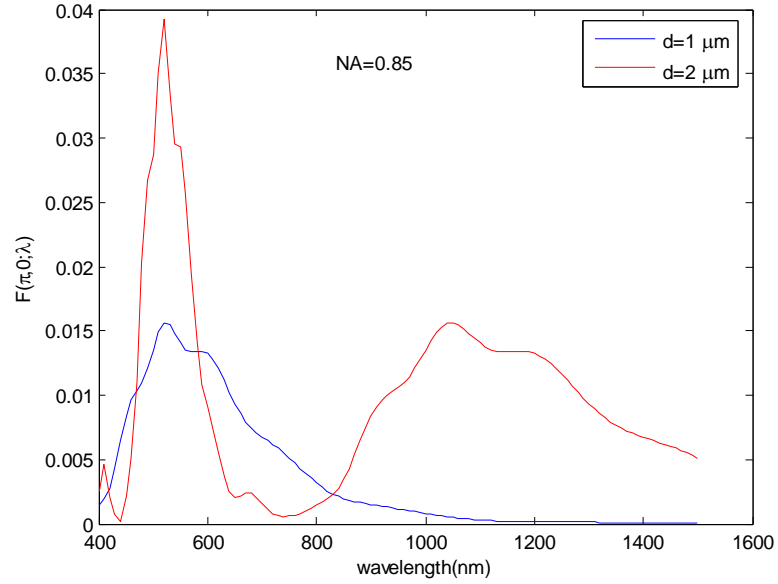


(b)

Figure 3.7 Normalized scattering spectrum in the forward direction. The refractive indices of spherical scatterer and surrounding media are assumed to be 1.59 and 1.33, respectively. (a) NA = 1.25; (b) NA = 0.85. Blue curves are the results of 1-micron-diameter sphere, and red curves are of 2 micron diameter sphere.



(a)



(b)

Figure 3.8 Normalized scattering spectrum in the backward direction. The refractive indices of spherical scatterer and surrounding media are assumed to be 1.59 and 1.33, respectively. (a) NA = 1.25; (b) NA = 0.85. Blue curves are the results of 1 micron diameter sphere, and red curves are of 2 micron diameter sphere.

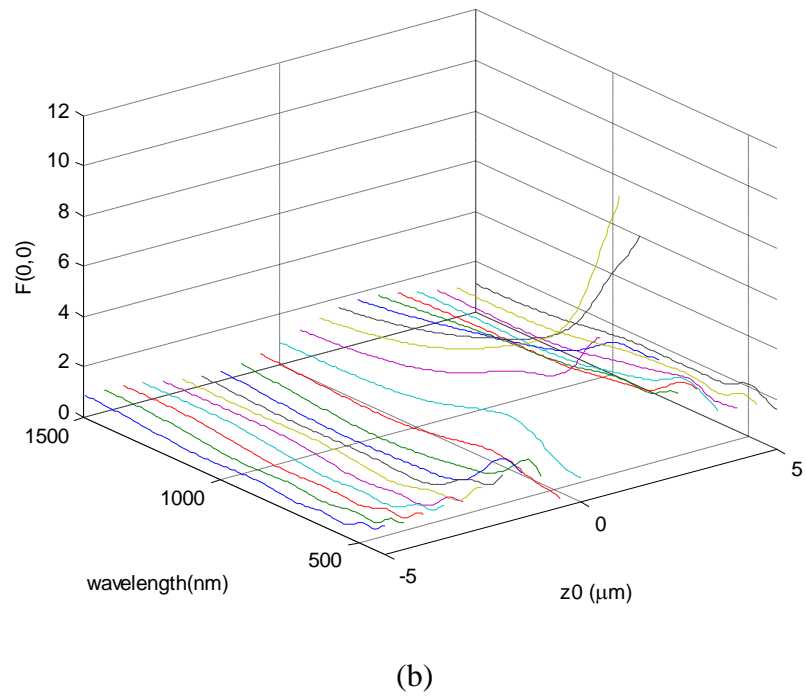
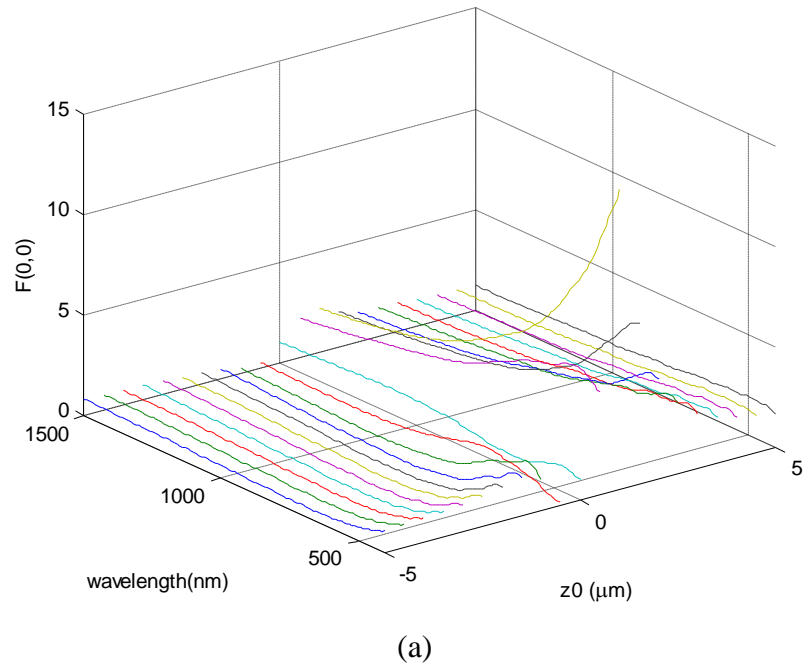


Figure 3.9 Normalized scattering spectrum in the forward direction at different axial positions

In the calculation above, the scatterer is assumed to be inert, i.e., there are no resonance features in the refractive index, and the effects of dispersion and absorption are ignored. The formulas derived above do not rely on the refractive index properties; thus they can also be used to model optical scattering by other types of uniform spherical particles including metallic particles. Figure 3.10 shows the calculated forward direction scattering spectra of gold spheres of different sizes in water using Eq. (3-29). A numerical aperture of 1.25 for the focusing objective lens was used in the calculation. The nanoparticle is assumed to be suspended in the water, and the refractive index data of gold are obtained from Palik [104]. We assume that the refractive index of the gold nanoparticle is the same as that of bulk material. As shown in Figure 3.10, there are characteristic dips in the forward scattering spectrum, which are caused by localized surface plasmon resonance (LSPR) [58, 105]. This is because the scattering at LSPR frequency is stronger than non-resonance frequency, and less energy will be less received. These positions of the dips shift as the size of the nanoparticles changes.

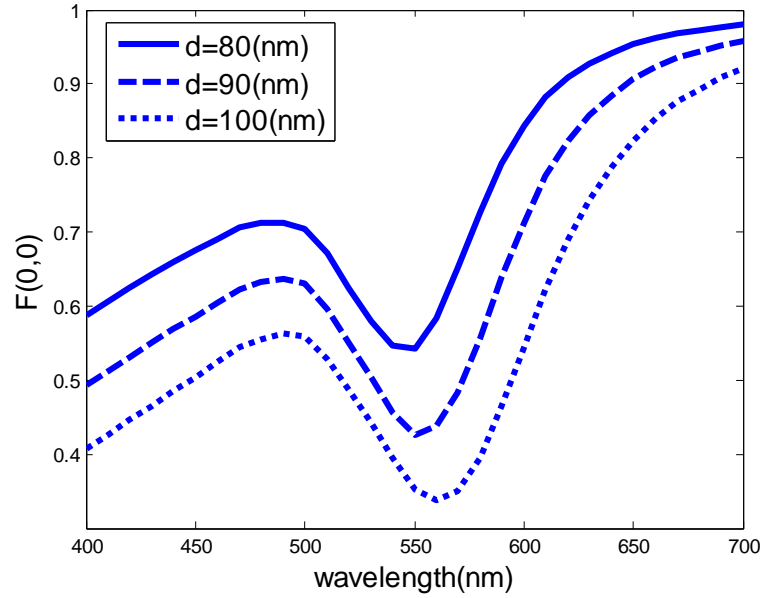


Figure 3.10 Normalized scattering spectrum of gold nanoparticles of various sizes in the water solution. NA = 1.25. Solid, dashed and dotted lines are the results of 80 nm, 90 nm and 100 nm gold particles, respectively.

3.5 Modeling Non-spherical-shaped Weak Scatterers Based On Born Approximation

The discussions and calculations above are based on Mie's scattering theory, for which the scatterer is assumed as a sphere. In the more general case, when scatterer is of non-spherical shape, other than sphere, there is no general analytical formula to calculate the scattered field. But when the scattered field is weak and able to be treated as a perturbation, for example, under the condition that the refractive index of the scatterer is very close to that of the surrounding medium (i.e., $m \approx 1$) or the size of the scatterer is much smaller than the wavelength, Born approximation [101, 106, 107] can be applied to obtain the scattered field.

The derivation starts with Maxwell's equations in charge-free space, and also time-dependency $e^{-j\omega t}$ is assumed throughout. The incident field propagating in the uniform medium without scatterer satisfies the wave equation

$$\nabla \times \nabla \times \mathbf{E}_i - \omega^2 \mu \varepsilon \mathbf{E}_i = 0, \quad (3-33)$$

where $\varepsilon = \varepsilon_r \varepsilon_0 = n^2 \varepsilon_0$ is the permittivity of the medium. With the presence of a weak scatterer, the total field $\mathbf{E} = \mathbf{E}_i + \mathbf{E}_s$, where \mathbf{E}_s is the scattered field, satisfies wave equation

$$\nabla \times \nabla \times (\mathbf{E}_i + \mathbf{E}_s) - \omega^2 \mu (\varepsilon + \Delta \varepsilon) (\mathbf{E}_i + \mathbf{E}_s) = 0. \quad (3-34)$$

where

$$\Delta \varepsilon = \begin{cases} (m^2 - 1)n^2 \varepsilon_0 & \text{inside the scatterer} \\ 0 & \text{else} \end{cases} \quad (3-35)$$

is the permittivity difference between scatterer and medium. Subtracting Eq. (3-33) from Eq. (3-34), we have

$$\nabla \times \nabla \times \mathbf{E}_s - \omega^2 \mu \varepsilon \mathbf{E}_s = \omega^2 \mu \Delta \varepsilon (\mathbf{E}_i + \mathbf{E}_s) \quad (3-35).$$

For weak scatterer, $\mathbf{E}_s \ll \mathbf{E}_i$, we can solve the scattering field by using Born approximation method, in which \mathbf{E}_s term in the right side of Eq. (3-35) is ignored. The incident field takes place of total field as the driving field, thus the wave equation for scattering wave changes to

$$\nabla \times \nabla \times \mathbf{E}_s - \omega^2 \mu \varepsilon \mathbf{E}_s = \omega^2 \mu \Delta \varepsilon \mathbf{E}_i. \quad (3-36)$$

Eq. (3-36) can be solved by using method of Green's function. The solution can be written in the form of

$$\mathbf{E}_s(\mathbf{R}) = \omega^2 \mu \iiint_{\mathbf{r}'} \overline{\overline{\mathbf{G}}}(\mathbf{R}; \mathbf{r}) \Delta \varepsilon \mathbf{E}_i d\mathbf{r}' \quad (3-37)$$

where $\mathbf{R}(R \sin \Theta \cos \Phi, R \sin \Theta \sin \Phi, \cos \Theta)$ is the position where the signal is detected, and $\mathbf{r}'(r' \sin \theta' \cos \phi', r' \sin \theta' \sin \phi', \cos \theta')$ is the spatial volume the of the scatterer. $\overline{\overline{\mathbf{G}}}$ is the Green's function of equation

$$\nabla \times \nabla \times \overline{\overline{\mathbf{G}}} - k^2 \overline{\overline{\mathbf{G}}} = \mathbf{n} \delta(\mathbf{r} - \mathbf{r}'), \quad (3-38)$$

where \mathbf{n} is the unit vector of driving field. The analytical solution of $\overline{\overline{\mathbf{G}}}$ is given as[108]

$$\overline{\overline{\mathbf{G}}} = (\overline{\overline{\mathbf{I}}} + \frac{\nabla \nabla}{k^2}) G_0, \quad (3-39)$$

where $\overline{\overline{\mathbf{I}}}$ is a 3×3 unit matrix, $G_0(\mathbf{R}, \mathbf{r}') = \exp(jk|\mathbf{R} - \mathbf{r}'|)/(4\pi|\mathbf{R} - \mathbf{r}'|)$ is the scalar Green's function. For far-field radiation $R \gg r'$, $|\mathbf{R} - \mathbf{r}'|$ in the phase term can be approximated as $|\mathbf{R}| - \mathbf{R} \cdot \mathbf{r}'/|\mathbf{R}|$. The scattering field can be reformatted into spherical coordinate components

$$\begin{aligned}
\mathbf{E}_s(\mathbf{R}) &= \omega^2 \mu \frac{\exp(jk|\mathbf{R}|)}{|\mathbf{R}|} \iiint_{\mathbf{r}'} \left(\bar{\mathbf{I}} + \frac{\nabla \nabla}{k^2} \right) \exp(-jk \frac{\mathbf{R} \cdot \mathbf{r}'}{|\mathbf{R}|}) \Delta \varepsilon \mathbf{E}_i d\mathbf{r}' \\
&= \omega^2 \mu \Delta \varepsilon \frac{\exp(jkR)}{R} \iiint_{\mathbf{r}'} d\mathbf{r}' \exp(-j\mathbf{k}_d \cdot \mathbf{r}') \begin{bmatrix} 0 & 0 & 0 \\ \cos \Theta \cos \Phi & \cos \Theta \sin \Phi & -\sin \Theta \\ -\sin \Phi & \cos \Phi & 0 \end{bmatrix} \begin{bmatrix} \mathbf{E}_{ix} \\ \mathbf{E}_{iy} \\ \mathbf{E}_{iz} \end{bmatrix} \begin{bmatrix} \hat{R} \\ \hat{\Theta} \\ \hat{\Phi} \end{bmatrix} .
\end{aligned}
\tag{3-40}$$

where \hat{R} , $\hat{\Theta}$, and $\hat{\Phi}$ are the unit vector in the spherical coordinate.

Since the scatterer is in the vicinity of the focal point, the electric field of incident wave at point \mathbf{r}' can be still described as Eq. (3-1). When Eq. (3-6) is substituted in Eq. (3-1), the incident field can be written as

$$\mathbf{E}(\mathbf{r}') = \int_0^{2\pi} \int_0^{\theta_m} -\frac{j}{2\pi} f e^{jkf} E_0 \sqrt{\cos \theta} e^{j\mathbf{k}_i \cdot \mathbf{r}'} k \sin \theta \begin{bmatrix} \cos \theta \cos^2 \phi + \sin^2 \phi \\ (\cos \theta - 1) \cos \phi \sin \phi \\ -\sin \theta \cos \phi \end{bmatrix} d\theta d\phi .$$

(3-41).

As derived by Richard and Wolf in ref. [109], the integration with respect to ϕ can be carried out with Bessel function of first kind. The electric field at a point \mathbf{r}' is expressed as

$$\mathbf{E}(\mathbf{r}') = -\frac{f k e^{jkf} E_0}{2} \begin{bmatrix} j(I_0 + I_2 \cos 2\phi') \\ jI_2 \sin 2\phi' \\ 2I_1 \cos \phi' \end{bmatrix} \tag{3-42}$$

where

$$\begin{aligned}
I_0 &= \int_0^{\theta_m} \cos^{\frac{1}{2}} \theta \sin \theta (1 + \cos \theta) J_0(kr' \sin \theta \sin \theta') e^{jkr' \cos \theta \cos \theta'} d\theta \\
I_1 &= \int_0^{\theta_m} \cos^{\frac{1}{2}} \theta \sin^2 \theta J_1(kr' \sin \theta \sin \theta') e^{jkr' \cos \theta \cos \theta'} d\theta \\
I_2 &= \int_0^{\theta_m} \cos^{\frac{1}{2}} \theta \sin \theta (1 - \cos \theta) J_2(kr' \sin \theta \sin \theta') e^{jkr' \cos \theta \cos \theta'} d\theta
\end{aligned} \tag{3-43}$$

Substituting Eq. (3-42) and (3-43) into Eq. (3-40), we get the three spherical coordinate components of scattered field in the form of

$$\begin{aligned}
\mathbf{E}_{s\hat{R}}(\mathbf{R}) &= 0 \\
\mathbf{E}_{s\hat{\Theta}}(\mathbf{R}) &= -\omega^2 \mu \Delta \varepsilon \frac{\exp(jkR)}{R} \frac{fke^{jkf} E_0}{2} \times \\
&\quad \iiint_{\mathbf{r}'} d\mathbf{r}' \exp(-j\mathbf{k}_d \cdot \mathbf{r}') [j \cos \Theta \cos \Phi (I_0 + I_2 \cos 2\phi') + j \cos \Theta \sin \Phi I_2 \sin 2\phi' - \sin \Theta 2I_1 \cos \phi'] \\
\mathbf{E}_{s\hat{\Phi}}(\mathbf{R}) &= -\omega^2 \mu \Delta \varepsilon \frac{\exp(jkR)}{R} \frac{fke^{jkf} E_0}{2} \times \\
&\quad \iiint_{\mathbf{r}'} d\mathbf{r}' \exp(-j\mathbf{k}_d \cdot \mathbf{r}') [-j \sin \Phi (I_0 + I_2 \cos 2\phi') + j \cos \Phi I_2 \sin 2\phi']
\end{aligned} \tag{3-44}$$

The integration in the Eq. (3-44) clearly indicates the scatterer-shape-dependence of scattered field.

When the term $\nabla(\nabla \cdot \mathbf{E})$ in the Eq. (3-36) can be ignored, we use a scalar formalism instead of vectorial field ones to describe scattered field. The wave equation of scattered field becomes

$$\nabla^2 E_s + \omega^2 \mu_0 \varepsilon_1 E_s = -\omega^2 \mu_0 \Delta \varepsilon E_i. \tag{3-45}$$

The solution of Eq. (3-45) is given by

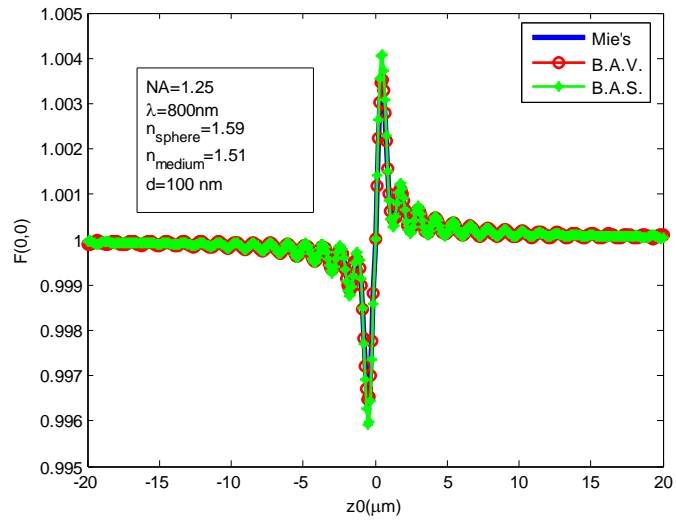
$$\begin{aligned}
E_s &= \iiint -\omega^2 \mu_0 \Delta \varepsilon(\mathbf{r}') E_i \left\{ \frac{1}{4\pi^2} \iint \frac{\exp[j\mathbf{k}_d \cdot (\mathbf{r} - \mathbf{r}')] }{2jk_{dz}} dk_{dx} dk_{dy} \right\} d^3\mathbf{r}' \\
&= -\omega^2 \mu_0 \iint dk_{dx} dk_{dy} \frac{e^{j\mathbf{k}_d \cdot \mathbf{r}}}{4\pi^2} \iiint \frac{\Delta \varepsilon(\mathbf{r}') E_i e^{-j\mathbf{k}_d \cdot \mathbf{r}'} d^3\mathbf{r}'}{2j\sqrt{k^2 - k_{dx}^2 - k_{dy}^2}}
\end{aligned} \tag{3-46}$$

The curled bracket term in Eq. (3-46) is the scalar Green's function G_0 .

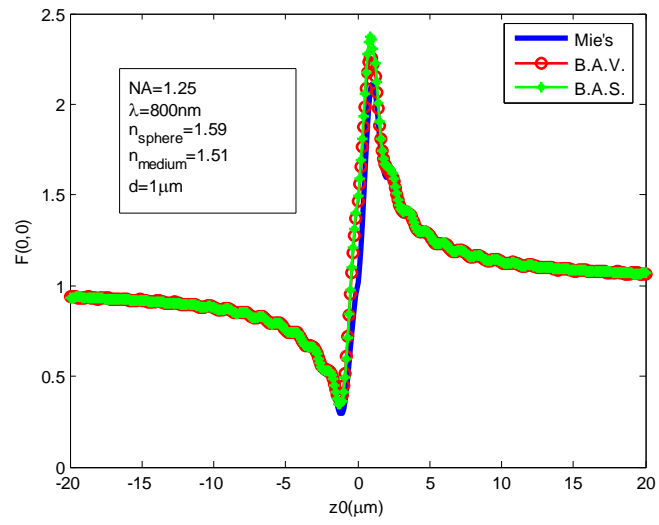
To compare with the results obtained by using Mie's theory, we used Eq. (3-29) to calculate the normalized scattered intensity in the forward direction, $F(0,0)$, produced by a spherical scatterer illuminated by tightly focused beam at different positions along the z axis. The results are in Fig. 3.11(a)-(d) as solid blue curves. The results calculated by Born approximation method using vectorial formulas, Eq. (3-44), and scalar formulas, Eq. (3-46), are also plot in the same figures as red curves with circles and green curves with stars, respectively. The wavelength is chosen to be 800nm, and the numerical aperture of the focusing objective is assumed to be 1.25, and refractive index is 1.59. Fig. 3.11(a) shows the results 100 nm sphere immersed in the oil (refractive index 1.51); Fig. 3.11(b) shows the results of 1 micron sphere immersed in the oil; Fig. 3.11 (c) shows the results of 100 nm sphere immersed in the water (refractive index 1.33); Fig. 3.11(d) shows the results of 1 micron sphere immersed in the water. Fig. 3.11 clearly shows that when refractive index of sphere is close to that of media, (a) and (b), or the size of scatterer is very small (a) and (c), the Born approximation methods are consistent with those calculated by using Mie's theory method. As expected, the results using vectorial formulism are much closer to Mie's theory results than those by using scalar formulism. When weak scatterer conditions

are not satisfied, Fig. 3.11 (d), there is much larger discrepancy existing between calculations from Born approximation and Mie's theory. But Born approximation methods can still represent the basic features in the scattered intensity.

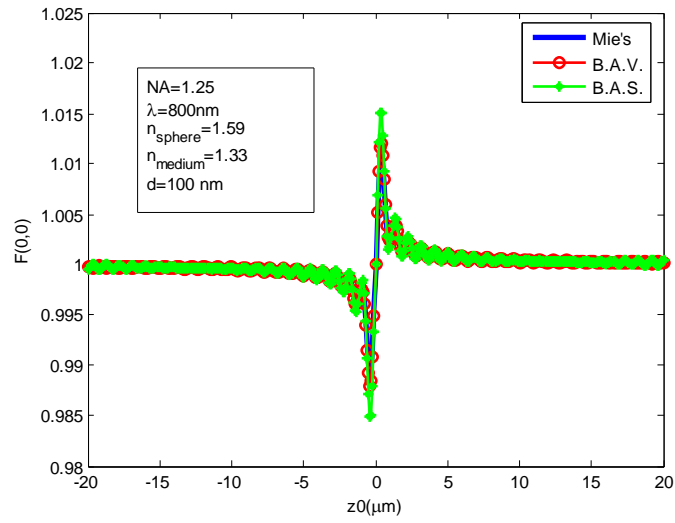
The normalized scattering spectra produced by non-spherical scatterer in the tightly focused supercontinuum beam are calculated by using vectorial formulism, Eq. (3-44), of Born approximation method. Fig. 3.12 displays the results of normalized scattering spectra of cubic scatter and spherical scatterers measured along the forward direction and the direction of polar angle at 30° . The refractive indices of scatterer and medium are 1.59 and 1.33, respectively. Fig. 3.12 (a) shows the scattering spectrum of scatterer size at 100 nm, and Fig. 3.13 (b) shows the results of scatterer size at 1 micron. The scattering spectra show dependence on the size and shape of the scatterer.



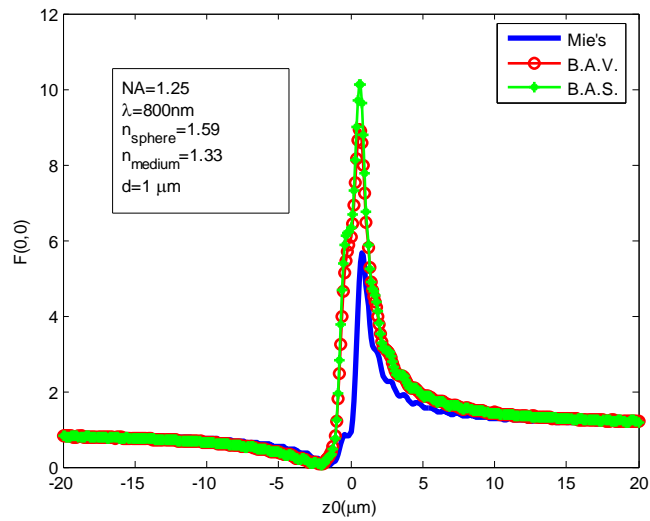
(a)



(b)

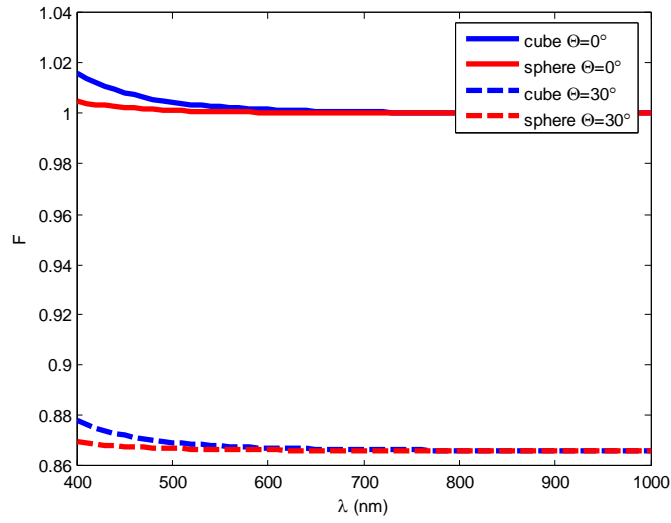


(c)

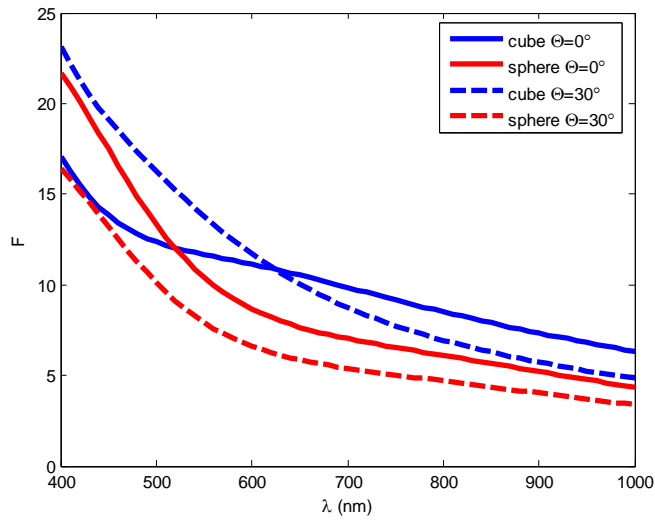


(d)

Figure 3.11 Normalized scattered intensity in forward direction of spherical scatterer located at different positions along z axis. Blue curves are calculated by using Mie's Theory. Red curves with circles and green curves with stars are calculated by using Born approximation method with vectorial and scalar formula, respectively. NA is 1.25, wavelength is 800nm, and refractive index of scatter is 1.59. (a) 100 nm sphere in oil; (b) 1 micron sphere in oil; (c) 100 nm sphere in water; (d) 1 micron sphere in water.



(a)



(b)

Figure 3.12 Calculated forward scattering efficiency $\lambda=800\text{nm}$, $\text{N.A.}=1.25$, $n_{\text{sphere}}=1.59$, $n_{\text{medium}}=1.33$, $d=100\text{nm}$ (a) and $d=1000\text{nm}$ (b). Solid curve is obtained by using Mie's theory and angular spectrum decomposition while the dotted one is obtained using Born approximation method.

3.6 Summary

In this chapter, we present theoretical models to analyze optical scattering by a single particle being trapped in white light supercontinuum optical tweezers. Mie's theory and angular spectrum decomposition method can be used to study the optical scattering spectra of a single uniform spherical scatterer. Analytical formulas for scattered waves in the forward and backward directions are derived when a spherical scatterer is placed on the z axis. The theory has also been used to calculate the scattering spectra of a single gold nanoparticle illuminated by tightly focused white light supercontinuum. Born approximation can be applied to analyze scattering by weak scatterers (e.g., the refractive index of the scatterer is close to surrounding medium or its size is small compared with wavelength) of non-spherical shape. The calculation results shows optical scattering spectrum depends on particle size, shape, refractive index, and resonant absorption. Single particle scattering spectroscopy in a supercontinuum trap can be a promising technique to non-invasively probe the properties of individual particles.

Chapter 4 Femtosecond Laser Beam Shaping

4.1 Introduction to beam shaping

Beam shaping is generally defined as a process to rearrange the intensity and phase of an optical light beam [9]. One of the simplest examples of beam shaping is probably that a plane wave is focused into a spot by a convex lens. The term “beam shape” stands for the intensity profile. The phase profile determines how the intensity profile evolves during propagation. A general beam shaping problem is to find an optical system that operates the incident beam to generate a desired intensity distribution, such as a uniform distribution at certain area on the target plane. The beam shaping technique has been investigated for both coherent and incoherent light beams.

Current beam shaping techniques can be categorized into two basic types: field mappers and beam integrators. Field mappers are designed for the incident beams with a known intensity profile; whereas integrators are designed for the relatively incoherent incident beams with less intensity information. The integrators are not so sensitive to beam alignment and beam size as field mappers; however, they are more easily affected by interference of coherent beam especially. Diffraction theory and geometric optics have been widely used in beam shaper design for different cases of application.

Since the first journal publication that introducing basic ideas of beam shaping by Roy Frieden in 1965 [110], the field of laser beam shaping has witnessed a steady

increase in research interests and practical applications. Today many important laser technologies have already made use of beam shaping, while some could potentially take advantages of the techniques in their applications, these include lithography, drilling in integrated circuit, packages and wiring boards, circuit component trimming, laser printing; material processing and formation, optical data storage, isotope separation, fiber injection; optical metrology, optical data/image processing, medical applications, as well as laboratory research [111-115].

Ultrafast lasers, as the name implies, have extremely high peak power in short time duration, and are very attractive in material processing, because they have been shown to increase efficiency and accuracy of material ablation, etching and cutting with less influence on the physical properties of the bulk material [116-119]. The current designs of beam shaping systems usually involve using monochromatic continuous wave (CW) laser. The aim of this chapter is to simulate and analyze the performance of ultrafast laser in the beaming shaping system.

4.2 Lossless beam shaping phase mask design

Figure 4.1 illustrates the typical beam shaping system. A laser beam with a initial intensity profile enters an aperture, where a diffractive optical element (DOE) is placed. The phase of incident beam will be modulated by the DOE. The desired intensity distribution will be obtained at the focal plane. If we assume the beam shaping lens is lossless, which means no energy absorption and blocking out exist in the system, i.e., the total energy of incoming and outgoing beams are the same.

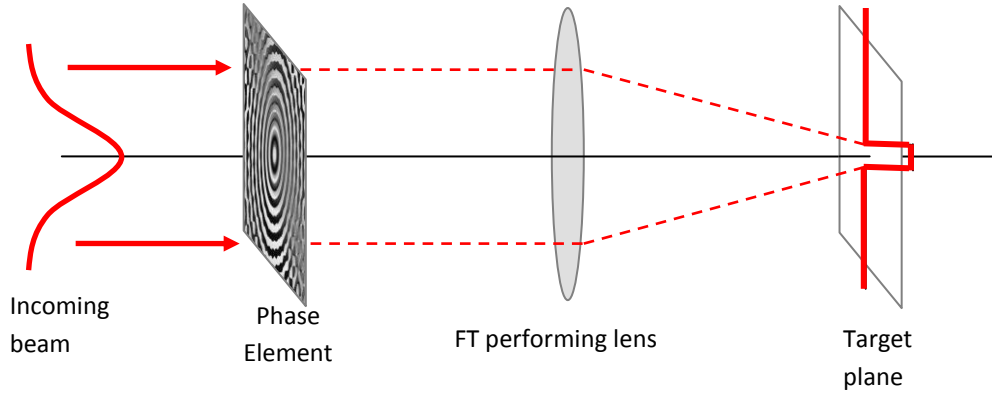


Figure 4.1 Schematic diagram of typical beam shaping system

The field on the incoming aperture together with that on the target plane is a Fourier transform pair. The uncertainty principle, which constrains the lower limit for the product of the root-mean-square (rms) width of a function and its rms bandwidth, must be taken into account. A dimensionless parameter β is used to evaluate the diffraction problem [9].

$$\beta = 2\pi \frac{R \cdot D}{\lambda f}, \quad (4-1)$$

where R is the characteristic length of incoming beam, D is the characteristic length of output beam, λ is the wavelength, and f is the focal length. How to convert a Gaussian intensity profile, the fundamental mode of laser, into a flat-top rectangular intensity profile, a favored beam profile by many applications, is a typical problem in the beam shaping studies. The 2-D Gaussian and 2-D rectangular functions can be decomposed into the products of two independent 1-D Gaussian functions and

rectangular functions, respectively. The 1-D functions are used in the following discussions without losing generality.

The one dimensional intensity profile of the unshaped laser is a Gaussian beam, given by $I_{input} = e^{-x^2/r_0^2}$, where r_0 is the Gaussian radius at 1/e intensity. The desired output intensity is flat-top rectangular with the width at $2r_f$. The dimensionless parameter β can be expressed as

$$\beta = \frac{2\sqrt{2\pi} \cdot r_0 r_f}{F\lambda}. \quad (4-2)$$

The efficiency of the field mapping problem of converting a Gaussian beam into a flat-top beam can be described in terms of the ranges of β as follows: for $\beta \geq 32$ one can obtain very good solutions and geometrical optics is applicable; for $4 \leq \beta \leq 32$ useful results may be obtained but they are not ideal; and for $\beta \leq 4$ one cannot achieve very good shaping of the beam [9]. Larger values of β make it possible to get steeper skirts and lower bumps on the output intensity profile. The factor β can be improved by increasing the input beam radius, expanding output spot size, decreasing wavelength, or reducing focal length.

To study the ultrafast laser beam shaping, we first designed the phase mask for a Ti:Sapphire femtosecond laser with center wavelength of 800 nm. The beam parameters are chosen as the following: $r_0 = 2$ mm and $r_f = 30$ μ m. The focal length of Fourier transform lens is assumed to be 50 mm. The calculated β is equal to 7.5199, phase mask designing can be achieved based on diffraction theoretic methods.

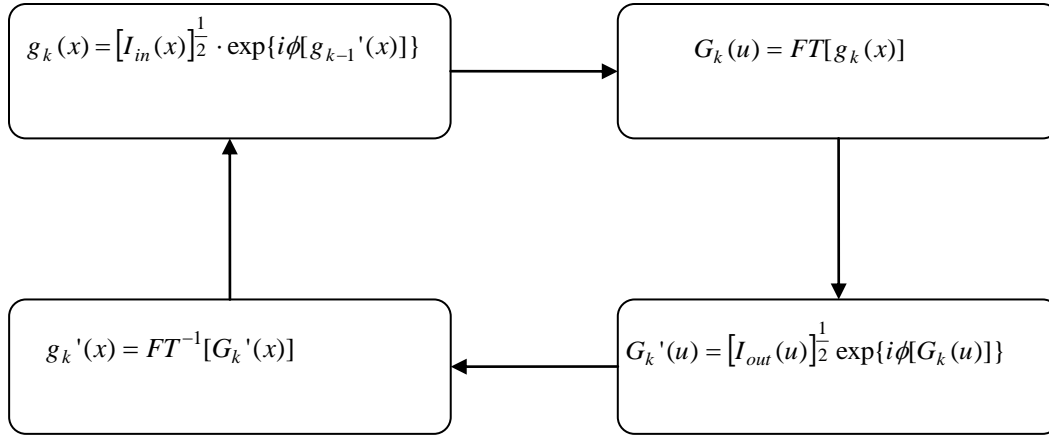


Figure 4.2 Diagram of Gerchberg-Saxton Iteration

Gerchberg-Saxton (GS) [10] and modified GS algorithms [11] have been thoroughly discussed and used to efficiently solve the phase-retrieval problems. A diagram of the iteration process is shown in Fig. 4.2. The term $I_{in}(x)$ is the intensity profile on the front focal plane of Fourier transform lens, and $I_{out}(u)$ is the desired intensity profile on the target plane. The k th iteration start from the electric field on the input plane, $g_k(x)$, of which amplitude is the square root of the intensity. The phase information of the electric field profile on the target plane $G_k(u)$ is extracted. In the meantime, the amplitude is replaced by the square root of the desired intensity $I_{out}(u)$. After performing inverse Fourier transform, the phase information is extracted for the (k+1)th iteration.

The modified GS algorithm, which was proposed by Liu and Taghizadeh[11], starts from $G_K(u)$ that is the result after the Kth GS iteration. This modified constraint

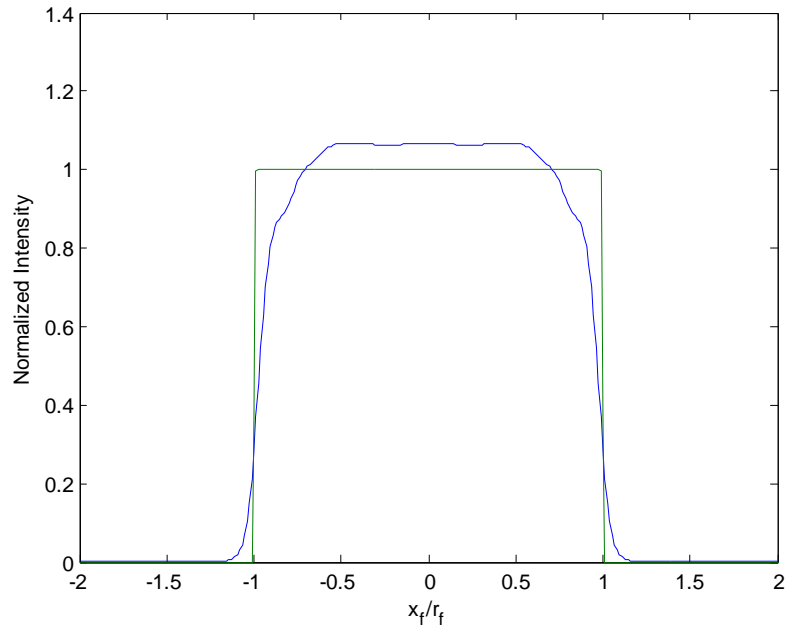
functions can be defined based on the difference between the desired and actual output profiles making it look like an ‘overcorrected’ version of the desired output,

$$F_{K+k}(u) = \begin{cases} \left| \frac{[I_{out}(u)]^{1/2}}{G_K(u)} \right|^c & |u| \leq r_f, \\ [I_{out}(u)]^{1/2} & |u| > r_f \end{cases} \quad (4-3)$$

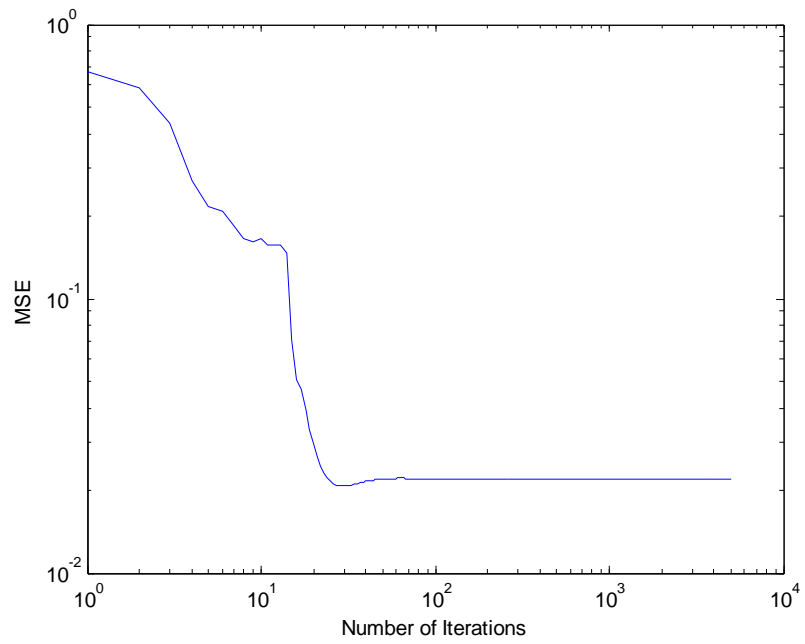
where c is a constant that can be manipulated. The iteration is usually evaluated by the normalized the mean square error (MSE) of the intensity at the target plane,

$$MSE = \frac{\sum_u |G_k(u)|^2 - I_{out}(u)|^2}{\sum_u |I_{out}(u)|^2}. \quad (4-4)$$

The simulation is implemented in the Matlab 7.0.4. The spatial size is chosen as 200 mm. Thus the resolution on the target plane will be $\lambda f/D = 0.2 \mu\text{m}$ for a grid of 2048 points. Figure 4.3 (a) shows the normalized intensity distribution of the output beam after 5000 GS iterations. We find that ~98.78% energy is constrained within the region, $|u| \leq r_f$. The corresponding MSE converges during the iterations as shown in Fig. 4.3(b).



(a)



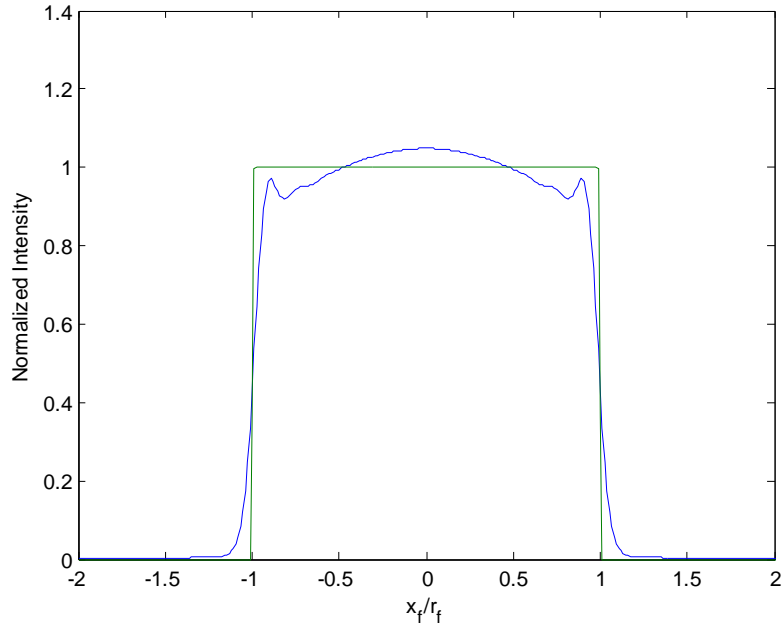
(b)

Figure 4.3(a) Normalized intensity distribution of designed flat-top beam after 5000 GS iterations. (b) Calculated MSE during the GS iterations

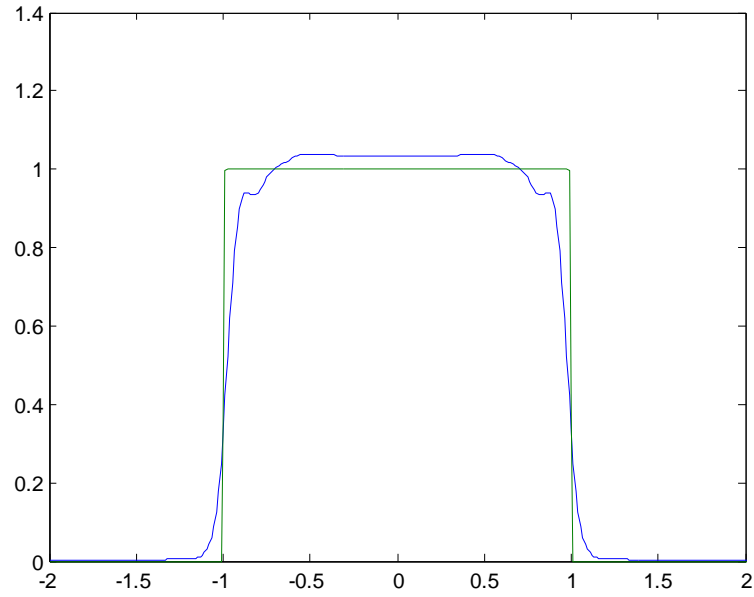
The convergence of the modified GS algorithm strongly depends on the selection of constant c . In our mask design process, the constant c and iteration numbers are optimized to find the minimum MSE during the first 200 modified GS iterations. The intensity profile after modified GS iterations with optimized constant c and iteration number is plot in Fig. 4.4(a). Approximately 99.68% of energy is constrained in the target region., but the intensity profile is still far away from the flap-top profile. That is because optimization of MSE of the intensity profile does not help to improve the flatness of the intensity profile. Therefore a new evaluation criterion is introduced,

$$FLAT = \frac{\left| |G_k(u)|^2 - |G_k(0)|^2 \right|^2}{|G_k(0)|^2} \quad |u| < r_f - \delta, \quad (4-5)$$

where $u = 0$ is the center of the target plane, and the subset δ is introduce to reduce the weight of boundary in the evaluation criterion. The smaller FLAT number is, the flatter intensity profile is in center part on the target plane. After similar optimization process for constant c and iteration number, the intensity profile is plot in Fig. 4.4(b). A flatter top intensity profile is achieved. In the meantime, the ratio of energy constrained in the target region improves to 99.83%.



(a)



(b)

Figure 4.4 Normalized intensity distribution of designed flat-top beam after modified GS iteration (a) optimized for minimum intensity MSE (b) optimized for flatness in the center part of intensity profile.

4.3 Beam Shaping with Femtosecond Laser

The use of femtosecond lasers for microprocessing applications has been widely studied in recent years as reduced thermally affected zones have been put in evidence around the irradiated area, unlike for nanosecond laser processing. How the distortion affects an ultrafast pulsed laser, which covers a wide frequency bandwidth, passing through the beam shaping system designed for a monochromatic laser, has not been fully investigated. In this section, femtosecond laser beam shaping is studied by simulation.

The amount of phase modulation by DOE is inversely proportional to wavelength as given by,

$$\varphi(\lambda) = 2\pi n(\lambda)l / \lambda, \quad (4-5)$$

where $n(\lambda)$ is the refractive index, and l is the thickness of DOE phase mask. When the dispersion of the material is small enough to be ignored, the amount of phase modulation can be expressed in the terms of φ_0 , which is phase modulation for the design wavelength λ_0 ,

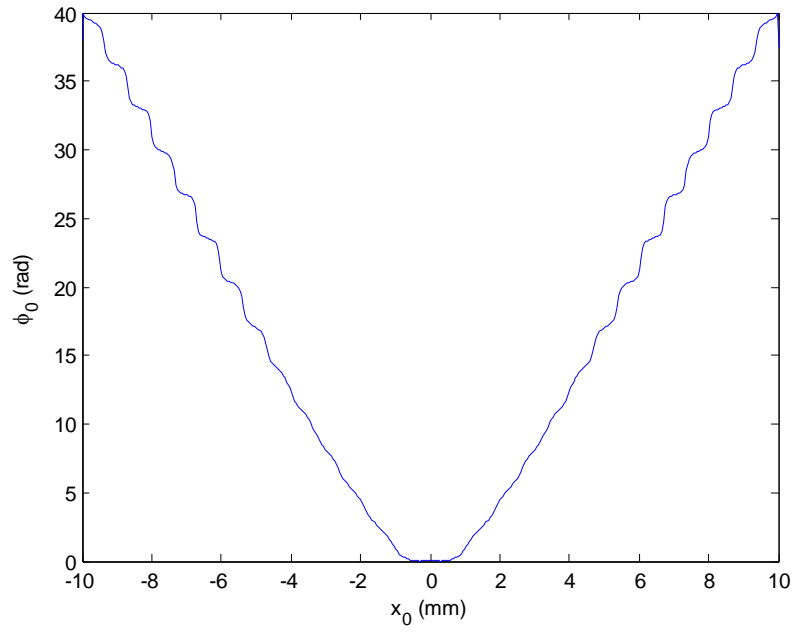
$$\varphi = \frac{\lambda_0}{\lambda} \varphi_0. \quad (4-6)$$

When a wrapped phase mask is employed in the real applications due to various reasons, such as the limit of thickness or inadequate dynamic range of the DOE, an

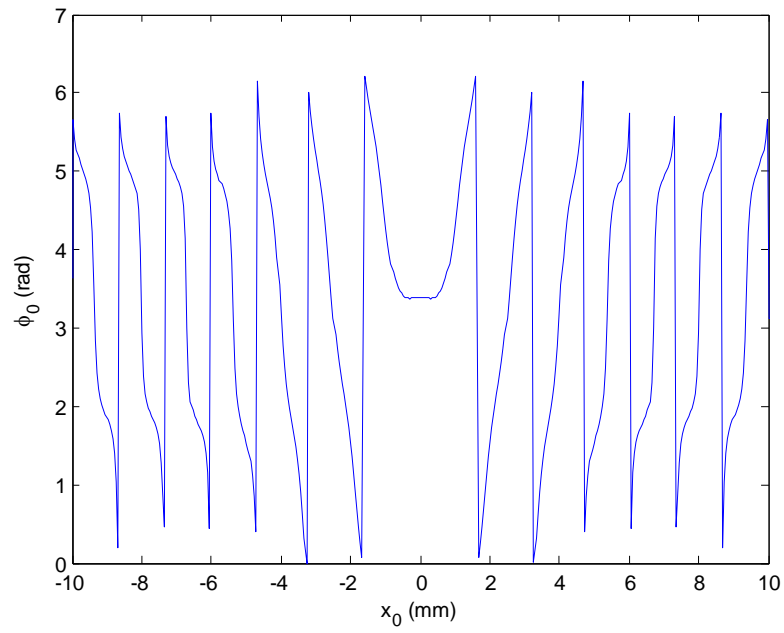
additional phase shift will be introduced by a N-folds wrapping phase mask, which can be expressed as,

$$\Delta\phi_w = 2\pi N \frac{\lambda_0}{\lambda} . \quad (4-7)$$

The phase mask designed for intensity profile Fig. 4.4 (b) is used in the following simulation. The size of the phase mask is assumed to be 20 mm. Fig. 4.5(a) plots the amount of phase modulation for the center wavelength 800 nm. The DOE with wrapped phase design is also taken into consideration, shown in Fig. 4.5(b).



(a)



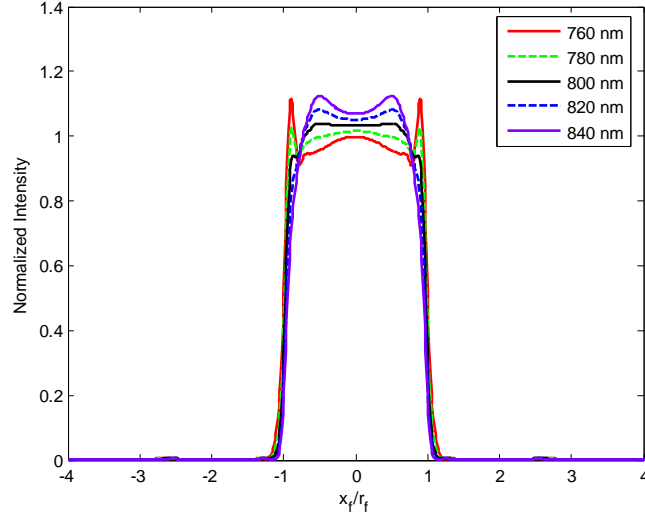
(b)

Figure 4.5 Phase distribution of optimized DOE (a) unwrapped phase (b) wrapped phase from 0 to 2π

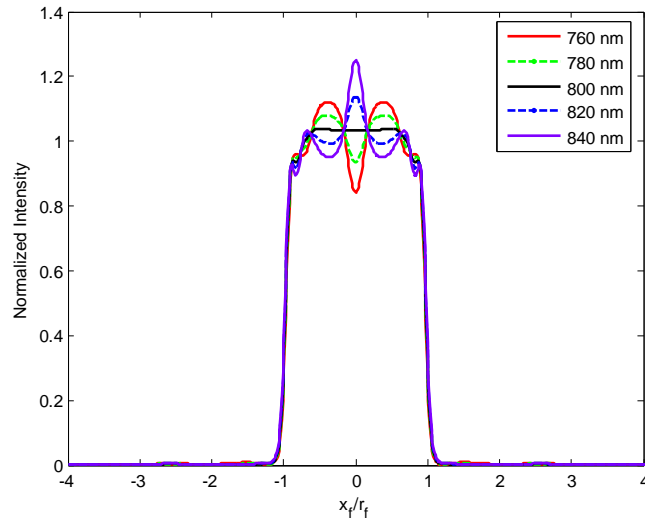
Shorter pulses result in a wider spectrum. We consider a 20-fs laser pulse with a Gaussian intensity profile with spectrum bandwidth of about 50 nm, is used in our simulation. First, the intensity profiles of different wavelengths are investigated. Fig. 4.6 (a) and (b) display the normalized intensity profiles for different wavelengths by using phase-unwrapped and phase-wrapped masks, respectively. It is observed, in our beam shaping simulation using unwrapped phase mask, at longer wavelengths (where the phase shift will be less than ideal) that the edges of the spatial profile are significantly lowered while the center is raised. For shorter wavelengths, the reverse is true with a dip appearing in the center of the profile and the edges becoming over-emphasized. The amount of deformation increases with difference between the applied wavelength and the center wavelength. In the simulation using wrapped phase masks, the distortion of intensity profiles become more obvious, as more ripples come into the plateau. But, in the case of both wrapped and unwrapped phase masks, the skirts of plateau are still steep, and changes of sizes are very small.

The intensity profiles of a 20 fs laser pulse with Gaussian profile passing through beam shaping system with unwrapped and wrapped phase mask are plotted in Fig. 4.7 (a) and (b), respectively. It can be observed that the pulse is delayed when using unwrapped phase mask more than that when wrapped phase mask is used, which is because the total amount of phase modulation of unwrapped phase mask is larger. However the relative phase shift to the designing wavelength of wrapped phase mask is larger, which results in a larger distortion. Fig. 4.8 shows the full-width-half-

maximum (FWHM) pulse widths on the target plane. The changes of pulse widths are less than 5% in the center plateau area.

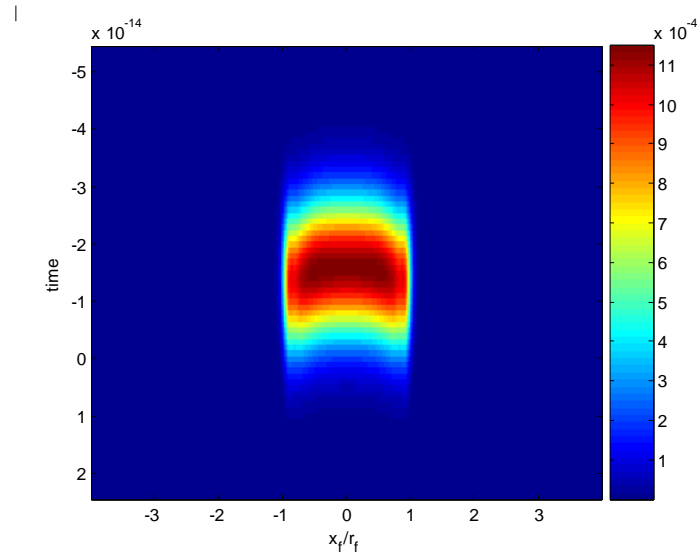


(a)

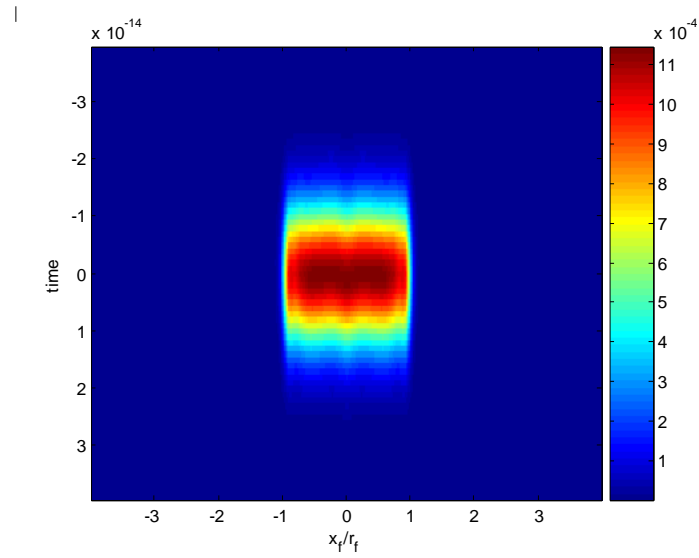


(b)

Figure 4.6 Normalized intensity profile of (a) unwrapped phase mask (b)

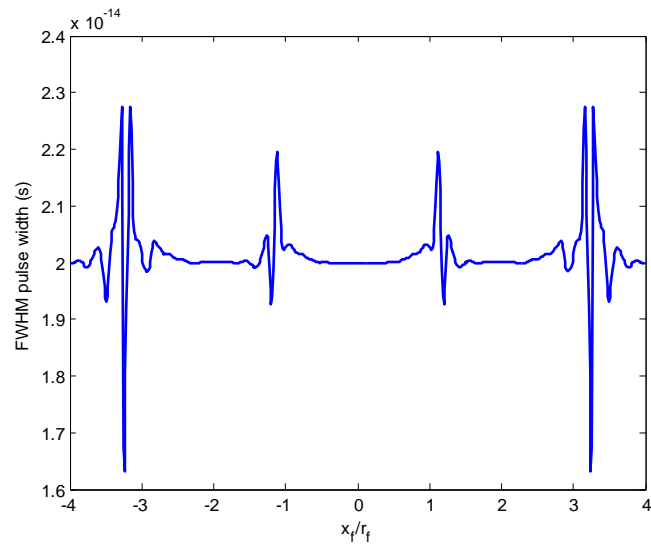


(a)

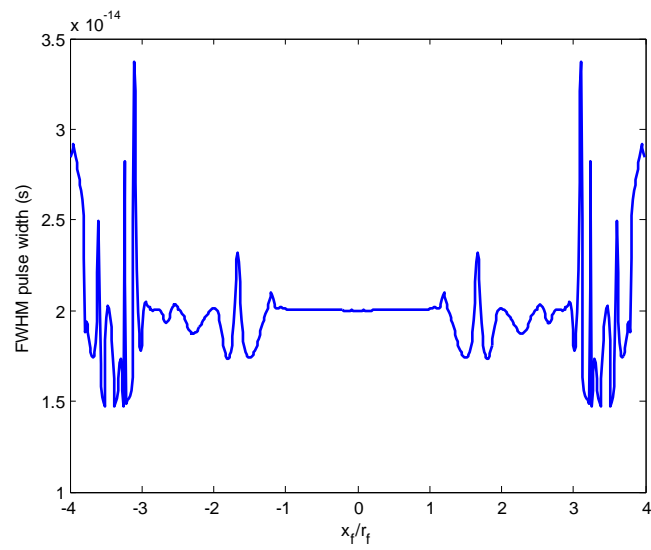


(b)

Figure 4.7 Pulse profiles of a 20 fs pulse passing through beam shaping system. (a) using unwrapped phase mask; (b) using wrapped phase mask

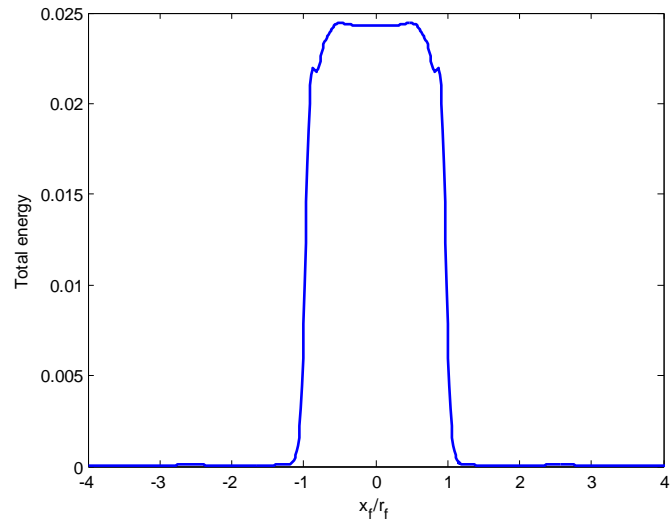


(a)

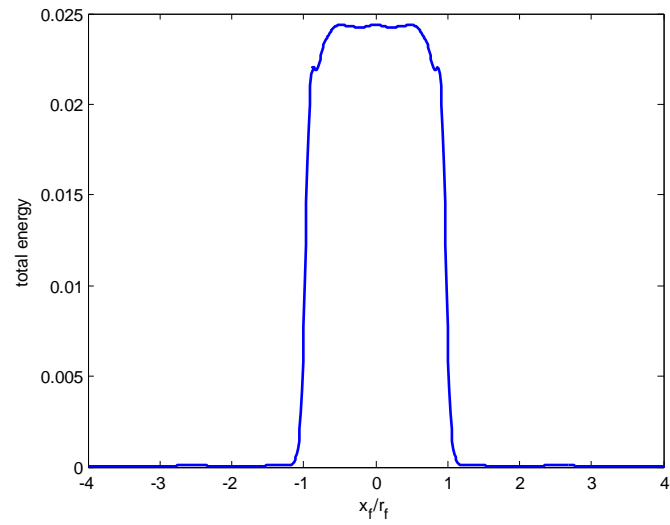


(b)

Figure 4.8 FWHM Pulse width of a 20 fs pulse passing through beam shaping system. (a) using unwrapped phase mask; (b) using wrapped phase mask



(a)



(b)

Figure 4.9 Total energy distribution of a 20 fs pulse passing through beam shaping system. (a) using unwrapped phase mask; (b) using wrapped phase mask

The total energy distributions of laser pulses on the target plane are calculated and plotted in Fig 4.9. Total energy distributions of femtosecond lasers passing through wrapped and unwrapped phase masks basically keep approximately the same shape as the intensity distribution of design wavelength. A small fluctuation appears on the plateau part of wrapped phase mask. The pulse energies restrained in the center part are, 98.34% and 98.36% of total energy for unwrapped and wrapped phase masks, respectively, which are slightly less than that of the design wavelength.

From the simulations above, we can find that although intensity profiles of wavelengths shifted from the system design suffer a distortion when passing through beam shaping system, pulse energy profiles change little for femtosecond pulses. The reason behind can be explained as following. The electric field on the target plane, $G(u; \lambda)$, is the Fourier transform of input field, $g(x)$, with the phase modulation $\phi(x)$ from the mask,

$$\begin{aligned} G(u; \lambda) &= \int_{-D/2}^{D/2} g(x) e^{i\phi(x)} e^{-i2\pi \frac{ux}{\lambda F}} dx \\ &= \int_{-D/2}^{D/2} g(x) e^{i \frac{\phi_0(x)\lambda_0}{\lambda}} e^{-i2\pi \frac{ux}{\lambda F}} dx \end{aligned} \quad (4-8)$$

The center part of the phase modulation $\phi_0(x)$ is flat and close to zero, $\phi_0(|x| < 0.28r_0) \leq 0.05$, where most of energy are located. Another reason is the relative amplitude of $g(x)$ decays at the order of $e^{-\Delta\omega^2}$, where $\Delta\omega$ is the frequency shift. In other words, the

frequency components with larger distortion have less weight in the pulse energy, and the performance of center frequency components dominate.

4.4 Summary

Specially shaped laser intensity profiles are desired both by basic science research and practical industry applications. Triggered by such demands, beam shaping technology has boomed. Beam shaped femtosecond pulsed lasers have found many opportunities for applications in various fields such as material microprocessing.

In this chapter, beam shaping technologies are briefly reviewed. A beam shaping system is designed for shaping a Gaussian Ti:Sapphire femtosecond laser beam into flattop profile by using modified Gerchberg-Saxton (GS) algorithm. A new criterion for the optimization process used in the beam shaping process is described. Comparing with the results from optimizing the intensity profile mean square error (MSE), total intensity falling in the center target region has increased from 99.68% to 99.83%, and in the meantime, better intensity profile is obtained.

The properties of an ultrashort (20 fs) pulsed laser are investigated by numerical simulations after passing through beam shaping system. Both phase-wrapped and phase-unwrapped modulations are considered in the calculations. The simulation results show that the intensity profile suffers distortion when working wavelength is different from the design wavelength, especially for using wrapped phase mask. However the distortions for the femtosecond laser pulses are much less, though still observable. The FWHM pulse widths changes less than 5% in the center region,

because the larger distortion components have much smaller intensity, and the performance of center frequency dominates.

Chapter 5 Terahertz generation

5.1 Background

The term terahertz (THz) radiation refers to the electromagnetic wave with wavelength between 1000 and 100 microns (corresponding to 0.3THz and 3 THz). THz waves fill the intermediate region between millimeter-wave band and far infrared (FIR).

Electromagnetic waves in the THz region can penetrate a wide variety of non-conducting materials: clothing, paper, cardboard, wood, masonry, plastic ceramic and so forth. THz radiations of certain frequencies can even penetrate tissues of several-centimeter-thickness and then scatter back [120]. Many materials of interest, such as plastic explosives, display characteristic spectral fingerprints in the THz region. Besides these factors, THz radiation is non-ionizing, since the photon energy is four orders of magnitude less than that of X-rays. This means that investigations with biological materials, such as living organisms or cells, do not result in harmful effects to the DNA [120].

Because of these unique properties, THz radiation has very attractive potential applications in many fields of scientific research and engineering, examples include biomedical imaging, security screening, remote sensing, and spectroscopy. However, extensive investigations with THz radiation and development of applications have been impeded for several reasons. One is the lack of THz generating sources.

As mentioned above, the wavelengths of THz radiation are distributed between those of millimeter wave and FIR. Therefore, current approaches of generating THz come from technologies of both areas. Many traditional methods for generating radio-frequency waves and microwaves have been extended to the THz range. Examples include backward wave oscillator (BWO) [121], and directly multiplied sources. Frequencies of THz radiation generated by these electronic methods are, not surprisingly, limited to the low frequency end, usually less than 1.5 THz. On the other hand, it is difficult to find a blackbody emitter for a terahertz light source. Rapid advances of current laser technologies have promoted the development of THz lasers. THz lasers typically involve using four laser techniques: different frequency mixing [122], terahertz parametric oscillators [123], molecular gas lasers [124] and quantum cascade lasers [125]. So far the highest output power of THz lasers can be even greater than 100 mW. However its intrinsic property of narrow specific wavelength bands makes it have limitation for spectroscopy application. The prominent method is optical rectification of ultrafast laser pulses using biased semiconductor switches [126] or 2nd order nonlinear crystal [13]. When ultrafast laser pulses illuminate switches or crystals, electromagnetic wave will be emitted. If the pulses are of a few picoseconds or hundreds of femtoseconds, the frequencies of generated electromagnetic wave can fall into the terahertz region. Combined with the THz time-domain spectroscopy systems (THz-TDS) [127], optical rectification systems are easy to be realized, and have been widely used to generate broadband terahertz radiation. So far,

photoconductive switches produce THz pulses with higher energy and higher average power, but maximum frequency of these pulses is below 1 THz [128].

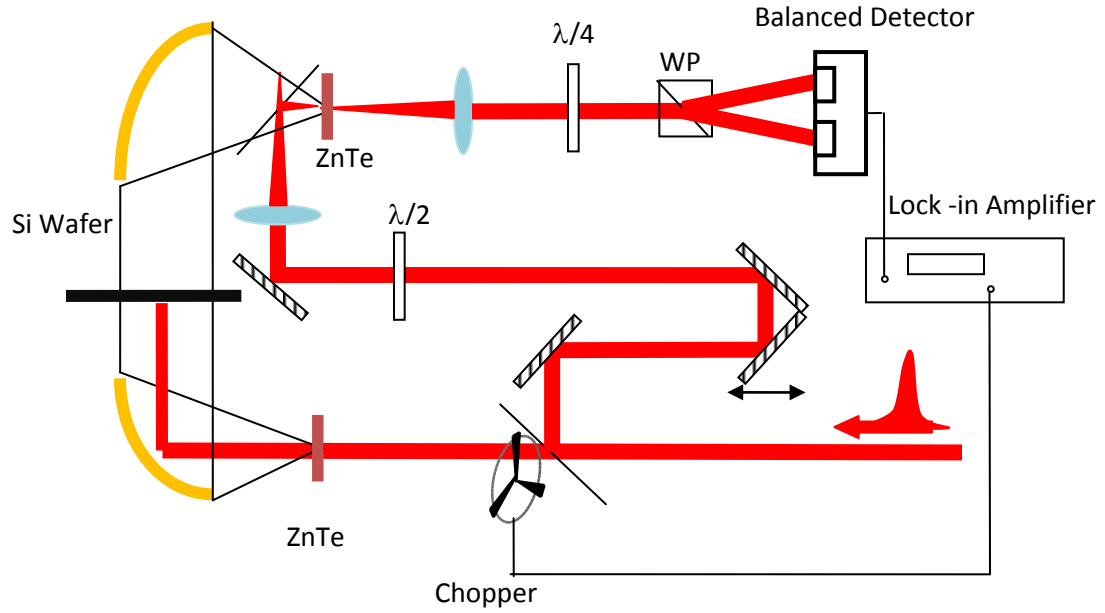
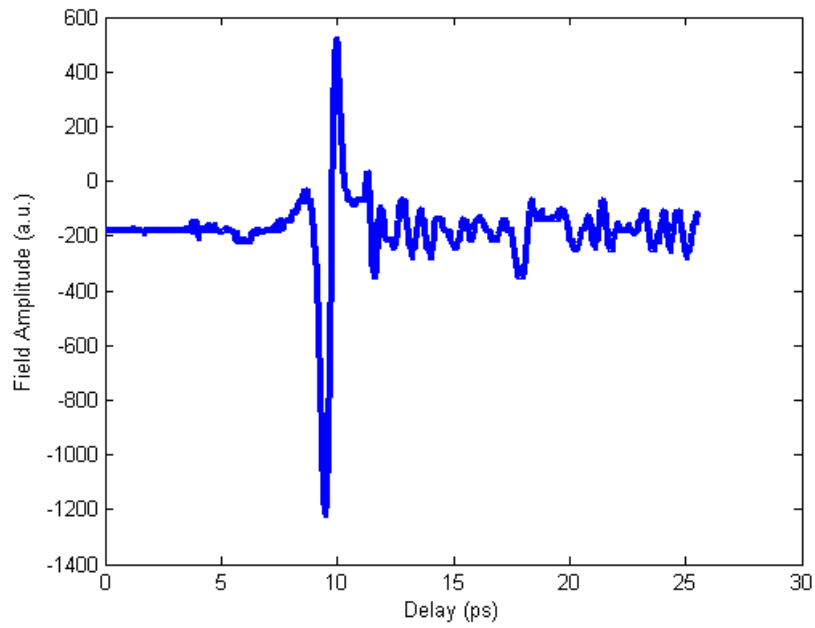


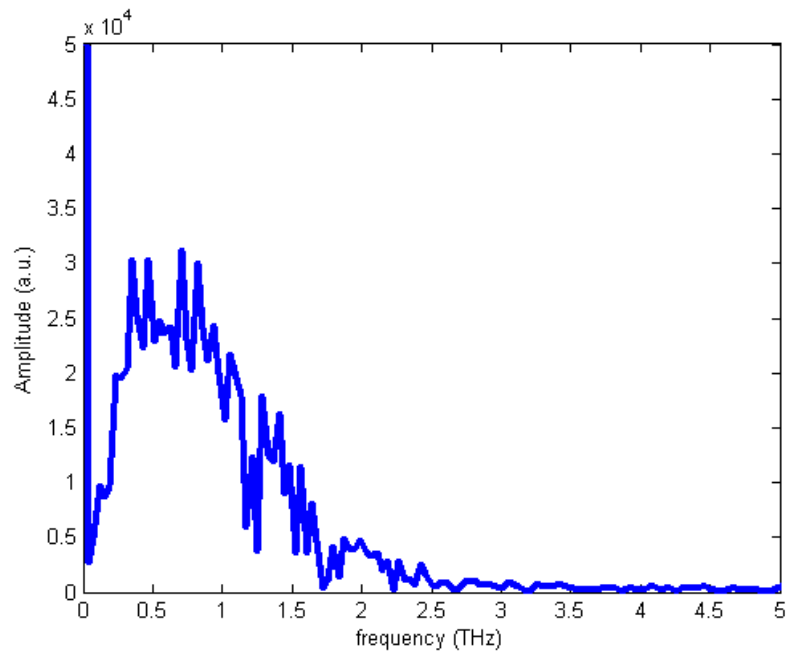
Figure 5.1 A schematic diagram of experimental setup of THz generation and THz-TDS detection.

Fig. 5.1 is the schematic diagram of experiment setup to generate THz radiation, and to detect it with THz-TDS system. The incoming femtosecond laser pulses are generated from Quantronix PM30 (pulse energy ~ 1.3 mJ per pulse, repetition rate 1 kHz). The laser beam is split into two beams, pumping and probing, by an uncoated pellicle beam splitter (Thorlabs). About 92% of the energy coming into the pump beam illuminates a 1-mm-thickness ZnTe $\langle 110 \rangle$ crystal. The THz radiation is collected by a pair of 90 degree off axis parabolic mirrors, which have the focal lengths of 4 inches. A high resistance silicon wafer was used to block the pump beam. The probe beam was weakly focused by a lens after the computer controlled delay

line. The probing beam and terahertz beam are recombined by a 50%/50% pellicle beam splitter. A 1-mm-thickness $\langle 110 \rangle$ ZnTe crystal is placed at the focal point of the terahertz beam. The collected probe beam first passes through a quarter wave plate, where it is circularly polarized, then through the Wollaston prism, where it is split into two linearly polarized beams, which are coupled into a balanced detector. When measuring the terahertz signals, a chopper is inserted into the pump beam before the focal lens to modulate the pump. The signal comes from the balanced detector is amplified by a lock-in amplifier. A terahertz waveform is obtained by sweeping the delay between the pump and probe laser pulses. Fig. 5.2 shows the typical THz time domain pulse profile and frequency domain spectrum measured by the setup in Fig 5.1.



(a)



(b)

Figure 5.2 the typical THz time domain pulse profile and frequency domain spectrum generated by 1 mm thickness ZnTe

The physics of THz generation of optical rectification in the second order nonlinear optical crystal can be mathematically described as follows. Consider a train of sub-picosecond laser pulses propagating in a second order nonlinear material. Assuming the propagation direction is along the z direction, the electric field of the pump laser can be written as

$$E_p(z,t) = \frac{1}{2} \tilde{\mathcal{E}}(z,t) \exp(\omega_p t - k_p \cdot z) + c.c. \quad (5-1),$$

where ω_p and $k_p = 2\pi/\lambda_p$ are the carrier frequency and wave vector, $\tilde{\mathcal{E}}(z,t)$ is the pulse envelope, which is slowly varying in t and z, and c.c means the term of complex conjugate. The THz radiation is guided by the Maxwell's equations

$$\begin{aligned} \nabla \times E_{THz} &= -\mu_0 \frac{\partial H_{THz}}{\partial t} \\ \nabla \times H_{THz} &= \frac{\partial(\epsilon_0 n_T^2 E_{THz} + P^{NL})}{\partial t} \end{aligned} \quad , \quad (5-2)$$

where n_T is the refractive index. The nonlinear polarization P^{NL} arises from the second order nonlinearity of the medium,

$$P^{NL} = \epsilon_0 d_{eff} E_p E_p \quad , \quad (5-3)$$

where d_{eff} is the nonlinear coefficient. In the frequency domain the electromagnetic wave equation of THz wave (denoted by overbar in the following discussion) can be expressed as

$$\left[\nabla^2 + \frac{\Omega^2}{c^2} n_T^2(\Omega) \right] \bar{E}_{THz} = \frac{2d_{eff}}{c^2} \int_{-\infty}^{\infty} \left(\frac{\partial^2 E_p^2}{\partial t^2} \right) \exp(-i\Omega t) dt, \quad (5-4)$$

where Ω denotes the frequency at THz region. If we substitute Eq.(5-1) into Eq.(5-4) and only consider the low frequency terms, the wave equation for the THz wave is given by

$$\left[\nabla^2 + \frac{\Omega^2}{c^2} n_T^2(\Omega) \right] \bar{E}_{THz} = -\frac{d_{eff}\Omega^2}{c^2} \overline{|\tilde{\mathcal{E}}|^2}, \quad (5-5)$$

where THz radiation is related to the pulse envelopes of the pump pulses. As we discussed above, the power of THz wave is a few orders of magnitude smaller than that of the pump laser, so the effect of the polarization induced by the THz wave can be ignored. If we ignore diffraction, the wave equations can be further simplified to

$$\left[\frac{\partial^2}{\partial z^2} + \frac{\Omega^2}{c^2} n_T^2(\Omega) \right] \bar{E}_{THz} = -\frac{d_{eff}\Omega^2}{c^2} \overline{|\tilde{\mathcal{E}}|^2}. \quad (5-6)$$

The pulse envelopes evolve in the crystal due to dispersion,

$$\tilde{\mathcal{E}}(z, t) = \frac{1}{2\pi} \int_{-\infty}^{\infty} \tilde{\mathcal{E}}(z=0, \Omega) \exp\{i[\Omega t - (k - k_p)z]\} d\Omega, \quad (5-7)$$

where k is the wave vector at frequency $\Omega + \omega_p$. $\tilde{\mathcal{E}}(z=0, \Omega)$ is the Fourier transform of the profile of the complex electric field in the temporal domain at the input facet, $\tilde{\mathcal{E}}(z=0, t)$, and,

$$\bar{\tilde{\epsilon}}(z=0, \Omega) = \int_{-\infty}^{+\infty} \tilde{\epsilon}(z=0, t) \exp(-i\Omega t) dt \quad . \quad (5-8)$$

Finally, Eq. (5-6) together with Eq.(5-7) can be used to analyze the THz wave generation in the second order nonlinear optical crystal initiated by optical rectification ultrashort pulses.

High Power broadband terahertz (THz) radiation sources are always desirable. However, THz radiation generated by optical rectification of ultrafast pulsed lasers in nonlinear crystals is usually at the level of nanowatts. The energy conversion efficiencies from pump lasers to THz frequencies are usually less than 10^{-5} . Three key factors limit the energy conversion efficiency: Manley-Rowe photon conversion limit [129]; absorption and dispersion; and short interaction length. Manley-Rowe relations claim that from quantum view, the number of the THz photons cannot exceed the number of the optical pumping photons. We can roughly estimate the upper limit of energy conversion efficiency to generate a 1 THz frequency from a typical Ti:Sapphire laser,

$$\frac{h\nu_{THz}}{h\nu_{IR}} = \frac{\lambda_{IR}}{\lambda_{THz}} = \frac{800\text{ nm}}{300\text{ }\mu\text{m}} = 2.6 \times 10^{-3} \quad .$$

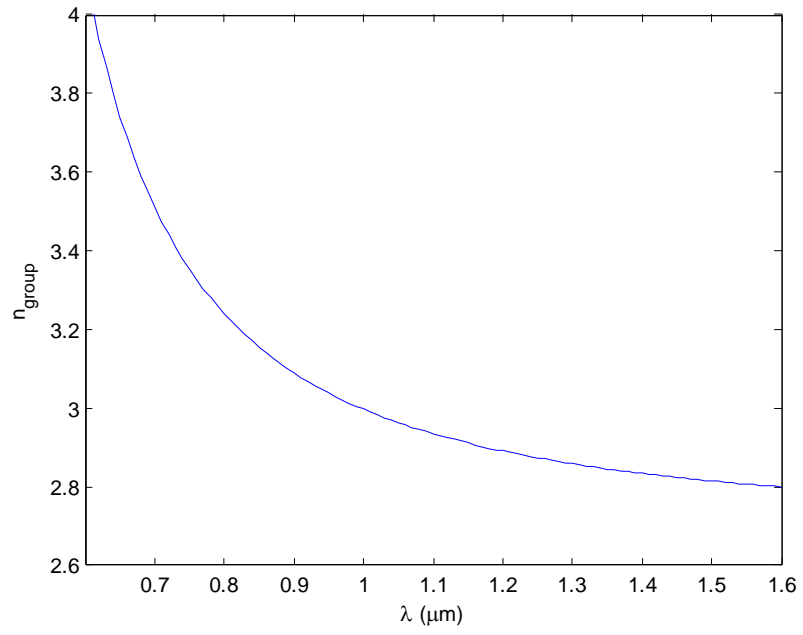
The nonlinear crystals usually have strong absorption in the terahertz region. So cooling the crystals to low temperature can increase the conversion efficiency [14]. Longer interaction lengths are desirable, necessitating appropriate consideration of phase matching constraints. The phase matching condition for the optical rectification

process (collinear difference frequency mixing) is given by $\Delta k = k(\omega_{opt} + \omega_{THz}) - k(\omega_{opt}) - k(\omega_{THz}) = 0$, where ω_{opt} and ω_{THz} are the optical and THz frequencies, respectively, and ω_{opt} and $(\omega_{opt} \pm \omega_{THz})$ lie within the spectrum of the optical pulse. We can express the coherence length $L_c = (\pi/\Delta k)$ as [130]

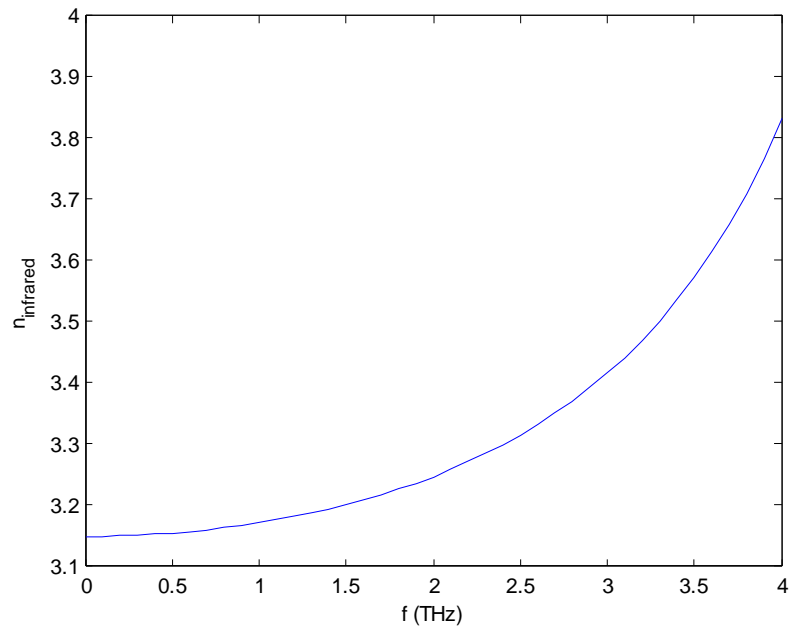
$$L_c = \frac{\lambda}{2|n_{gp} - n_{THz}|}, \quad (5-9)$$

where λ is the wavelength at terahertz signal, n_{gp} is the group index of pump laser, and n_{THz} is the refractive index of THz.

Due to the dispersion of nonlinear crystals, usually only a narrow-band THz frequency can satisfy the phase matching condition, which depends on the carrier frequency of the pump beam. For example, ZnTe is one of most popularly used optical rectification crystals. The refractive index of ZnTe crystal in the optical region is given as $n = \sqrt{4.27 + 3.01\lambda^2 / (\lambda^2 - 0.142)}$ [131], where λ is the wavelength in microns. The refractive index of ZnTe crystal at THz frequencies can be found from $n = \sqrt{289.27 - 6f^2 / (29.16 - f^2)}$ [132], where f is the frequency in the unit of THz. Fig. 5.3 shows the group indexes in the optical region and refractive index in the terahertz region. Coherence lengths for pumping pulse with different central frequencies are plotted in Fig. 5.4(a). The corresponding calculated terahertz spectra generated in a 1-mm-thick ZnTe crystal, where absorptions are ignored in calculation, are plotted in Fig. 2(b), respectively.

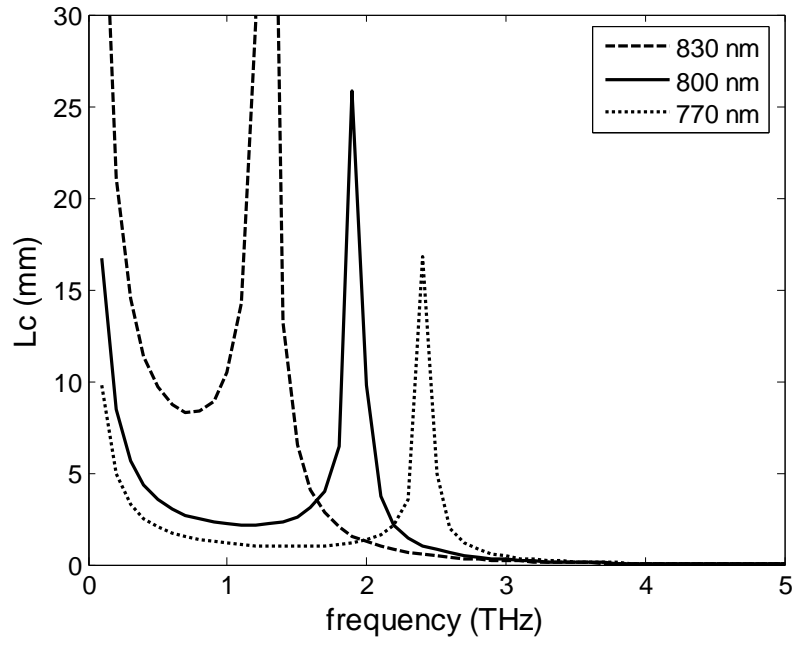


(a)

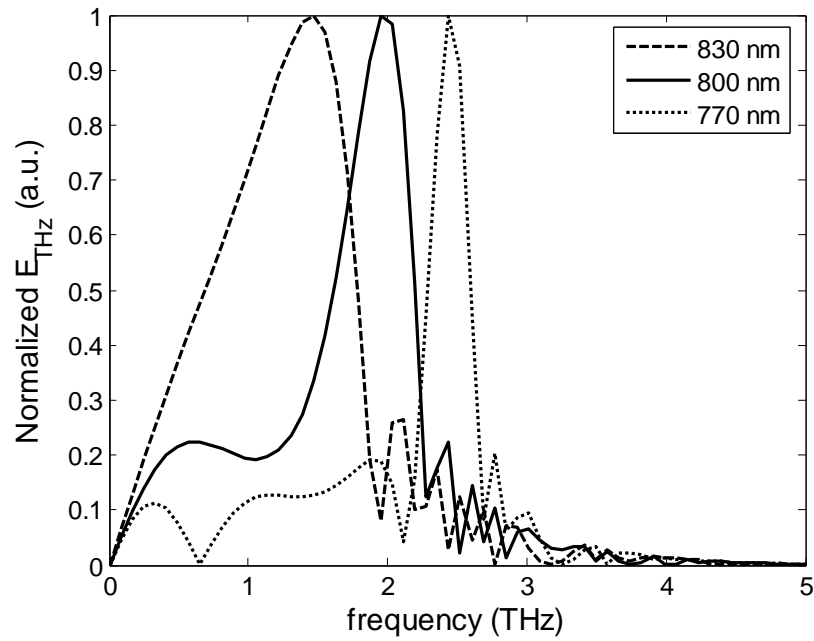


(b)

Figure 5.3 Group index in visible region(a) and refractive index in FIR(b) of ZnTe



(a)



(b)

Figure 5.4 Coherence lengths in ZnTe and terahertz spectrum. Coherence lengths (a) for three different pump laser wavelengths (830, 800, and 770 nm) are shown to compare with the terahertz spectra (b).

A number of methods have been developed to improve the phase matching condition. For instance, periodic poled structures make it possible to satisfy quasi phase matching conditions [133-135]. Cherenkov cone [136] and tilt wave front [128, 137-139] properties can make phase matching condition fulfilled at a certain angle. A method using supercontinuum as pump source to improve the THz generation efficiency will be discussed in this chapter.

5.2 Terahertz generation by optical rectification of supercontinuum

As discussed above, optical rectification of ultrashort laser pulses is a widely used schemes of broadband THz generation for laboratory research. However, the strong dispersion of nonlinear crystals in the optical and near-infrared regions usually limits the phase-matching condition between pump pulses and THz pulses, while it limits the conversion efficiency and bandwidth of the THz pulses. For instance, ZnTe is a popular nonlinear crystal used in the lab for optical rectification terahertz generation. For the typical pumping laser, a mode-locking Ti: sapphire femtosecond laser working at 800nm, phase matching condition is satisfied for the frequency of about 2 THz [130]. It has been demonstrated that the phase matching condition can be modulated at the desired terahertz frequency by using a femtosecond pulse shaping technique [140, 141]. However most of the energy of pumping laser pulses is lost during the pulse shaping process.

Recently it has been reported that when ultrashort laser pulses are coupled into highly nonlinear photonic crystal fibers [7], supercontinuum is generated during the intense nonlinear process [5]. The physics behind SC generation in PCF is addressed in Chapter 2. When nonlinear PCF is pumped at anomalous GVD regions, the soliton-related nonlinear effects will involve in the SC generation. Even if the PCF is only a few millimeter long, the supercontinuum spectrum can be broadened to a few hundred nanometers. At the same time, the time domain pulse duration is still kept within the range of subpicoseconds. In this case supercontinuum can be considered as the superposition of a series of pulses with different central frequencies. Therefore if supercontinuum was used as the pump source, phase matching condition can be satisfied in a broad region.

The evolution of the pulse propagating in the fiber can be mathematically described by generalized nonlinear Schödinger equations (NLSE) [142]

$$\frac{\partial E(z,t)}{\partial z} + \frac{\alpha}{2} E(z,t) - \sum_{n \geq 1} \frac{i^{n+1}}{n!} k^{(n)} \frac{\partial^n E(z,t)}{\partial t^n} = i\gamma \left(1 + \frac{i}{\omega_0} \frac{\partial}{\partial t}\right) E(z,t) \int_{-\infty}^{+\infty} R(\tau) |E(z,t-\tau)|^2 d\tau ,$$

(5-10)

where $E(z,t)$ is the complex electric field profile of pulse in the coordinate traveling at

the speed of group velocity of carrier, $v_g = \left. \frac{d\omega}{dk} \right|_{\omega_c}$, and ω_c is the angular frequency of

carrier. The left side of Eq. (5-10) describes linear propagation of pulse in the fibers.

The second term is the loss. And the third term presents the dispersions in the fiber.

The right side of Eq. (5-10) is the nonlinear effects involved in the SC generation. The self-steepening effects are represented by time derivative. The nonlinear response of the fiber, such as Raman scattering and Kerr effect, are expressed as a convolution with a response function $R(\tau)$, which is given by [142, 143],

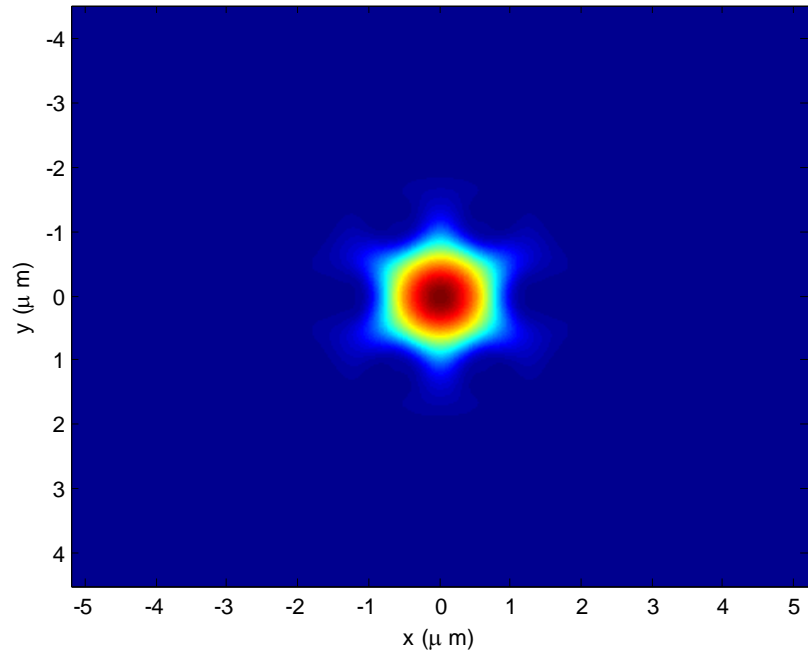
$$R(\tau) = (1 - f_R)\delta(\tau) + f_R h(\tau) \quad , \quad (5-11)$$

where f_R is the ratio of the contribution from Raman scattering in the fiber, which is taken as 0.18 in the calculation[142]. The term $h_R(\tau)$ is the Raman response which can be modeled as a single Lorentzian line[143]

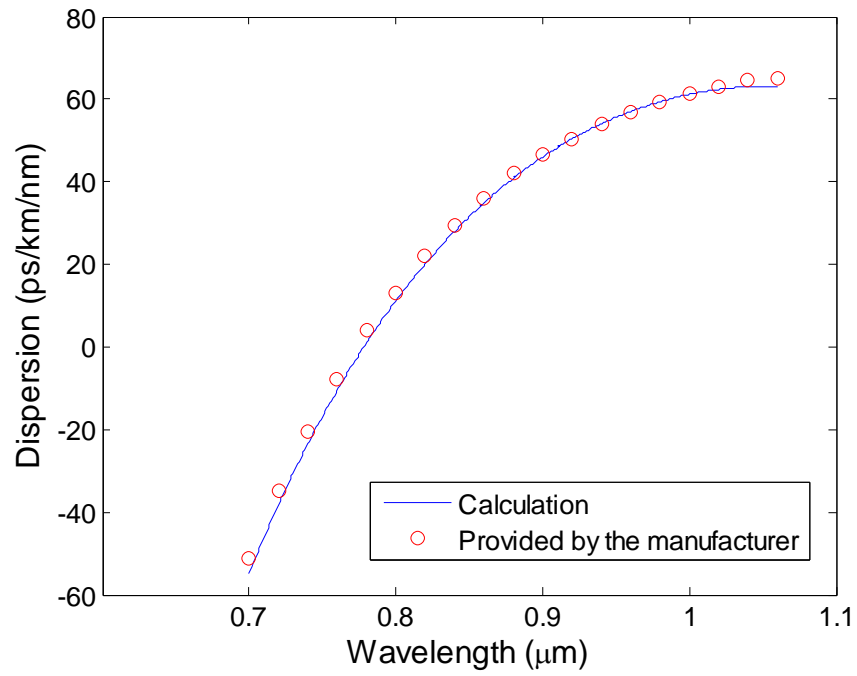
$$h_R(\tau) = \frac{\tau_1^2 + \tau_2^2}{\tau_1 \tau_2^2} \exp(-\frac{\tau}{\tau_2}) \sin(\frac{\tau}{\tau_1}) \quad (5-12).$$

The inverse time scale $1/\tau_1$ gives the phonon frequency and $1/\tau_2$ determines the bandwidth of the Lorentzian line. We choose the values $\tau_1=0.0122$ ps and $\tau_2=0.032$ ps.

Another important parameter is the dispersion in highly nonlinear PCF. The simulation is based on photonic crystal fiber NL-770-2.0 (Crystal-fiber). Since the dispersion data provided by manufacturer are limited, I calculated the values based on bi-orthogonal vector method [144] to analyze the modes and calculate the dispersion relationship. Fig. 5.5(a) shows the fundamental mode in the PCF NL-770-2.0, and Fig. 5.5(b) displays the dispersion curves (red circles are the measured results provided by the manufacturer). The calculation shows a very good agreement with the experiment.



(a)



(b)

Figure 5.5 Typical transverse mode (a) and dispersion(b) of nonlinear PCF NL-770-2.0

The generalized nonlinear Schrödinger equations (NLSE) can be numerically solved through split-step Fourier method. The operators on pulse envelope can be categorized into linear operators, terms in the left side of the Eq. (5-10), and nonlinear operators, terms in the right side of Eq. (5-10). The linear operators account for the dispersions and loss, while the nonlinear operators represent power-related nonlinear process. The total propagation distance is divided into many small segments with the length of dz . Within each segment, linear propagation of pulse is first calculated over the distance from 0 to $dz/2$. And nonlinear operation is only taken into account at the middle plane of the segment, and then linear operation is again performed over the next half distance from $dz/2$ to dz . The linear part can be solved in frequency domain. But the nonlinear operation is realized in the temporal domain. More detailed description and discussion is available [143, 145]. Fig. 5.6 shows the simulation results of evolution of a transform limited pulses with Gaussian profile propagating in the nonlinear PCF (NL-770-2.0). We assume the average power of Ti: Sapphire femtosecond laser working at 800 nm wavelength is 100 mW with the typical repetition rate 80 MHz. The pulse width is 100 fs. The propagation distance increases 5 mm each time. We can find that within the initial short propagation distance, about 15 mm, the spectral broadening exhibits symmetric property while the pulse is compressed in time domain. After that, initial pulse breaks into several soliton-like pulses, the result of soliton fission effect [6], as shown in Fig. 5.6(a). At the same time, figure 5.6 (b) shows spectrum of pulse undertakes red-shifts in the frequency domain due to Raman scattering [6]. Newly generated long-wavelength components

get involved into FWM, dispersive wave generation and other complex nonlinear processes, resulting in spectrum broadening on the short-wavelength side. Finally an extremely broad band supercontinuum spectrum is generated. SC generation within the first 15 mm, where laser pulse is compressed in time domain but spectrum is broadened, is more of interest for THz as we discussed earlier in this section.

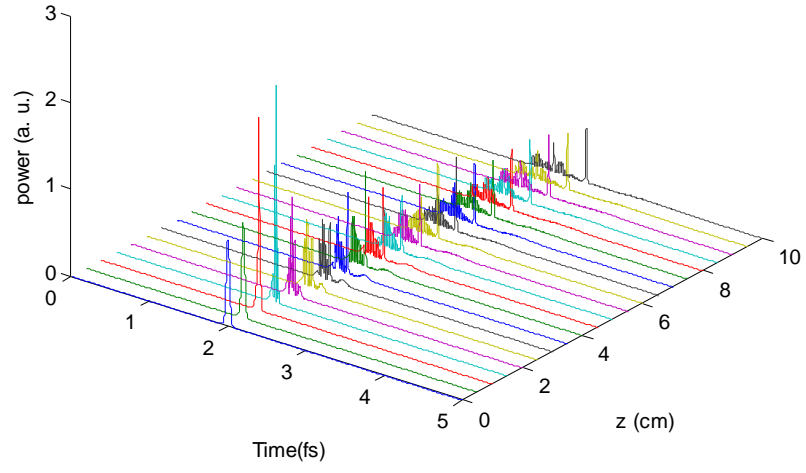
The wave equation for THz wave, Eq. (5-6), is also a nonlinear equation, which can be again numerically solved by the split-step Fourier method. Given that the envelope of THz is slowly varying during generation, the solution of Eq. (5-6) can be written as [146, 147]

$$\left[i\frac{\partial}{\partial z} - k(\Omega)\right]\overline{E_{THz}} = \frac{d_{eff}\Omega^2}{k(\Omega)c^2} \overline{|\tilde{\mathcal{E}}|^2} . \quad (5-13).$$

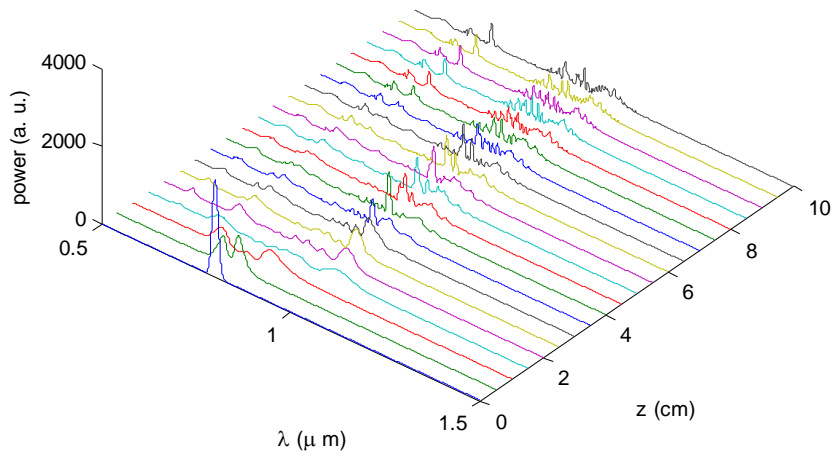
The left side of Eq. (5-13) is the linear operator and the right side is nonlinear term. The total propagation distance is also divided into many small segments with length of dz . Within each segment, over the distance from 0 to $dz/2$ linear propagations of pump pulse, using Eq. (5-8), and THz wave, left side of Eq. (5-13), are first calculated. At the middle plane of the segment, the two waves are connected through the nonlinear operation, right side of the Eq. (5-13), and then linear propagation of pump wave and THz wave are again calculated over the next half distance from $dz/2$ to dz .

Assuming the 100 fs laser pulses with Gaussian profile centered at 800 nm (100 mW/80 MHz), we first calculated SC generation with a 3 mm increment each time.

Fig. 5.7(a) shows spectrum expanding in frequency domain. The output SC was then used as input pump source and coupled into a 1 mm thick ZnTe crystal to calculate the THz spectrum. The results are shown in Fig. 5.7 (b). As we expected, the THz spectrum changes with different pump SC sources. As the SC spectrum broadening, phase matching condition is satisfied in a larger range, especially for the higher and lower ends. For example, the intensity of the frequency component at 1 THz pumped by SC generated from a 9 mm length PCF is almost 3 times as large as that pumped by a femtosecond laser directly. The simulation results show that the desired THz spectrum in longer or shorter wavelength can be obtained by adjusting the spectrum of SC via changing the length of PCF or tuning power of the femtosecond pumping laser.

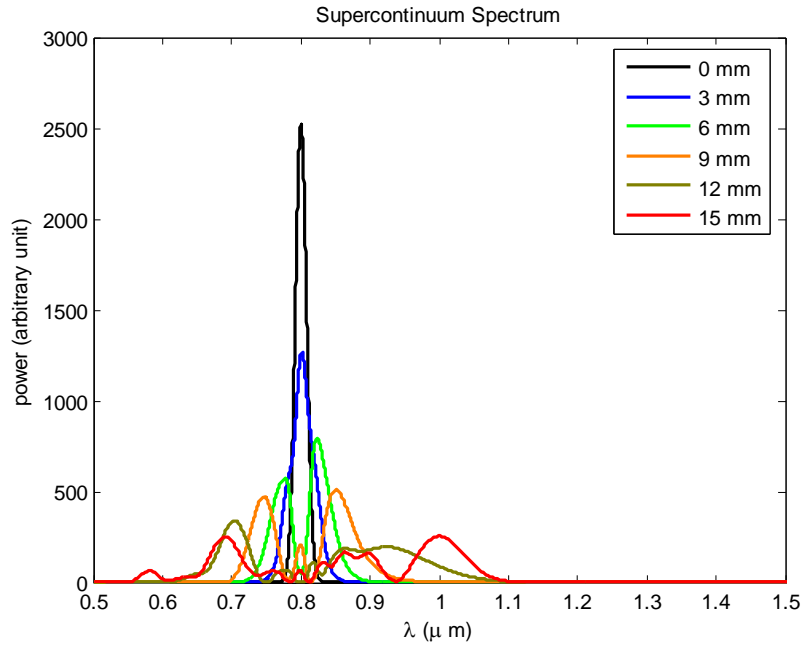


(a)

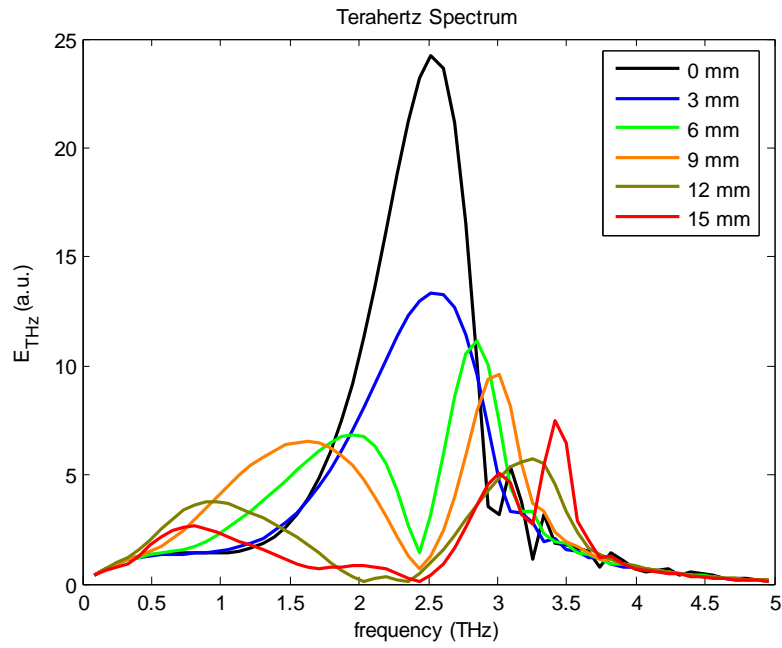


(b)

Figure 5.6 Temporal evolution of laser pulse (a) and spectrum broadening (b) in SC generation



(a)



(b)

Figure 5.7 Spectrum broadening in a nonlinear PCF and terahertz spectrum. (a) spectrum broadening of femtosecond laser pulses within nonlinear PCF of different propagation distances. (b) Terahertz spectrum generated by optical rectification of SC.

5.3 Summary

Terahertz technologies and their applications are promising in the near future. Optical rectification of ultrashort laser pulses in the second order nonlinear crystals is one of the most widely used methods of generating THz radiation. However, energy transfer efficiencies of it are low. In this chapter, a method using supercontinuum can improve the THz generation technique are proposed.

When a highly nonlinear PCF is pumped in the anomalous dispersion region, an optical soliton is formed in the fiber. Even if the propagation distance in the PCF is only a few millimeter long the supercontinuum spectrum can be broadened to a few hundred nanometers. At the same time, the pulse duration is kept within the range of sub-picosecond. In this case, the supercontinuum can be considered the superposition of a series of pulses with different central frequencies. Therefore, if supercontinuum was used as the pump source in optical rectification, phase matching condition can be satisfied in a broad region. The numerical simulation is realized by using split-step Fourier method. The calculation results show the spectrum changing with various pumping SC. This is an easy method to realize spectrum tuning and power enhancement for THz generation.

Chapter 6 Conclusions and Future Work

6.1 Conclusions

In this dissertation, three applications of ultrafast femtosecond lasers are presented. First, we study the single particle scattering spectroscopy using supercontinuum white light tweezers. Supercontinuum white light optical tweezers are demonstrated by using the ultra broad band supercontinuum (SC) generated in highly nonlinear photonic crystal fibers pumped by ultrafast laser pulses. The scattering spectroscopy of single particle trapped by supercontinuum white light tweezers was observed. Scattering spectra of different particles have been measured and presented. Trapping stiffness in the supercontinuum white light optical tweezers has been calibrated and results show that the trapping stiffness depends strongly on the supercontinuum spectrum.

The scattering spectra in tightly focused supercontinuum are also studied. When the scatterer is of spherical shape, modeling based on Mie's scattering theory and angular spectrum decomposition, are described. In the case of non-spherical-shaped scatterers, when the size of the scatterer is small or the refractive index of the scatterer is close to the surrounding medium, another model based on the Born approximation and Green's function is derived. The calculations are presented and discussed as well. This work has built a foundation for understanding optical scattering spectroscopy of single particle in the supercontinuum white light optical tweezers and points the directions to further applications to probe the single particle's physical and chemical

properties via the linear and nonlinear optical scattering spectra. These approaches can lead to many important applications particularly in nanoparticle characterization and sensing.

The second part of this dissertation is dedicated to the study of the femtosecond beam shaping. The performances of beam-shaping in the case of using femtosecond lasers with Gaussian beam profile into a flat-topped rectangular profile are studied and discussed for practical realization. A new criterion in the optimization process for beam shaping profile is described. Comparing with the result by optimizing the intensity profile mean square error (MSE), total intensity falling in the center target region has increased from 99.68% to 99.83%. At the meantime, better intensity profile is obtained. The temporal and spatial properties of femtosecond laser pulses during beam shaping are studied. The simulation results show that the intensity profile suffer distortion when working wavelength is off from the design wavelength, especially for using wrapped phase mask. However the distortions for the femtosecond laser pulses are much less, though the distortions are still observable. The FWHM pulse widths changes less than 5% in the center region. The reason is that the larger distortion components have much smaller intensity; as a result, the performance of center frequency dominates.

The last part of this dissertation is terahertz (THz) generation by optical rectification of femtosecond laser pulses. A method by using optical rectification of supercontinuum is proposed to improve the conversion efficiency over a broadband

range. Highly efficient broadband terahertz will accelerate the development of terahertz technologies and its applications such as biomedical imaging and remote security screening.

6.2 Future Work

Single particle spectroscopy technique by using supercontinuum white light optical tweezers has demonstrated the potential capabilities to probe the properties of scatterer being trapped, which will be useful in the research of biomedical science and material science. Future work will study the properties of biological cells and monitor the changes in real time.

Scattering spectra of noble metallic nanoparticles are more sensitive to its shape and surrounding media than those of dielectric particles due to the localized surface plasmon effects. So it is interesting to investigate the scattering spectroscopy of a single nano-sized metal particle trapped by supercontinuum white light optical tweezers, which can be potentially a new approach for real time monitoring the environment change in the microscopic world.

The simulation program developed for femtosecond beam shaping has been utilized for fabrication of EO-crystal-based phase modulators. A study will undertake to examine the performances of beam shaper in the real experiments. The phase modulators are assumed to be ideal, i.e., the diffraction effects and boundary effects are ignored when beam passes through phase modulation, which will result in discrepancy

between experiment results and simulations. Future work will expand the algorithm by taking into account of those factors.

Simulation of terahertz generation by optical rectification of supercontinuum pulses has demonstrated the possibility of improving the performance of THz generation by tuning the lengths of the highly nonlinear PCF. A preliminary concept-proof experiment should be performed in the near future.

Bibliography

1. J. C. Diels, and W. Rudolph, *Ultrashort laser pulse phenomena: fundamentals, techniques, and applications on a femtosecond time scale* (Academic Press, San Diego, 1996).
2. M. E. Fermann, A. Galvanauskas, and G. Sucha, *Ultrafast Lasers: Technology and Applications* (CRC Press, 2003).
3. P. Li, K. Shi, and Z. Liu, "Manipulation and spectroscopy of a single particle by use of white-light optical tweezers," *Opt. Lett.* **30**, 156-158 (2005).
4. R. R. Alfano, *The Supercontinuum Laser Source: Fundamentals With Updated References* (Springer, 2006).
5. J. K. Ranka, R. S. Windeler, and A. J. Stentz, "Visible continuum generation in air-silica microstructure optical fibers with anomalous dispersion at 800 nm," *Opt. Lett.* **25**, 25-27 (2000).
6. J. M. Dudley, G. Genty, and S. Coen, "Supercontinuum generation in photonic crystal fiber," *Rev. Mod. Phys.* **78**, 1135-1184 (2006).
7. J. C. Knight, T. A. Birks, P. S. J. Russell, and D. M. Atkin, "All-silica single-mode optical fiber with photonic crystal cladding," *Opt. Lett.* **21**, 1547-1549 (1996).
8. H. C. van de Hulst, *Light Scattering by Small Particles* (Courier Dover Publications, 1981).
9. F. M. Dickey, and S. C. Holswade, *Laser beam shaping: theory and techniques* (Marcel Dekker, New York, 2000).
10. R. W. Gerchberg, and W. O. Saxton, "A practical algorithm for the determination of phase from image and diffraction plane pictures," *Optik* **35**, 237-246 (1972).
11. J. S. Liu, and M. R. Taghizadeh, "Iterative algorithm for the design of diffractive phase elements for laser beam shaping," *Opt. Lett.* **27**, 1463-1465 (2002).
12. D. Mittleman, "Sensing with terahertz radiation," Springer series in optical sciences.
13. A. Rice, Y. Jin, X. F. Ma, X. C. Zhang, D. Bliss, J. Larkin, and M. Alexander, "Terahertz optical rectification from <110> zinc-blende crystals," *Appl. Phys. Lett.* **64**, 1324-1326 (1994).
14. Y. S. Lee, T. Meade, M. DeCamp, T. B. Norris, and A. Galvanauskas, "Temperature dependence of narrow-band terahertz generation from periodically poled lithium niobate," *Appl. Phys. Lett.* **77**, 1244-1266 (2000).
15. A. Ashkin, J. M. Dziedzic, J. E. Bjorkholm, and S. Chu, "Observation of a single-beam gradient force optical trap for dielectric particles," *Opt. Lett.* **11**, 288-290 (1986).
16. A. Ashkin, "History of optical trapping and manipulation of small-neutralparticle, atoms, and molecules," *IEEE J. Sel. Top. Quant.* **6**, 841-856 (2000).
17. D. G. Grier, "A revolution in optical manipulation," *Nature* **424**, 810-816 (2003).
18. K. C. Neuman, and S. M. Block, "Optical trapping," *Rev. Sci. Instrum.* **75**, 2787 (2004).
19. K. Dholakia, P. Reece, and M. Gu, "Optical micromanipulation," *Chem. Soc. Rev.* **37**, 42-55 (2008).
20. S. Chu, J. E. Bjorkholm, A. Ashkin, and A. Cable, "Experimental Observation of Optically Trapped Atoms," *Phys. Rev. Lett.* **57**, 314-317 (1986).
21. J. C. Crocker, and D. G. Grier, "Microscopic measurement of the pair interaction potential of charge-stabilized colloid," *Phys. Rev. Lett.* **73**, 352-355 (1994).

22. J. C. Crocker, and D. G. Grier, "When Like Charges Attract: The Effects of Geometrical Confinement on Long-Range Colloidal Interactions," *Phys. Rev. Lett.* **77**, 1897-1900 (1996).
23. Y. N. Ohshima, H. Sakagami, K. Okumoto, A. Tokoyoda, T. Igarashi, K. B. Shintaku, S. Toride, H. Sekino, K. Kabuto, and I. Nishio, "Direct Measurement of Infinitesimal Depletion Force in a Colloid-Polymer Mixture by Laser Radiation Pressure," *Phys. Rev. Lett.* **78**, 3963-3966 (1997).
24. J. C. Crocker, J. A. Matteo, A. D. Dinsmore, and A. G. Yodh, "Entropic Attraction and Repulsion in Binary Colloids Probed with a Line Optical Tweezer," *Phys. Rev. Lett.* **82**, 4352-4355 (1999).
25. R. Verma, J. C. Crocker, T. C. Lubensky, and A. G. Yodh, "Attractions between hard colloidal spheres in semi-flexible polymer solutions," *Macromolecules* **33**, 177-186 (2000).
26. A. G. Yodh, "Entropically driven self-assembly and interaction in suspension," *Phil. Trans. Roy. Soc. A* **359**, 921-937 (2001).
27. G. M. Wang, E. M. Sevick, E. Mittag, D. J. Searles, and D. J. Evans, "Experimental Demonstration of Violations of the Second Law of Thermodynamics for Small Systems and Short Time Scales," *Phys. Rev. Lett.* **89**, 50601 (2002).
28. A. Ashkin, J. M. Dziedzic, and T. Yamane, "Optical trapping and manipulation of single cells using infrared laser beams," *Nature* **330**, 769-771 (1987).
29. A. Ashkin, and J. M. Dziedzic, "Optical trapping and manipulation of viruses and bacteria," *Science* **235**, 1517-1520 (1987).
30. K. Svoboda, P. P. Mitra, and S. M. Block, "Fluctuation analysis of Motor Protein Movement and Single Enzyme Kinetics," *Proc. Nat. Acad. Sci. USA* **91**, 11782-11786 (1994).
31. C. Bustamante, S. B. Smith, J. Liphardt, and D. Smith, "Single-molecule studies of DNA mechanics," *Curr. Opin. Struct. Biol.* **10**, 279-285 (2000).
32. M. W. Berns, "Laser scissors and tweezers," *Sc. Am.* **278**, 52-57 (1998).
33. K. Svoboda, and S. M. Block, "Biological Applications of Optical Forces," *Annu. Rev. Biophys. Biomol. Struct.* **23**, 247-285 (1994).
34. A. D. Mehta, J. T. Finer, and J. A. Spudich, "Use of optical traps in single-molecule study of nonprocessive biological motors," *Methods Enzymol* **298**, 436-459 (1998).
35. A. D. Mehta, M. Rief, J. A. Spudich, D. A. Smith, and R. M. Simmons, "Single-Molecule Biomechanics with Optical Methods," *Science* **283**, 1689 (1999).
36. S. C. Kuo, "Using Optics to Measure Biological Forces and Mechanics," *Traffic* **2**, 757-763 (2001).
37. A. Ishijima, and T. Yanagida, "Single molecule nanobioscience," *Trend. Biochem. Sci.* **26**, 438-444 (2001).
38. Y. Ishii, A. Ishijima, and T. Yanagida, "Single molecule nanomanipulation of biomolecules," *Trend. Biotech.* **19**, 211-216 (2001).
39. S. Khan, and M. P. Sheetz, "Force Effects on Biochemical Kinetics," *Annu. Rev. Biochem.* **66**, 785-805 (1997).
40. C. Bustamante, J. C. Macosko, and G. J. L. Wuite, "Grabbing the cat by the tail: manipulating molecules one by one," *Nat. Rev. Mol. Cell Biol.* **1**, 130-136 (2000).
41. K. Svoboda, and S. M. Block, "Optical trapping of metallic Rayleigh particles," *Opt. Lett.* **19**, 930-932 (1994).
42. P. C. Ke, and M. Gu, "Characterization of trapping force on metallic Mie particles," *Appl. Opt.* **38**, 160-167 (1999).

43. L. P. Ghislain, N. A. Switz, and W. W. Webb, "Measurement of small forces using an optical trap," *Rev. Sci. Instrum.* **65**, 2762 (1994).
44. A. Rohrbach, and E. H. K. Stelzer, "Trapping forces, force constants, and potential depths for dielectric spheres in the presence of spherical aberrations," *Appl. Opt.* **41**, 2494-2507 (2002).
45. H. Yin, M. D. Wang, K. Svoboda, R. Landick, S. M. Block, and J. Gelles, "Transcription Against an Applied Force," *Science* **270**, 1653 (1995).
46. D. Raucher, T. Stauffer, W. Chen, K. Shen, S. Guo, J. D. York, M. P. Sheetz, and T. Meyer, "Phosphatidylinositol 4, 5-Bisphosphate Functions as a Second Messenger that Regulates Cytoskeleton-Plasma Membrane Adhesion," *Cell* **100**, 221-228 (2000).
47. E. Eriksson, J. Scrimgeour, A. Graneli, K. Ramser, R. Wellander, J. Enger, D. Hanstorp, and M. Goksor, "Optical manipulation and microfluidics for studies of single cell dynamics," *J. Opt. A* **9**, S113-S121 (2007).
48. T. Shimada, W. Watanabe, S. Matsunaga, T. Higashi, H. Ishii, K. Fukui, K. Isobe, and K. Itoh, "Intracellular disruption of mitochondria in a living HeLa cell with a 76-MHz femtosecond laser oscillator," *OpticsExpress* **13**, 9869-9880 (2005).
49. J. E. Curtis, B. A. Koss, and D. G. Grier, "Dynamic holographic optical tweezers," *Opt. Comm.* **207**, 169-175 (2002).
50. M. Reicherter, T. Haist, E. U. Wagemann, and H. J. Tiziani, "Optical particle trapping with computer-generated holograms written on a liquid-crystal display," *Opt. Lett.* **24**, 608-610 (1999).
51. P. C. Mogensen, and J. Glückstad, "Dynamic array generation and pattern formation for optical tweezers," *Opt. Comm.* **175**, 75-81 (2000).
52. M. E. J. Friese, T. A. Nieminen, N. R. Heckenberg, and H. Rubinsztein-Dunlop, "Optical alignment and spinning of laser-trapped microscopic particles," *Nature* **394**, 348-350 (1998).
53. N. B. Simpson, K. Dholakia, L. Allen, and M. J. Padgett, "Mechanical equivalence of spin and orbital angular momentum of light: an optical spanner," *Opt. Lett.* **22**, 52-54 (1997).
54. H. He, M. E. J. Friese, N. R. Heckenberg, and H. Rubinsztein-Dunlop, "Direct Observation of Transfer of Angular Momentum to Absorptive Particles from a Laser Beam with a Phase Singularity," *Phys. Rev. Lett.* **75**, 826-829 (1995).
55. V. Garces-Chavez, D. McGloin, H. Melville, W. Sibbett, and K. Dholakia, "Simultaneous micromanipulation in multiple planes using a self-reconstructing light beam," *Nature* **419**, 145-147 (2002).
56. K. Ajito, and K. Torimitsu, "Near-infrared Raman spectroscopy of single particles," *Trend. Anal. Chem.* **20**, 255-262 (2001).
57. C. Xie, and Y. Li, "Raman spectra and optical trapping of highly refractive and nontransparent particles," *Appl. Phys. Lett.* **81**, 951 (2002).
58. J. Prikulis, F. Svedberg, M. Käll, J. Enger, K. Ramser, M. Goksör, and D. Hanstorp, "Optical spectroscopy of single trapped metal nanoparticles in solution," *Nano Lett.* **4**, 115-118 (2004).
59. R. R. Alfano, and S. L. Shapiro, "Emission In Region 4000 To 7000 A Via 4-Photon Coupling In Glass," *Phys. Rev. Lett.* **24**, 584-587 (1970).
60. C. Lin, and R. H. Stolen, "New nanosecond continuum for excited-state spectroscopy," *Appl. Phys. Lett.* **28**, 216 (1976).

61. T. A. Birks, W. J. Wadsworth, and P. S. J. Russell, "Supercontinuum generation in tapered fibers," *Opt. Lett.* **25**, 1415-1417 (2000).
62. "<http://www.crystal-fibre.com>."
63. R. H. Stolen, C. Lee, and R. K. Jain, "Development of the stimulated Raman spectrum in single-mode silica fibers," *JOSA B* **1**, 652-657 (1984).
64. P. L. Baldeck, P. P. Ho, and R. R. Alfano, "Effects of self, induced and cross phase modulations on the generation of picosecond and femtosecond white light supercontinua," *Revue de Physique Appliquee* **22**, 1677-1694 (1987).
65. I. Ilev, H. Kumagai, K. Toyoda, and I. Koprnikov, "Highly efficient wideband continuum generation in a single-mode optical fiber by powerful broadband laser pumping," *Appl. Opt.* **35**, 2548-2553 (1996).
66. P. K. A. Wai, C. R. Menyuk, Y. C. Lee, and H. H. Chen, "Nonlinear pulse propagation in the neighborhood of the zero-dispersion wavelength of monomode optical fibers," *Opt. Lett.* **11**, 464-466 (1986).
67. A. V. Husakou, and J. Herrmann, "Supercontinuum Generation of Higher-Order Solitons by Fission in Photonic Crystal Fibers," *Phys. Rev. Lett.* **87**, 203901 (2001).
68. J. P. Gordon, "Theory of the soliton self-frequency shift," *Opt. Lett.* **11**, 662-664 (1986).
69. F. M. Mitschke, and L. F. Mollenauer, "Discovery of the soliton self-frequency shift," *Opt. Lett.* **11**, 659-661 (1986).
70. N. Akhmediev, and M. Karlsson, "Cherenkov radiation emitted by solitons in optical fibers," *Phys. Rev. A* **51**, 2602-2607 (1995).
71. T. Udem, R. Holzwarth, and T. W. Haensch, "Optical frequency metrology," *Nature* **416**, 233-237 (2002).
72. I. Hartl, X. D. Li, C. Chudoba, R. K. Ghanta, T. H. Ko, J. G. Fujimoto, J. K. Ranka, and R. S. Windeler, "Ultrahigh-resolution optical coherence tomography using continuum generation in an air-silica microstructure optical fiber," *Opt. Lett.* **26**, 608-610 (2001).
73. Z. Yusoff, P. Petropoulos, K. Furusawa, T. M. Monro, and D. J. Richardson, "A 36 channel x 10 GHz spectrally sliced pulse source based on supercontinuum generation in normally dispersive highly nonlinear holey fibre," *IEEE Photonic Tech. Lett.* **15**, 1689-1691 (2003).
74. K. Shi, S. H. Nam, P. Li, S. Yin, and Z. Liu, "Wavelength division multiplexed confocal microscopy using supercontinuum," *Opt. Comm.* **263**, 156-162 (2006).
75. K. Shi, P. Li, S. Yin, and Z. Liu, "Chromatic confocal microscopy using supercontinuum light," *OpticsExpress* **12**, 2096-2101 (2004).
76. H. Kano, and H. Hamaguchi, "Femtosecond coherent anti-Stokes Raman scattering spectroscopy using supercontinuum generated from a photonic crystal fiber," *Appl. Phys. Lett.* **85**, 4298 (2004).
77. K. Shi, P. Li, and Z. Liu, "Broadband coherent anti-Stokes Raman scattering spectroscopy in supercontinuum optical trap," *Appl. Phys. Lett.* **90**, 141116 (2007).
78. M. P. MacDonald, L. Paterson, K. Volke-Sepulveda, J. Arlt, W. Sibbett, and K. Dholakia, "Creation and Manipulation of Three-Dimensional Optically Trapped Structures," (2002), pp. 1101-1103.
79. J. Arlt, V. Garcés-Chavez, W. Sibbett, and K. Dholakia, "Optical micromanipulation using a Bessel light beam," *Opt. Comm.* **197**, 239-245 (2001).

80. H. Felgner, O. Muller, and M. Schliwa, "Calibration of light forces in optical tweezers," *Appl. Opt.* **34**, 977-982 (1995).
81. N. Malagnino, G. Pesce, A. Sasso, and E. Arimondo, "Measurements of trapping efficiency and stiffness in optical tweezers," *Opt. Comm.* **214**, 15-24 (2002).
82. K. Berg-Sørensen, and H. Flyvbjerg, "Power spectrum analysis for optical tweezers," *Rev. Sci. Instrum.* **75**, 594 (2004).
83. I. M. Tolic-Nørrelykke, K. Berg-Sørensen, and H. Flyvbjerg, "MatLab program for precision calibration of optical tweezers," *Comput. Phys. Comm.* **159**, 225-240 (2004).
84. M. Capitanio, G. Romano, R. Ballerini, M. Giuntini, F. S. Pavone, D. Dunlap, and L. Finzi, "Calibration of optical tweezers with differential interference contrast signals," *Rev. Sci. Instrum.* **73**, 1687 (2002).
85. B. A. Nemet, and M. Cronin-Golomb, "Microscopic flow measurements with optically trapped microprobes," *Opt. Lett.* **27**, 1357-1359 (2002).
86. B. A. Nemet, and M. Cronin-Golomb, "Measuring microscopic viscosity with optical tweezers as a confocal probe," *Appl. Opt.* **42**, 1820-1832 (2003).
87. M. Doi, and H. See, *Introduction to polymer physics* (Oxford University Press, New York, 1996).
88. E. W. Casperson, C. Yeh, and W. F. Yeung, "Single particle scattering with focused laser beams," *Appl. Opt.* **16**, 1104-1107 (1977).
89. H. Chew, M. Kerker, and D. D. Cooke, "Light scattering in converging beams," *Opt. Lett.* **1**, 138-140 (1977).
90. J. P. Chevaillier, J. Fabre, and P. Hamelin, "Forward scattered light intensities by a sphere located anywhere in," *Appl. Opt.* **25**, (1986).
91. G. Gouesbet, G. Grehan, and B. Maheu, "Scattering of a Gaussian beam by a Mie scatter center using a Bromwich formalism," *J. Opt.(Paris)* **16**, 83-93 (1985).
92. J. T. Hodges, G. Gréhan, G. Gouesbet, and C. Presser, "Forward scattering of a Gaussian beam by a nonabsorbing sphere," *Appl. Opt.* **34**, 2120-2132 (1995).
93. S. O. Park, and S. S. Lee, "Forward far-field pattern of a laser beam scattered by a water-suspended homogeneous sphere trapped by a focused laser beam," *JOSA A* **4**, 417-422 (1987).
94. J. A. Lock, "Improved Gaussian beam-scattering algorithm," *Appl. Opt.* **34**, 559-570 (1995).
95. J. A. Lock, "Calculation of the Radiation Trapping Force for Laser Tweezers by Use of Generalized Lorenz-Mie Theory. I. Localized Model Description of an On-Axis Tightly Focused Laser Beam with Spherical Aberration," *Appl. Opt.* **43**, 2532-2544 (2004).
96. J. A. Lock, "Calculation of the Radiation Trapping Force for Laser Tweezers by Use of Generalized Lorenz-Mie Theory. II. On-Axis Trapping Force," *Appl. Opt.* **43**, 2545-2554 (2004).
97. P. Li, K. Shi, and Z. Liu, "Optical scattering spectroscopy by using tightly focused supercontinuum," *OpticsExpress* **13**, 9039-9044 (2005).
98. A. Rohrbach, and E. H. K. Stelzer, "Three-dimensional position detection of optically trapped dielectric particles," *J. Appl. Phys.* **91**, 5474 (2002).
99. L. Novotny, R. D. Grober, and K. Karrai, "Reflected image of a strongly focused spot," *Opt. Lett.* **26**, 789-791 (2001).

100. P. Török, P. D. Higdon, R. Juškaitis, and T. Wilson, "Optimising the image contrast of conventional and confocal optical microscopes imaging finite sized spherical gold scatterers," *Opt. Comm.* **155**, 335-341 (1998).
101. J. D. Jackson, *Classical Electrodynamics* (Wiley, New York, 1999).
102. L. Mandel, and E. Wolf, *Optical Coherence and Quantum Optics* (Cambridge University Press, 1995).
103. E. Wolf, "Electromagnetic Diffraction in Optical Systems. I. An Integral Representation of the Image Field," *Proc. Roy. Soc. Lond. A* **253**, 349-357 (1959).
104. E. D. Palik, *Handbook of Optical Constants of Solids I* (Academic Press, San Diego, 1998).
105. T. Klar, M. Perner, S. Grosse, G. von Plessen, W. Spirkl, and J. Feldmann, "Surface-Plasmon Resonances in Single Metallic Nanoparticles," *Phys. Rev. Lett.* **80**, 4249-4252 (1998).
106. G. W. Burr, "Volume holographic storage using the 90-degree geometry," (Californina Institute of Technology, 1996).
107. J. X. Cheng, and X. S. Xie, "Greens function formulation for third-harmonic generation microscopy," *JOSA B* **19**, 1604-1610 (2002).
108. L. Novotny, and B. Hecht, *Principles of Nano-Optics* (Cambridge University Press, 2006).
109. B. Richards, and E. Wolf, "Electromagnetic Diffraction in Optical Systems. II. Structure of the Image Field in an Aplanatic System," *Proc. Roy. Soc. Lond. A* **253**, 358-379 (1959).
110. B. R. Frieden, "Lossless conversion of a plane laser wave to a plane wave of uniform irradiance," *Appl. Opt.* **4**, 1400-1403 (1965).
111. T. R. Groves, and R. A. Kendall, "Distributed, multiple variable shaped electron beam column for high throughput maskless lithography," *J. Vac. Sci. Tech. B* **16**, 3168-3173 (1998).
112. S. Johansson, V. Pasiskevicius, F. Laurell, R. Hansson, and K. Ekvall, "Laser diode beam shaping with GRIN lenses using the twisted beam approach and its application in pumping of a solid-state laser," *Opt. Comm.* **274**, 403-406 (2007).
113. A. Masters, and T. Geuking, "Beam shaping optics expand excimer-laser applications," *Laser Focus World* **41**, 99-+ (2005).
114. G. Sinclair, J. Leach, P. Jordan, G. Gibson, E. Yao, Z. J. Laczik, M. J. Padgett, and J. Courtial, "Interactive application in holographic optical tweezers of a multi-plane Gerchberg-Saxton algorithm for three-dimensional light shaping," *OpticsExpress* **12**, 1665-1670 (2004).
115. S. Heinemann, "Computer-Generated Beam Shaping and Focusing Optical-Elements for Laser Material Processing," *Opt. Comm.* **119**, 613-622 (1995).
116. N. Bärsch, K. Körber, A. Ostendorf, and K. H. Tönshoff, "Ablation and cutting of planar silicon devices using femtosecond laser pulses," *Appl. Phys. A* **77**, 237-242 (2003).
117. X. Liu, D. Du, and G. Mourou, "Laser ablation and micromachining with ultrashort laser pulses," *Quantum Electronics, IEEE Journal of* **33**, 1706-1716 (1997).
118. B. N. Chichkov, C. Momma, S. Nolte, F. von Alvensleben, and A. Tünnermann, "Femtosecond, picosecond and nanosecond laser ablation of solids," *Appl. Phys. A* **63**, 109-115 (1996).
119. N. Sanner, N. Huot, E. Audouard, C. Larat, J. P. Huignard, and B. Loiseaux, "Programmable focal spot shaping of amplified femtosecond laser pulses," *Opt. Lett.* **30**, 1479-1481 (2005).

120. D. L. Woolard, W. R. Loerop, and M. Shur, *Terahertz Sensing Technology: Volume 1: Electronic Devices and Advanced Systems Technology* (World Scientific Pub Co Inc, 2003).
121. L. Ives, C. Kory, M. Read, J. Neilson, M. Caplan, N. Chubun, R. Wilcox, T. Robinson, C. C. Res, and S. Inc, "Development of Terahertz backward wave oscillators," Vacuum Electronics Conference, 2004. IVEC 2004. Fifth IEEE International, 67-68 (2004).
122. Y. Matsui, M. D. Pelusi, S. Arahira, and Y. Ogawa, "Beat frequency generation up to 3.4THz from simultaneous two-mode lasing operation of sampled-grating DBR laser," Electron. Lett. **35**, 472-474 (1999).
123. T. Tanabe, K. Suto, J. Nishizawa, K. Saito, and T. Kimura, "Tunable terahertz wave generation in the 3-to 7-THz region from GaP," Appl. Phys. Lett. **83**, 237-239 (2003).
124. M. C. Wanke, O. Lehmann, K. Muller, Q. Z. Wen, and M. Stuke, "Laser rapid prototyping of photonic band-gap microstructures," Science **275**, 1284-1286 (1997).
125. B. S. Williams, S. Kumar, Q. Hu, and J. L. Reno, "Resonant-phonon terahertz quantum-cascade laser operating at 2.1 THz (λ similar or equal to 141 μ m)," Electron. Lett. **40**, 431-433 (2004).
126. P. K. Benicewicz, J. P. Roberts, and A. J. Taylor, "Scaling of Terahertz Radiation from Large-Aperture Biased Photoconductors," JOSA B **11**, 2533-2546 (1994).
127. P. R. Smith, D. H. Auston, and M. C. Nuss, "Subpicosecond photoconducting dipole antennas," Quantum Electronics, IEEE Journal of **24**, 255-260 (1988).
128. J. Hebling, A. G. Stepanov, G. Almasi, B. Bartal, and J. Kuhl, "Tunable THz pulse generation by optical rectification of ultrashort laser pulses with tilted pulse fronts," Appl. Phys. B **78**, 593-599 (2004).
129. R. W. Boyd, *Nonlinear Optics* (Academic Press, 2003).
130. A. Nahata, A. S. Weling, and T. F. Heinz, "A wideband coherent terahertz spectroscopy system using optical rectification and electro-optic sampling," Appl. Phys. Lett. **69**, 2321-2323 (1996).
131. D. T. F. Marple, "Refractive Index of Znse, Znte, + Cdte," J. Appl. Phys. **35**, 539 (1964).
132. T. Hattori, Y. Homma, A. Mitsuishi, and M. Tacke, "Indices of refraction of ZnS, ZnSe, ZnTe, CdS, and CdTe in the far infrared," Opt. Comm. **7**, 229-232 (1973).
133. Y. Sasaki, A. Yuri, K. Kawase, and H. Ito, "Terahertz-wave surface-emitted difference frequency generation in slant-stripe-type periodically poled LiNbO3 crystal," Appl. Phys. Lett. **81**, 3323-3325 (2002).
134. Y. Sasaki, Y. Avetisyan, H. Yokoyama, and H. Ito, "Surface-emitted terahertz-wave difference-frequency generation in two-dimensional periodically poled lithium niobate," Opt. Lett. **30**, 2927-2929 (2005).
135. K. Kawase, T. Hatanaka, H. Takahashi, K. Nakamura, T. Taniuchi, and H. Ito, "Tunable terahertz-wave generation from DAST crystal by dual signal-wave parametric oscillation of periodically poled lithium niobate," Opt. Lett. **25**, 1714-1716 (2000).
136. D. H. Auston, K. P. Cheung, J. A. Valdmanis, and D. A. Kleinman, "Cherenkov Radiation from Femtosecond Optical Pulses in Electro-Optic Media," Phys. Rev. Lett. **53**, 1555-1558 (1984).
137. A. G. Stepanov, J. Kuhl, I. Z. Kozma, E. Riedle, G. Almasi, and J. Hebling, "Scaling up the energy of THz pulses created by optical rectification," OpticsExpress **13**, 5762-5768 (2005).

138. A. G. Stepanov, J. Hebling, and J. Kuhl, "Efficient generation of subpicosecond terahertz radiation by phase-matched optical rectification using ultrashort laser pulses with tilted pulse fronts," *Appl. Phys. Lett.* **83**, 3000-3002 (2003).
139. K. L. Yeh, M. C. Hoffmann, J. Hebling, and K. A. Nelson, "Generation of 10 mJ ultrashort terahertz pulses by optical rectification," *Appl. Phys. Lett.* **90**, (2007).
140. J. Ahn, A. Efimov, R. Averitt, and A. Taylor, "Terahertz waveform synthesis via optical rectification of shaped ultrafast laser pulses," *OpticsExpress* **11**, 2486-2496 (2003).
141. Y. Liu, S. G. Park, and A. M. Weiner, "Terahertz Waveform Synthesis via Optical Pulse Shaping," *IEEE J. Sel. Top. Quant.* **2**, 709 (1996).
142. G. P. Agrawal, *Nonlinear fiber optics* (Springer, 2001).
143. K. J. Blow, and D. Wood, "Theoretical description of transient stimulated Raman scattering in optical fibers," *Quantum Electronics, IEEE Journal of* **25**, 2665-2673 (1989).
144. E. Silvestre, M. V. Andres, and P. Andres, "Biorthonormal-basis method for the vector description of optical-fiber modes," *J. Lightwave Tech.* **16**, 923-928 (1998).
145. I. Cristiani, R. Tediosi, L. Tartara, and V. Degiorgio, "Dispersive wave generation by solitons in microstructured optical fibers," *OpticsExpress* **12**, 124-135 (2004).
146. Y. J. Ding, "Efficient generation of high-power quasi-single-cycle terahertz pulses from a single infrared beam in a second-order nonlinear medium," *Optics Letters* **29**, 2650-2652 (2004).
147. Y. J. Ding, "Quasi-single-cycle terahertz pulses based on broadband-phase-matched difference-frequency generation in second-order nonlinear medium: high output powers and conversion efficiencies," *IEEE J. Sel. Top. Quant.* **10**, 1171-1179 (2004).

Vita

Peng Li

Education

- Ph.D. in Electrical Engineering Expected Aug 2008
The Pennsylvania State University, University Park, PA, 16802 USA
- M.S. in Optics Jun 2001
Nankai University, Tianjin, P.R.China
- B.S. in Applied Optics Jun 1998
Nankai University, Tianjin, P.R.China

Publications

- K. Shi, **P. Li**, and Z. Liu, "Supercontinuum Cars tweezers", Journal of Nonlinear Optical Physics & Materials, **16**, 457-470 (2007)
- K. Shi, **P. Li**, and Z. Liu, "Broadband coherent anti-Stokes Raman scattering spectroscopy in supercontinuum optical trap", *Applied Physics Letters* **90**, 141116 (2007)
- K. Shi, S. H. Nam, **P. Li**, S. Yin, and Z. Liu, "Wavelength division multiplexed confocal microscopy using supercontinuum, " *Optics Communications*, **263**, 156-162 (2006)
- **P. Li**, K. Shi, and Z. Liu, "Optical scattering spectroscopy by using tightly focused supercontinuum," *Optics Express* 13, 9039-9044 (2005).
- **P. Li**, K. Shi, and Z. Liu, "Manipulation and spectroscopy of a single particle by use of white-light optical tweezers," *Optics Letters* 30, 156-158 (2005).
- K. Shi, **P. Li**, S. Yin, and Z. Liu, "Chromatic confocal microscopy using supercontinuum light," *Optics Express* 12, 2096-2101(2004)